RNI - No. MAHENG / 2017 / 74063
VOLUME 3 (Issue 1) July - Dec 2019

ISSN No. 2561-5911
BI-ANNUAL SUBSCRIPTION : Rs. 2000/-

G P GLOBALIZE RESEARCH JOURNAL OF CHEMISTRY

Abstracted in Chemical Abstracts (CAS), USA
International Scientific Indexing (ISI)
Impact Factor 0.883 (2018)
International Society for Research Activity Journal Impact Factor 0.615
International Institute of Organized Research (I2OR) Impact Factor 1.405 (2019)

GAURANG PUBLISHING

GAURANG PUBLISHING GLOBALIZE
PRIVATE LIMITED

RNI No. MAHENG/2017/74063 ISSN (Print) No. 2581–5911

Volume 3 Issue 1 ❖ July – December 2019

G P GLOBALIZE RESEARCH JOURNAL OF CHEMISTRY

Abstracted in Chemical Abstracts (CAS), USA
International Scientific Indexing (ISI) Impact Factor 0.883 (2018)
International Institute of Organized Research (I2OR) Impact Factor 1.405 (2019)
ISRA Journal Impact Factor 0.615

Supported by **ASSOCIATION OF CHEMISTRY TEACHERS**, the National Registered Organisation of Chemistry Educators of India
Registration No. Maharashtra Government, Mumbai, 922, 2010 G.B.B.S.D. dated 08.04.2010.
Website: www.associationofchemistryteachers.org

GAURANG PUBLISHING GLOBALIZE PRIVATE LIMITED, MUMBAI

CIN No. U22130MH2016PTC287238

UAN - MH19D0008178

Published by:
Gaurang Publishing Globalize Private Limited, Mumbai
1, Plot 72, Pandit M.M.M. Marg, Tardeo, Mumbai 400 034.
Email: gpglobalize@gmail.com
www.gpglobalize.com
Tel: +91 9969392245
CIN No. U22130MH2016PTC287238

ISSN (Print) No: 2581-5911

Printed at: Nil Creation, Girgaum, Mumbai - 400 004, India.

GP GLOBALIZE RESEARCH JOURNAL OF CHEMISTRY

An International Peer Reviewed Journal of Chemistry

RNI No: MAHENG/2017/74063 **ISSN (Print) No: 2581-5911**
ISI Impact Factor: 0.883 (2018)

Printed and Published by Gaurang Rajan Pendurkar on behalf of Gaurang Publishing Globalize Private Limited and printed at NIL CREATION, Shop No. 7, 35/55, Bandu Gokhale Path, Mugbhat Cross Lane, Jivanji Maharaj Chawl (Shree Swami Samarth Nagar), Girgaon, Mumbai 400004 and published at Gaurang Publishing Globalize Private Limited 1, Plot 72, P M M M Marg, Tardeo, Mumbai-400034.
Editor-in-Chief Dr. D.V. Prabhu.

G P GLOBALIZE RESEARCH JOURNAL OF CHEMISTRY

RNI No: MAHENG/2017/74063 **ISSN No (Print): 2581-5911**
ISI Impact Factor: 0.883 (2018)

GUIDELINES TO AUTHORS

GP Globalize Research Journal of Chemistry is an international peer reviewed journal which publishes full length research papers, short communications, review articles and book reviews covering all areas of Chemistry including Environmental Chemistry. G P Globalize Research Journal of Chemistry is a biannual journal published in English in print and online versions.

(1) Manuscript preparation

a) Page Layout: A4 (21 cm x 29.7 cm) leaving 2.5 cm margin on all sides of the text. All the text should be in Times New Roman font, double spaced and pages should be numbered consecutively.

b) Use MS word (2003-2007) for text and TIFF, JPEG or Paint for figures.

c) The first page should contain title in bold, 14 point size, name/s of author/s in bold, 12 point size, affiliation/s-address, email id and contact number in 11 point size, abstract-up to 200 words in 11 point size, keywords-between 5 to 10 keywords in 11 point size.

d) Main Text- The paper should be divided into the following sections:

Introduction, Materials and Methods, Results and Discussion, Conclusions, Acknowledgement and References.

Tables and Figures of good resolution (600 dpi) should be numbered consecutively and given in the order of their appearance in the text and should not be given on separate pages.

e) References- References should be cited in the text as superscript numbers in order of appearance.

References at the end of the paper should be listed in serial order to match their order of appearance in the text. Names of journals should be in italics and volume number should be in bold.

Reference to papers e.g. Ganesh R.S., Pravin S. and Rao T.P., 2005, *Talanta,* **66,** 513.

Reference to books e.g. Lee J.D., 1984, A New Course in Inorganic Chemistry, 3rd ed., ELBS and Van Nostrand Reinhold (UK) Co. Ltd., p.268-269.

f) Abbreviations should be explained at first appearance in the text.

g) Nomenclature should be as per **IUPAC** guidelines.

h) SI units should be used throughout.

(2) Manuscript Submission

Manuscripts should be submitted online at dvprabhu48@gmail.com. The paper will be accepted for publication after review. All correspondence should be made to the Editor-in-Chief at dvprabhu48@gmail.com.

(3) Proofs

Galley proofs will be sent online to the corresponding author on request and should be returned to the Editorial office within seven working days.

(4) Plagiarism

GP Globalize Research Journal of Chemistry is committed to avoid plagiarism and ensure that only original research work is published.

The Editorial Board and panel of reviewers will check and prevent plagiarism in the manuscripts submitted for publication.

(5) Copyright

Publication of a paper in GP Globalize Research Journal of Chemistry automatically transfers copyright to the publisher. Authors can share free eprints of their published papers with fellow researchers.

(6) Circulation and Subscription Rates

The Journal is published twice a year - January and July

Subscription rates are as follows:

Library/Instituional charges (In India)	Rs. 2000/-
Individual charges (In India)	Rs. 2000/-
Library/Instituonal charges (Outside India)	US $ 100
Individual charges (Outside India)	US $ 100

Subscription charges:
Review of Research papers is done free of charge. Subscription to the Journal is expected.

Mode of Payment:

Demand draft/Multicity cheque payable at Mumbai in favour of
"Gaurang Publishing Globalize Pvt. Ltd. Mumbai"

For Online Payment:

Name of the Bank	**:**	**Axis Bank**
Branch Name	**:**	**Tardeo, Mumbai (MH)**
Account No.	**:**	**916020066451552**
IFSC Code	**:**	**UTIB0001345**

For further details please contact:

Dr. D.V. Prabhu, Editor-in-Chief,
Email: dvprabhu48@gmail.com
Mobile: 09870 226 899

Mr. Rajan Pendurkar, Publishing Co-ordinator,
Email: gpglobalize@gmail.com
Mobile: 09969 392 245

A Request to Authors

We thank you for sending your research paper to G P Globalize Research Journal of Chemistry (RNI No. MAHENG/2017/74063 ISSN No. (Print): 2581-5911).

Review of research papers is done free of charge.

You are requested to send a DD/Multicity Cheque for Rs. 2000/- in favour of ***"Gaurang Publishing Globalize Pvt. Ltd., Mumbai"*** *payable at Mumbai, as subscription charges.*

We would appreciate if you help us in our efforts to promote academic excellence.

G P GLOBALIZE RESEARCH JOURNAL OF CHEMISTRY

RNI No. MAHENG/2017/74063 ISSN No. (Print) 2581-5911
ISI Impact Factor: 0.883 (2018)

Volume 3 Issue 1 ❄ July-December 2019

CONTENTS

Papers

RNI No. MAHENG/2017/74063
ISSN No. (Print) 2581-5911
ISI Impact Factor 0.883 (2018)

Oxidation Studies in Irradiated Ultra High Molecular Weight Polyethylene (UHMWPE)

[1]Narayan V.S.*, [2]Ross, M.A., [2]Warner, D., and [2]Gupta, C.E.M.
[1]Anthara Technologies Consulting, 11103 Clarewood Ct., Fort Wayne, IN 46814, USA.
[2]DePuy Orthopaedics Inc., PO Box 988, 700 Orthopaedic Drive, Warsaw, IN 46581, USA.
E-mail: v.narayan@antharatech.com

Abstract
Ultra High Molecular Weight Polyethylene (UHMWPE) is extensively used as an articulating bearing material in artificial hip and knee orthopaedic joints. Ionizing radiation such as gamma (γ) or Electron Beam (EB) is commonly employed to ensure sterility of the implantable device. One of the consequences of exposure to ionizing radiation is crosslinking of the polymer rendering it more wear resistant in the articulating joint. However, this is typically accompanied by increased oxidation potential of the otherwise inert polymer. Stabilization is commonly accomplished by thermal treatment above or below the melt temperature of the polyethylene or with the use of an antioxidant. This study investigates the effect of the radiation source as well as the total dose delivered to the polymer and its effect on the oxidative stability. The oxidation response is monitored on samples that are subject to an accelerated aging protocol that has been established for shelf aging of irradiated UHMWPE. Physical, material and mechanical characteristics of both, γ- as well as EB- irradiated UHMWPE at nominal dose values of 50, 75 and 100 kGy were measured in the non-aged as well as 2-, 4-, 6- and 10-weeks accelerated-aged materials. The results of the study have been reported.

Keywords: *UHMWPE, Oxidation, Ionizing radiation*

Introduction

Osteoarthritis is a widely prevalent clinical issue among the aging and highly active population demographic. While a number of mitigating solutions are offered as short-term solutions, total joint replacement (TJR) has been established as the most widely accepted surgical option for end-stage osteoarthritis. Although a wide number of metallic and ceramic materials are employed in articulating joint bearings, Ultra High Molecular Weight Polyethylene (**UHMWPE**) bearing surfaces remain the gold standard. Over 99% knee joint and currently over 95% hip joint bearings use UHMWPE in the articulation space. This is based on their consistent results and survivorship of ~85% after 15 years[1]. Over the past 40 years, the retrieval, analysis and report of failed devices have been driving factors in continually improving the state-of-the-art in joint replacements[2].

This improvement has been largely driven by the sterilization of the UHMWPE devices using ionizing radiation, such as gamma (γ) or Electron Beam (EB)[3]. While the primary purpose for the employment of ionizing radiation was to sterilize the device, the resulting radiation exposure caused the material to increase in crystallinity[4], thereby increasing the strength and stiffness of the bulk material due to chain and homolytic bond scission of the linear chains of the polymer. The radiation

also effected crosslinking of the otherwise chemically inert UHMWPE molecular chains due to subsequent recombination of the free radicals thereby generated to alter the molecular architecture and yield a network structure[5,6]. The crosslinking rendered the material to be harder, less ductile and improved wear performance. This was a significant improvement in the material to address the primary clinical limitations of the non-crosslinked UHMWPE joint materials - discharge of micro-size particles into the body that induced a response to generate an inflamed periprosthetic membrane that is rich in macrophages and cytokines[7]. This response results in tumors and subsequent loss in bone density in the affected region known as bone resorption or osteolysis. The generation of the harder, more wear-resistant crosslinked UHMWPE has been very effective in addressing this clinical problem. However, one of the detrimental consequences of the radiation exposure is that all of the free radicals generated within the bulk polymer cannot be quenched by the crosslinking reaction due to limited mobility and access of these free radicals to one another in the solid state of the polymer. This is further exacerbated with additional loss in chain mobility due to crosslinking. Thus, the free radicals that remain unreacted have extremely long half life extending to decades in years[8]. Premnath *et al*., have provided a comprehensive overview of the various free radical reactions in play as well as mechanistic pathways through which these reactions occur[8].

These residual free radicals within irradiated UHMWPE could initiate oxidation in the otherwise inert polymer leading to degradative loss in properties leading to UHMWPE implant failure. Oxidation of irradiated UHMWPE orthopaedic implants both, on the shelf in the packaging as well as *in vivo* has been extensively reported to cause adverse effects on the mechanical properties[9,10]. Irradiation of UHMWPE using ionizing radiation sources such as gamma or electron beam generates free radicals which can trigger oxidation if left unaddressed. Clinical and *in vitro* test results have verified oxidative stability by remelting the irradiated UHMWPE materials used in orthopaedic devices[11,12]. Therefore, a large number of current, state-of-the-art UHWPE bearing implants have been generated by crosslinking using ionizing radiation followed by thermal treatment to quench the free radicals above the melt temperature of UHMWPE.

There are two implantable grades of UHMWPE, the requirements for which are specified in ASTM standard F648 – "*Specification for Ultra-High-Molecular-Weight Polyethylene Powder and Fabricated Form for Surgical Implants*" and ISO standard 5834 – "*Implants for surgery—Ultra-high molecular weight polyethylene*". In the standards, these grades are described as Types 1, 2, both currently manufactured by Celanese Corporation and use the trade names GUR 1020 and GUR 1050 respectively. Bothe these grades are widely available and commonly employed in orthopaedic implants. These grades, although chemically identical, differ only in molecular weight with the GUR 1020 UHMWPE typically at an average molecular weight of approx. 3.5 x 10^6 g/mol while GUR 1050 UHWPE has an average molecular weight of 5.5 -6.0 x 10^6 g/mol[13].

In the present study, the comparative response of GUR 1020 UHMWPE materials to oxidation as a function of radiation source (g vs. EB), radiation dose as well as aging period has been characterized. The characterization has involved measurement of the degree of oxidation, as well as material and mechanical property changes that result in the aged materials. Key questions being addressed in this study include:

- Is there are difference in material response depending upon the source of the ionizing radiation?
- How do the properties of the materials vary as a function of the radiation dose?
- Is the oxidation response, and therefore the material property changes influenced by the source of the ionizing radiation?

In order to simulate on-shelf and in vivo oxidation of UHMWPE, the protocol prescribed in ASTM F2003 - "*Accelerated Aging of Ultra-High Molecular Weight Polyethylene after Gamma Irradiation in Air*" was

employed to effect accelerated aging of the materials to various periods. While the outcome of the accelerated aging for different times cannot be accurately correlated to actual on-shelf aging or in vivo oxidation times, the protocol provides relative responses of the various materials. This allows for ranking of the relative oxidative stability of the materials processed under different conditions. The aging periods employed in this study include 0, 2, 4, 6 and 10 weeks. Characterization of the non-aged and aged materials involved:

a. Oxidation Index by FTIR as described in ASTM F 2102
b. Transvinylene Index by FTIR as described in ASTM
c. Crystallinity by DSC per ASTM F 2625
d. Gravimetric Swell Ratio
e. Double Notched Impact per ASTM F 648
f. Ductility as percent elongation at failure in a static tensile test.

Characterization of and monitoring the changes in these properties would enable a better understanding of differences and impact of the two different ionizing radiation types.

Materials and Methods

- GUR 1020 UHMWPE powder (Celanese Corporation) was consolidated into cylindrical 2.5" bars by ram extrusion at MediTECH Medical Polymers. The consolidated material as-is, in a non-irradiated condition and hereafter referred to as **NI-1020**, has been employed in this study as control material.
- Ram extruded and g-irradiated GUR 1020, hereafter referred to as **G-50, G-75, and G-100**, are generated by gamma irradiation at doses of 50, 75 & 100 kGy respectively and subsequently remelted at or above 155ºC.
- Ram extruded and irradiated GUR 1020, hereafter referred to as **E-50, E-75, and E-100**, are generated by e-beam irradiation at Iotron Industries at doses of 50, 75 & 100 kGy respectively and subsequently remelted at or above 155ºC.
- **Accelerated Aging**
  Test samples as needed for the characterization were fabricated and subjected to accelerated aging in accordance with ASTM F-2003 protocol. Accordingly, the samples were placed in a stainless-steel pressure vessel under 5 atm (74 psi) oxygen pressure. The chamber was placed in an oven at room temperature, which was then heated to and maintained at 70ºC for periods ranging from 2 – 10 weeks.

- **Oxidation Response**
  Cubical test samples (10 x 15 x 25 mm) that were fabricated from each material group and subjected to the various accelerated aging periods were characterized for the oxidation response of the material using Fourier Transform Infra-Red (FTIR) Spectroscopy. The FTIR evaluation was performed on three samples from each test group in accordance with ASTM F2102 ("*Standard Guide for Evaluating the Extent of Oxidation in Ultra-High-Molecular-Weight Polyethylene Fabricated Forms Intended for Surgical Implants*") to determine the average oxidation index (OI) values as well as the Transvinylene index (TVI). A Thermo Fisher Scientific spectrometer with a Nicolet iN10 MX microscope (Thermo Fisher Scientific, Madison, WI) and a rectangular aperture of 50 μm x 150 μm was used for all evaluations. To perform the evaluation, each sample was placed in a microtome and 200 μm thin sections were taken. Each section was placed on the motorized stage of the microscope and the edge of the aperture was placed 25 μm in from the edge of the section. At this position, an FTIR absorption spectrum was obtained using 18 scans with a resolution of 4 cm^{-1}. The motorized stage was then moved in increments of 0.5 mm deep and spectra were obtained at each depth.

  The oxidation index (OI) value was determined at each depth by taking the area under the carbonyl absorption peak (>C=O) centered at approximately 1720 cm^{-1} between 1650 to 1850 cm^{-1} and dividing by the area under the reference absorption peak that is associated with $\delta_s(CH_3)$ and $\gamma_w(CH_2)$[14] and centered around 1370 cm^{-1} between 1330 and 1396 cm^{-1}. This allows for normalizing the peak area for

the thickness and allows for quantification of the signal value. For each sample, an average oxidation index was then calculated by averaging the values from each depth for that sample.

- **Transvinylene Index**
  The FTIR spectra generated for the measurement of the oxidation response of all the materials groups under various conditions of accelerated aging was also leveraged for the determination of the Transvinylene Index (TVI) in accordance with the procedure described in ASTM F2381 ("*Standard Test Method for Evaluating Trans-Vinylene Yield in Irradiated Ultra High Molecular Weight Polyethylene Fabricated Forms Intended for Surgical Implants by Infrared Spectroscopy*"). The TVI was calculated by taking the area under the Transvinylene peak between 955 and 978 cm^{-1} and dividing by the area under the normalization peak between 1371 and 1404 cm^{-1}.

- **Percent Crystallinity**
  The % crystallinity in the samples was determined using a Differential Scanning Calorimeter, or DSC (TA Instruments, Schaumburg, IL). The Q1000 (Serial# 1000-0392, BT# 69617) calorimeter was employed and measurements were made in accordance with the procedure described in ASTM F2625 ("*Measurement of Enthalpy of Fusion, Percent Crystallinity, and Melting Point ·of Ultra-High-Molecular Weight Polyethylene by Means of Differential Scanning Calorimetry*"). The DSC samples were microtomed to a thickness of 400µm from 10 x 15 x 25 mm blocks. These blocks were fabricated from each material group and subjected to the various accelerated aging periods prior to testing. Three 5 mm diameter circular disc samples were punched for each material group. These punched samples were then weighed and tested. The DSC scans were run at 10 ºC/min from 30 to 180 ºC under nitrogen environment.

- **Gravimetric Swell Ratio**
  The swell ratio was determined using DePuy Work Instruction WI 4949 that is based on ASTM D2765, Method C (Standard Test Method for Determination of Gel Content and Swell Ratio of Crosslinked Ethylene Plastics) using six 8.13 x 8.13 x 8.13 mm cubes for each material group. The swell ratio measurements were conducted on the DePuy Synthes gravimetric swell ratio tester (DePuy Orthopaedics, Warsaw, IN; BT# 69020, Serial# 1200603907005).

- **Double Notched Izod (DNI) Impact Toughness**
  Impact toughness properties were evaluated in accordance with ASTM F648 ("*Specification for Ultra-High-Molecular-Weight Polyethylene Powder and Fabricated Form for Surgical Implants – Annex 1: Impact Strength*") using six double-notched Izod impact sample specimens with a Ceast double notched Izod tester (Instron, Pianezza, Italy; BT# 69293, Serial# 14153). The machine test samples were stabilized for 24 hours at standard lab conditions prior to test.

- **Ductility as % Elongation to Failure**
  Tensile testing was performed on six samples in accordance with ASTM D638 using Type IV samples and a MTS Insight 5 (MTS Systems Corporation, Eden Prairie, MN; BT# 69609, Serial# 10200470). The machined test samples were stabilized for 24 hours prior to test and then tested at standard lab conditions. The initial crosshead speed was 5.08 mm/min and then increased to 50.8 after 1.27 mm of excursion.

Results and Discussion

All the characterization data is reported below. Data however, is not available for the following:

- 6-week aged NI-1020 samples as the material was compromised in the aging chamber due to power outage and therefore measurements on these samples were not performed.

- Gravimetric Swell Ratio measurements for the non-irradiated NI 1020 samples at all aging conditions since these are not crosslinked and woud not yield a meaningful result in the swell testing.

- The E-beam materials, regardless of the radiation dose, were more severely oxidized at 10 weeks aging and samples for FTIT, DSC and Swell ratio testing could not be generated.

Oxidation Behavior

The oxidation response has been measured by FTIR in accordance to the procedure in ASTM F2102. The average value for all sample specimens measured is then computed and reported below in Table 1.

Table 1: Oxidation Index values for different Aging Conditions

Aging Period	NI-1020	50-E	50-G	75-E	75-G	100-E	100-G
Non-Aged	0.032 ±0.006	0.050 ±0.009	0.056 ±0.009	0.045 ±0.016	0.070 ±0.023	0.079 ±0.026	0.061 ±0.009
2-week Aged	0.036 ±0.012	0.051 ±0.014	0.069 ±0.018	0.054 ±0.007	0.077 ±0.013	0.027 ±0.013	0.057 ±0.011
4-week Aged	0.045 ±0.015	0.068 ±0.016	0.074 ±0.005	0.096 ±0.015	0.054 ±0.013	0.075 ±0.016	0.062 ±0.010
6-week Aged	*	0.225 ±0.012	0.086 ±0.011	0.253 ±0.084	0.114 ±0.028	0.223 ±0.029	0.142 ±0.019
10-week Aged	0.220 ±0.015	**	0.600 ±0.059	**	0.513 ±0.253	**	0.704 ±0.059

* Data not measured as samples were compromised in aging chamber
** Too brittle to yield samples for measurement

Consistent with previous studies[15,16,17], there is a progressive increase in the oxidation index over 10 weeks of aging. All materials show little or no change in oxidation index up to 4 weeks aging. Any small differences in values noted up to this point are insignificant as, below an oxidation index of 0.1, there is considerable noise in the FTIR signal. However, the materials begin to separate out in oxidation response at the 6-week mark. Onset of oxidation is noted in all the materials. Statistically higher oxidation index values are noted for the e-beam irradiated materials relative to their gamma-irradiated counterparts. The trend is confirmed at the 10-week mark wherein the e-beam materials are too brittle to measure. While there is progression in oxidation in the gamma materials, they are still ductile enough to be microtomed and characterized even at the 10-week aged mark.

Transvinylene Index

Previous studies[18,19] have shown that the TVI is a function of the radiation dose applied to the polymer. The results are summarized in **Table 2**.

Table 2: Transvinylene Index values for different Aging Conditions

Aging Period	NI-1020	50-E	50-G	75-E	75-G	100-E	100-G
Non-Aged	-0.004 ±0.001	0.020 ±0.002	0.015 ±0.000	0.026 ±0.007	0.018 ±0.000	0.030 ±0.002	0.024 ±0.000
2-week Aged	-0.004 ±0.001	0.017 ±0.000	0.015 ±0.000	0.022 ±0.004	0.018 ±0.001	±0.032 ±0.005	0.024 ±0.001
4-week Aged	-0.004 ±0.000	0.021 ±0.001	0.015 ±0.000	0.026 ±0.004	0.018 ±0.001	0.038 ±0.001	0.025 ±0.001
6-week Aged	*	0.019 ±0.004	0.015 ±0.000	0.026 ±0.007	0.019 ±0.000	0.040 ±0.001	0.024 ±0.000
10-week Aged	-0.005 ±0.001	**	0.014 ±0.000	**	0.018 ±0.000	**	0.022 ±0.001

* Data not measured as samples were compromised in aging chamber
** Too brittle to yield samples for measurement

The nonirradiated NI-1020 samples did not yield a meaningful result for TVI as there was no exposure to ionizing radiation and hence there were no Transvinylene groups generated. While the transvinylene functionality is unchanged due to aging, it is seen that the E-beam irradiated materials show a somewhat higher TVI relative to the gamma analogs at the same radiation dose. While this needs to be verified further, it is likely that the higher intensity of the E-beam generates more transvinylene groups as compared to the gamma analogs at the same radiation dose.

Percent Crystallinity

The melt endotherm was integrated between 50ºC and 160ºC. % Crystallinity was then calculated using a reference heat of fusion value of 289.5 J/g for 100% crystalline polyethylene (PE). The response of the percent crystallinity in the materials to irradiation as well as aging in the present study has been summarized in **Table 3**. The trends seen here are consistent with that observed in FTIR measurements. While some small change is noted at 6 weeks, the gamma materials as well as the non-irradiated UHMWPE at 10 weeks aging show values at or about 70%**.** This has been associated with significant oxidation in a previous study[20].

Table 3: Percent Crystallinity values for different Aging Conditions

Aging period	NI-1020	50-E	50-G	75-E	75-G	100-E	100-G
Non-Aged	60 ±3.0	55.2 ±0.6	51.9 ±3.0	53.1 ±2.1	54.2 ±0.4	53 ±1.7	53.4 ±0.7
2-week Aged	59.1 ±1.8	55.6 ±2.3	54.2 ±3.6	55.8 ±0.4	53.6 ±3.0	54.1 ±2.1	55.6 ±2.3
4-week Aged	60.5 ±2.2	52.5 ±1.5	54.5 ±1.2	54.4 ±2.8	58.3 ±1.4	56.6 ±2.4	57.1 ±1.6
6-week Aged	*	65.9 ±2.4	58.2 ±2.8	66.5 ±1.3	59 ±2.3	62.9 ±1.2	60.6 ±0.8
10-week Aged	71.2 ±3.0	**	74 ±0.8	**	68.7 ±4.0	**	73.6 ±1.8

* Data not measured as samples were compromised in aging chamber
** Too brittle to yield samples for measurement

Gravimetric Swell Ratio

The gravimetric swell ratio indicates the degree of crosslinking in the polymer as a result of exposure to the ionizing radiation. It is the ratio of the swollen volume of the polymer in a suitable solvent to the original volume of the cubical sample of the polymer in a dry state. Higher the crosslinking, smaller the degree of swelling. The steady state swell ratio, q_s, is calculated after 48 hours of drying according to Equation 1 below:

Swell ratio $q_s = [(W_g – W_d) / (W_o – W_e)] * K+1$..... (1)

Where,

W_g = weight of swollen gel after immersion period

W_d = weight of dried gel

W_o = original polymer weight

W_e = weight of extract

K = ratio of density of polymer to that of the solvent at the immersion temperature

Given the steady state swell ratio, *qs*, of a polymer immersed in a specific solvent at a particular temperature, the crosslink density, molecular weight between crosslinks, and number of crosslinks/chain can be computed if one knows the Flory interaction parameter, c_1, for the polymer-solvent system. Based on Flory's network theory[21,22], the following expression is derived for the crosslink density, n_d, as a function of the steady state swelling ratio, the Flory interaction parameter, and, the ϕ_1-, the molar volume of the solvent.

$$\upsilon_d = -\frac{1n(1-q_s^{-1}) + q_s^{-1} + X_i q_{s^{-2}}}{\phi_1(q_s^{-1/3} - q_s^{-1/2})} \quad (2)$$

Molecular weight between cross-links, M_c

$$M_c = (\bar{\upsilon}\upsilon_d)^{-1} \quad (3)$$

Where **n** is the specific volume of the polymer. Therefore, the crosslink density (n_d) is given by

$$n_d = M_0 / M_c \quad (4)$$

The results are summarized in **Table 4.**

Table 4: Gravimetric Swell Ratio values for different Aging Conditions

Aging Period	NI-1020	50-E	50-G	75-E	75-G	100-E	100-G
Non-Aged	N/A	4.41±0.30	3.66±0.05	3.27±0.17	3.25±0.07	3.18±0.11	3.07±0.03
2-week Aged	N/A	4.75±0.43	3.76±0.10	3.35±0.16	3.35±0.05	3.22±0.07	3.13±0.04
4-week Aged	N/A	4.92±0.49	3.91±0.07	3.17±0.10	3.31±0.05	3.11±0.08	3.07±0.04
6-week Aged	N/A	5.66±0.72	3.82±0.15	3.49±0.23	3.52±0.14	3.68±0.23	3.21±0.06
10-week Aged	N/A	*	4.80±0.52	*	4.97±0.21	*	3.77±0.28

* Breakdown of gel in solvent

The results do not point to a big difference in the extent of crosslinking at any given dose between g- or EB-irradiated UHWPE as the swell ratios as very comparable. It is however seen that the response to aging is consistent with measurements of previous properties. The breakdown in network is so thorough for the EB materials that no measurement of swell ratio is possible at 10 weeks. The g-irradiated materials hold up better to the aging process.

Double Notched Izod (DNI) Impact Toughness Response to Oxidation

While impact toughness of most polymers is usually evaluated using unnotched samples, UHMWPE is an extremely tough material. As a result, unnotched samples do not break. Therefore, double notched samples are used in this study as prescribed in ASTM F648. The characterization of the DNI impact toughness for all the material groups were monitored as a function of aging and summarized in **Table 5**.

Table 5: Double Notched Izod Impact Toughnes for different Aging Conditions

Aging period	NI-1020	50-E	50-G	75-E	75-G	100-E	100-G
Non-Aged	135.3±2.7	77.9±3.5	73.4±1.3	71.6±2.6	69.3±1.5	59.5±1.9	57.3±5.8
2-week Aged	139.4±2.3	88.8+9.6	74.5±0.8	72.5±2.7	68.7±1.8	58.3±2.0	58.9±2.0
4-week Aged	148.9±3.7	90.0±104	77.5±1.6	72.4±6.9	69.9±1.2	60.3±4.3	60.4±1.5
6-week Aged	*	32.3±9.4	79.1±2.6	50.6±11.8	69.7±4.6	27.4±5.6	43.8±14.1
10-week Aged	27.4±5.1	1.4±0.7	23.0±1.8	2.4±0.7	23.1±7.0	1.2±0.3	10.4±2.4

* Data not measured as samples were compromised in aging chamber

While the remelted materials show good retention of properties at the end of 4 weeks, thereafter the trends noted in the FTIR measurements are replicated. The EB-materials start showing loss in properties at 6 weeks aging. While the gamma materials, particularly at 50 and 75 kGy continue to remain stable, the 100 kGy gamma material shows some loss, though it is not statistically significant from the value at 4 weeks aging. At 10 weeks, all materials, including the non-irradiated UHMWPE show oxidative loss. The EB materials show consistently lower properties than the corresponding gamma materials beyond 6-weeks aging regardless of the radiation dose.

Ductility as Percent Elongation at Failure in Static Tensile Test

From the static tensile testing performed on ASTM Type IV tensile specimens of the various material groups, the percent elongation at failure provides insights into the ductility of the materials. As the materials age, they become more brittle and, consistent with the impact toughness results, lose ductility. This is evidenced from the drop in the percentage elongation at failure of the samples with aging period. The results of the testing are summarized in **Table 6**.

Table 6: Percent Elongation at Failure values for different Aging Conditions

Aging Period	NI-1020	50-E	50-G	75-E	75-G	100-E	100-G
Non-Aged	425.35 ±20.08	333.45 ±33.33	297.97 ±33.72	289.07 ±31.10	289.82 ±20.47	244.05 ±16.87	243.72 ±11.49
2-week Aged	406.34 ±26.94	333.16 ±37.61	300.46 ±39.28	300.01 ±27.30	276.70 ±27.68	263.58 ±15.90	265.29 ±15.43
4-week Aged	366.97 ±46.51	330.45 ±43.54	320.08 ±16.00	300.81 ±20.44	266.70 ±31.65	253.92 ±14.97	251.61 ±8.10
6-week Aged	*	335.49 ±42.47	335.82 ±21.74	296.67 ±30.92	289.58 ±27.02	286.12 ±13.67	239.54 ±13.14
10-week Aged	402.75 ±34.13	2.33 ±0.44	284.75 ±43.02	4.65 ±2.49	279.03 ±47.54	2.24 ±0.80	230.50 ±25.74

* Data not measured as samples were compromised in aging chamber

Once again, the trends noted in other properties is reflected here in the loss of ductility. The EB materials are so much oxidized and degraded by 10 weeks aging that virtually all ductility is lost. The gamma materials still retain up to approximately 250% elongation at break though these values are lower than that demonstrated by the aged nonirradiated UHMWPE, NI-1020.

Conclusions

Thus, the findings provide valuable insights into the three fundamental questions raised at the start of the study:

* There are measurable difference in material response depending upon the source of the ionizing radiation.
* While the materials generated by either radiation source show comparable properties at the same radiation dose, EB materials have a measurably higher amount of transvinylene groups than the gamma materials and are therefore possible more vulnerable to oxidation.
* The oxidation response, and therefore the material property changes are influenced by the source of the ionizing radiation. While all materials upon irradiation and remelting show good stability for at least 4 weeks of ASTM aging on par with non-irradiated UHMWPE, the e-beam materials show greater scatter in response upon aging beyond 4 weeks than the corresponding gamma materials and tend to oxidize faster.
* The gamma materials show better stability than the e-beam materials in their material and mechanical properties and respond similar to non-irradiated UHMWPE, particularly at lower doses of 50 and 75 kGy.

Acknowledgement

The authors wish to thank Lou Matrisciano, Restoration Medical Polymers for his help with processing and generating EB-irradiated samples.

References

1. Gomez-Barrena E., Medel F., Puertolas J.A., 2009, *Open Orthop J*., **3,** 115.

2. Harris, W.H., Clinical Considerations, in Biological, Material, and Mechanical Considerations of Joint Replacement, ed. B.F. Morrey, 1993, New York, NY: Raven Press, p.1-11.

3. Kurtz, S.M., Muratoglu, O.K., Evans, M., Edidin, A.A., 1999, *Biomaterials*, **20,** 1659.

4. Bostrom, M.P., Bennett, A.P., Rimnac, C.M., Wright, T.M., 1994, *Clin. Orthop.,* **309,** 20.

5. Grobbelaar, C. J.; du Plessis, T. A. and Marais, F., 1978, *J. Bone and Joint Surg.,* **60-B(3),** 370.

6. Oonishi, H., Takayama, Y. and Tsuji, E., 1992, *Radiat. Phys. Chem.,* **39,** 495.

7. Purdue PE, Koulouvaris P. and Potter H.G., et al. 2007, *Clin. Orthop. Relat. Res.,* **454,** 251.

8. Premnath V, Harris, W.H., Jasty, M. and Merrill, E.W., 1996, *Biomaterials*, **17(18),** 1741.

9. Rimnac, C.M., Klein, R.W., Betts, F. and Wright, T.M., 1994, *J. Bone Joint Surg.*, **76 A,** 1052.

10. Collier, J.P., Sperling, D.K., Currier, J.H., Sutula, L.C., Saum, K.A. and Mayor, M.B., 1996, *J. Arthroplasty* **11(4),** 377.

11. Muratoglu, O.K., Bragdon, C.R., D.O. O'Connor, Jasty, M. and Harris, W.H., 1999, *J. Arthroplasty* **16 (2),** 149.

12. McKellop, H., Shen, F.-W., Lu, B., Campbell, P. and Salovey, R., 1999, *J. Orthop. Res*., **17(2)**, 157.

13. Kurtz, S.M., ed., UHMWPE Biomaterials Handbook, 3rd ed., 2016, Elsevier, NY, p.12.

14. Krimm, S., Liang, C.Y. and Sutherland, G.B.B.M., 1956, *J. Chem. Phys.,* **25(3),** 549.

15. Buchanan, F.J. and Sim, B., Downes, S., 1999, *Biomaterials* **20,** 823.

16. Sun DC, Stark C. and Dumbleton JH., 1996, ACS Symposium Series, Irradiation of polymers. Washington DC: American Chemical Society, 340.

17. K. Greer, 2003, Transactions of the Society for Biomaterials, 28, 378.

18. Lyons, B.J., Johnson, W.C. "Radiolytic formation and decay of trans-vinylene unsaturation in polyethylene", Reichmanis, E., Frank, C.W., O'Donnell J.H., (Eds.), 1993, Irradiation of Polymeric Materials: Processes, Mechanisms, and Applications, American Chemical Society, Washington, DC.

19. Johnson, W.C. and Lyons, B.J., 1995, *Radiat. Phys. Chem.* **46,** 829.

20. Narayan V.S., King R. and Senyurt A.S., 2010, *Transactions of the Orthopaedic Research Society*, **56,** 2316.

21. Flory, P. J., Principles of Polymer Chemistry, Ithaca and London, Cornell University Press, 1953.

22. Flory, P. J. and Reihner, J., 1943, *J. Chem. Phys.,* **11(11)**, 521.

RNI No. MAHENG/2017/74063
ISSN No. (Print) 2581-5911
ISI Impact Factor 0.883 (2018)

In-situ Reduction of Gold Nanoparticles in Alginate Film Matrix for Application in Surface Enhanced Raman Scattering

Abhishek Das[1,3,*], Himanshi[4], Ridhima Chadha[1], Nandita Maiti[1,3], Suman Neogy[2] and Sudhir Kapoor[1,3,*]
[1]Radiation and Photochemistry Division,
[2]Mechanical Metallurgy Division,
Bhabha Atomic Research Centre, Mumbai-400085, India.
[3]Homi Bhabha National Institute, Anushaktinagar, Mumbai-400094, India.
[4]Department of Chemistry, Indian Institute of Technology Roorkee, Roorkee-247667, India.
Email: abhidas@barc.gov.in; sudhirk@barc.gov.in

Abstract
Low cost gold nanoparticle (GNP) loaded polymeric SERS substrates were synthesized for probable application in on-site trace-level sensing of organic dyes. Water soluble transparent sodium alginate films were prepared by cast-drying method. The films were cross-linked using an aqueous mixture of Ca^{2+} and Fe^{3+}. Au^{3+} ions loaded in the above films by sorption were further reduced by 0.05 M glucose solution at 60°C. The films were characterized by UV-vis spectroscopy, infrared spectroscopy and transmission electron microscopy (TEM). The synthesized films were further studied for detection of crystal violet (CV), a fungicide, by surface enhanced Raman scattering technique (SERS). The observed detection limit of CV in the above films was found to be 10 nM or ~4 ppb.

Keywords: *SERS, Alginate films,* in-situ *gold nanoparticle synthesis, trace level detection, Cast-dry films, glucose mediated reduction*

Introduction

Gold nanoparticle (GNP) substrates are widely used for trace level detection of organic molecules by surface enhanced Raman scattering (SERS) technique[1, 2]. Noble metal nanoparticles exhibit unique optical property wherein free electrons present on the surface of the nanoparticle oscillate collectively[3] upon excitation by an electromagnetic radiation of a specific wavelength which is dependent on the size[4], shape[5] and dielectric constant[6] of the material. The above resonance condition is called surface plasmon resonance. The surface plasmon creates a near field[7] in proximity to the surface of the nanoparticle. When two or more noble metal nanoparticles come closer to each other, the near field of each nanoparticle interact or couple giving rise to a resultant enhanced electric field at the junction of the particles[8]. The above junction is often referred to as hot-spot[9]. Any molecule in the vicinity of the above hot-spot is most likely to experience enhanced electric field which may polarize its electron cloud. The molecule may ultimately stabilize by scattering back the absorbed energy. The changes in the near field of the coupled plasmon are recorded in far-field in the form of UV-vis optical absorption[10] and SERS[11]. Designing of substrates made up of GNPs or silver nanoparticles (AgNPs) which

would absorb analytes in its hot-spots to show SERS signal at low concentration has been the aim of researchers working in the field of SERS sensing[12]. SERS substrates can be either in the form of solution or as solid. Both have their own advantages and disadvantages. Noble metal nanoparticles in solution are very sensitive to addition of analytes, as it often induces agglomeration[13,14] leading to generation of hot-spots. As a result, very low concentrations of analyte can be detected in solutions containing noble metal nanoparticles. Most commonly known GNPs and AgNPs can be prepared in solution by citrate[15] and borohydride[16] method. The most noted drawback of these solutions is that the solutions tend to agglomerate if the temperature and pH conditions are not maintained[17]. Solid substrates on the other hand are generally synthesized by electrochemical deposition[18,19] of noble metals on rough surfaces or by chemical vapor deposition[20]. The above substrates can be stored for long time without any changes as well as can be carried outdoors for on-site detection using handheld Raman spectrometer[21]. The detection limits of the solid substrates are observed to be comparatively higher than their solution counter-parts as the metal nanoparticles are immobilized on a solid matrix which reduces the control over agglomeration of particles upon adsorption of analytes. Thus, it can be said that solution based SERS substrates are suited for low concentration detection whereas solid SERS substrates are suited for on-site detection[22].

Recently, SERS substrates were developed by immobilizing GNPs in a filter paper[23].Silver nanoparticles can also be coated on the surface of glass for SERS sensing[14]. But such a coating requires sophisticated handling as scratch on the surface can remove the layer of silver nanoparticles. The aim of this work was to synthesize GNPs in a solid matrix where plasmonic nanoparticles are not dislodged from the matrix. Polymeric matrixes were one of the most important choices. Very few reports are available where polymeric films are used to immobilize GNPs for application in SERS sensing[24]. The polymer used in this study is sodium alginate. Sodium alginate is a biopolymer obtained from brown algae. Alginic acid is a biopolymer consisting of alternating units of α-L-guluronic acid (G) and β-D-mannuronic acid (M)[25]. Sodium replaces the acidic proton in the carboxylic groups of the alginic acid and makes the biopolymer highly soluble in water. Cross-linking of alginate polymer is one of the simplest methods of cross-linking. Addition of sodium alginate solution drop-wise in Ca^{2+} or Ba^{2+} solution leads to cross-linking of alginate as bivalent metal ion binds to two adjacent carboxylic groups present on the skeleton of the polymer. The above cross-linked structure is well explained by "egg-box model", where cavities are created for sorption of metal ions by residual carboxylic groups[26]. Alginate biocomposites can be obtained in the form of beads[27] or films[28] depending on the application. GNPs were also synthesized in alginate anisotropic structures for sensing applications[29]. There are reports where mixtures of bivalent calcium ion and trivalent ferric ions have been used to cross-link alginate[30]. Ferric ions strongly bind alginate and have one free valency which can be used for extraction of anions[31]. In this work, monovalent tetrachloroaurate ions were added to cross-linked alginate films for adsorption via replacement of Ca^{2+} or Fe^{3+} ions or both. The Au^{3+} ions loaded in the films by sorption were further reduced by glucose to synthesize GNPs *in-situ*. The GNP loaded films were then used for detection of crystal violet (CV), a dye and a fungicide, using SERS.

Materials and Methods

Gold (III) chloride hydrate (99.995% trace metal basis), sodium alginate (synthetic), crystal violet (90.0%), polyvinyl pyrollidone (PVP, avg mol wt 40,000), n-hexane (95%), calcium nitrate (99%), ferric chloride (97%) and D-glucose (99.5%) were obtained from Sigma-Aldrich and were used as received. Hydrochloric acid (30%) was obtained from Merck. All the experiments were performed in Millipore purified water.

Synthesis of GNP loaded Alginate Films

2% (w/v) sodium alginate solution and 8% (w/v) PVP solution were mixed in the ratio of 9:1 by volume at 25ºC. 20 mL of the above mixture was stirred for half an hour followed by addition of 1 mL n-hexane while

stirring vigorously. The above mixture was spread on a perfectly flat petri-dish with an internal diameter of 9 cm and air-dried to form a robust transparent film. The dried film was removed later from the petri-dish using a pair of forceps. The above water-soluble film was cut into pieces of dimension: 1 cm x 1 cm. All the cut films were washed in acetone and air-dried in order to remove any organic impurities. The above films were added to cross-linking solution consisting of 0.1M Ca^{2+} and 0.1M Fe^{3+} ions in various ratio by volume while stirring for 2 hours. Each of the above water insoluble cross-linked films were dipped in 1 mL of $3x10^{-3}$ M $HAuCl_4$ solution for 1 day. Au^{3+} containing cross-linked alginate films were immersed in 5 mL of 0.05 M D-glucose solution in a 10 mL volumetric flask and heated in a boiling water bath for *in-situ* reduction of Au^{3+} to GNPs. Red coloured GNP loaded alginate films were further used for SERS detection of CV.

Experimental Techniques

The absorption spectra of the solutions, used in this work, were recorded using UV-vis absorption spectrophotometer (JASCO V-650). The Raman spectra of solid CV and SERS spectra of the solutions were recorded using 632 nm laser line from a He-Ne laser. The sample solutions were taken in a standard 1×1 cm^2 quartz cuvette and the Raman scattered light was collected at 180° scattering geometry and detected using a CCD (Synapse) based monochromator (LabRAM HR800, Horiba JobinYvon, France) together with an edge filter. The spot size on the sample was ~0.5 mm in diameter, and the laser power at the sampling position was 10 mW for the excitation wavelengths of 632 nm. The Raman band of a silicon wafer at 520 cm^{-1} was used to calibrate the spectrometer, and the accuracy of the spectral measurement was estimated to be better than 1 cm^{-1}. Transmission electron microscope (TEM) images and selective area electron diffraction (SAED) patterns for the samples were taken on JEOL 1200 EX Microscope operated at an accelerating voltage of 200 kV. Fourier transform infrared (FT-IR) spectra were recorded using Shimadzu FT-IR instrument.

Results and Discussion

Robust water-soluble alginate (Alg) films were immersed in cross-linking solution after washing in extrapure acetone. This washing in acetone is necessary to remove organic impurities present on the surface. Solubility of sodium alginate in acetone is much lower than that in water. Five washed Alg films were dipped in 20 mL of cross-linking solutions comprising of mixture of 0.1 M $Ca(NO_3)_2$ and 0.1 M $FeCl_3$ in the ratio of 1:0, 3:1, 4:1, 5:1 and 6:1. The above cross-linked films were further immersed in 1 mL of $3x10^{-3}$ M Au^{3+} solution to study the extent of absorption of Au^{3+} by the films by recording the UV-vis absorption spectra at regular intervals for 1 day. The absorption maximum of $AuCl_4^-$ appears at ~310 nm for $3x10^{-3}$ M $HAuCl_4$. As the concentration of Au^{3+} was decreased, the absorption maximum was found to be blue shifted. This may be due to the overlap of more intense 220 nm peak and less intense 310 nm peak of $HAuCl_4$. UV-visible absorption spectra of a series of different concentrations are shown in Fig. 1a. Calibration curve for quantitative detection of concentration of $HAuCl_4$ can be obtained by plotting absorbance vs. concentration at a specific wavelength. Fitting of the above curve were fitted with least square fit method[32]. The coefficient of determination (R^2) for each fit at different wavelength predicts the accuracy of the method (Fig. 1b)[32]. From Fig. 1b, it can be seen that R^2 is lower in the range 300 to 345 nm due to overlap of 220 nm peak. At 350 nm, the R^2 value is 0.99973, which indicates that determination of concentration of $HAuCl_4$ can be carried out with minimal error at this wavelength. The absorbance of the supernatant in the above cases at 350 nm vs. time is shown in Fig. 1c. More than 60% decrease in absorbance was observed in the case of the cross-linking solution containing Ca^{2+} and Fe^{3+} in the molar ratio of 1:0 and 5:1. Based on the above observation, films cross-linked with 0.1 M $Ca(NO_3)_2$were considered for further experiments and the film was assigned name 'Ca-Alg' film. Similarly, films cross-linked with 0.1 M $Ca(NO_3)_2$ and 0.1 M $FeCl_3$ in the ratio 5:1, were considered for further experiments and called 'Ca-Fe-Alg' film.

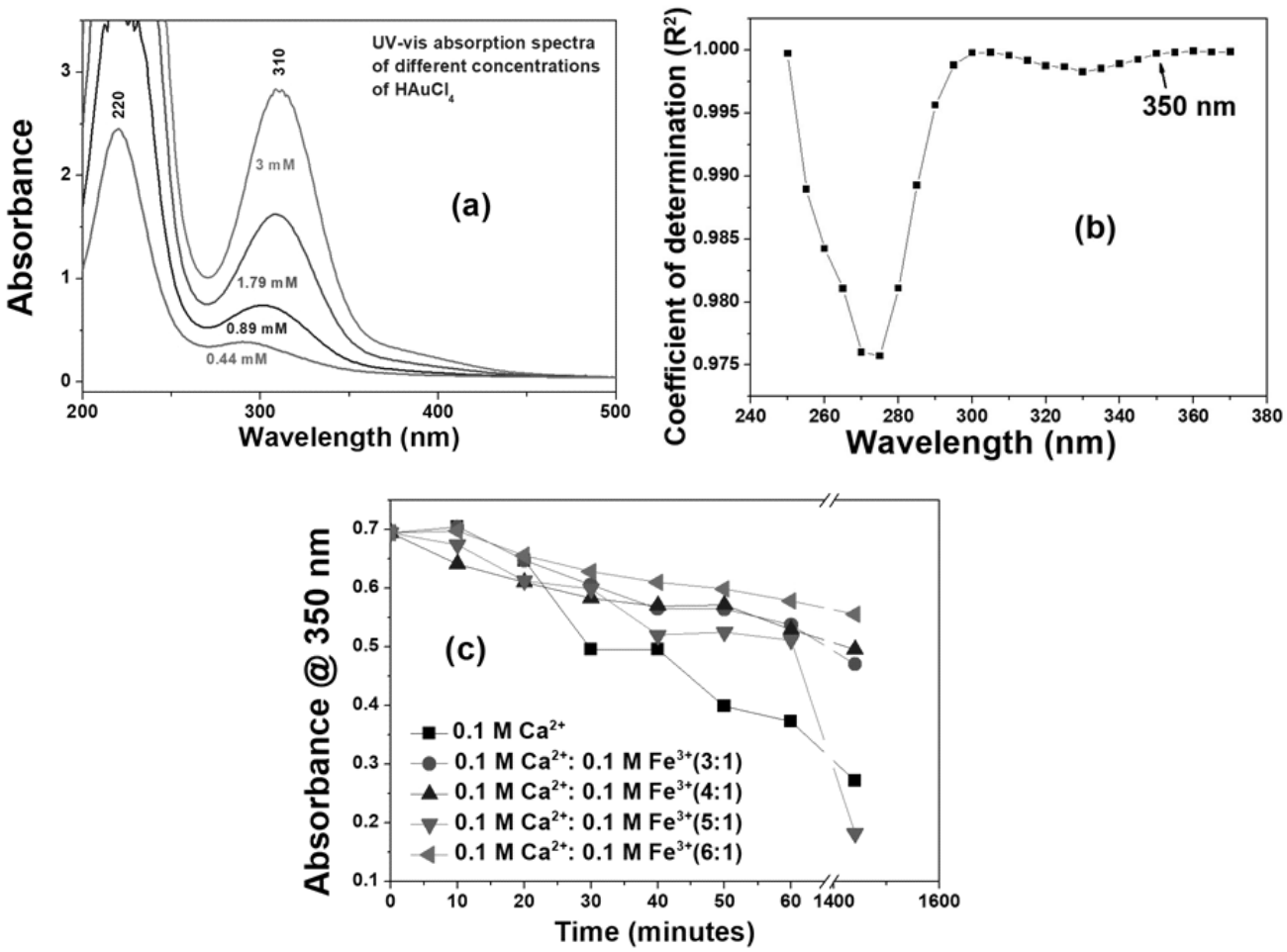

Fig. 1: (a) UV-vis absorption spectra of different concentrations of $HAuCl_4$,
(b) Coefficient of determination (R^2) for varying wavelength obtained from fitting of absorbance vs. concentration of $HAuCl_4$ solutions at fixed wavelength, and
(c) Absorbance of the supernatant of the cross-linked films with Ca^{2+} to Fe^{3+} content (molar ratio) of 1:0, 3:1, 4:1, 5:1 and 6:1 immersed in a solution of $3x10^{-3}$ M Au^{3+} recorded at regular intervals.

The images of the transparent film, cross-linked film, Au^{3+} loaded cross-linked film and GNP loaded cross linked films are shown in Fig. 2. It can be seen that cross-linking of the film only in Ca^{2+} turns transparent film into translucent white colour, whereas in presence of Fe^{3+}, the film turns light yellow (Fig. 2b). Absorption of Au^{3+} imparts a yellowish tinge to all the cross-linked films (Fig. 2c). Further *in-situ* reduction of Au^{3+} absorbed in the films by D-glucose turns the films reddish due to formation of GNPs as shown in Fig. 2d. The extent of cross-linking of alginate matrix of the films depends upon the charge density of the cross-linking ion. Surface charge density of Fe^{3+} is higher than that of Ca^{2+}. Brus et al. has demonstrated that cross-linked alginate polymer with higher surface charge density on cross-linking cation show higher extent of chemical exchange due to carboxylic groups[33]. Thus, Fe^{3+} may contribute more towards increasing the adsorption of $AuCl_4^-$ by chemical exchange, in comparison to Ca^{2+}.

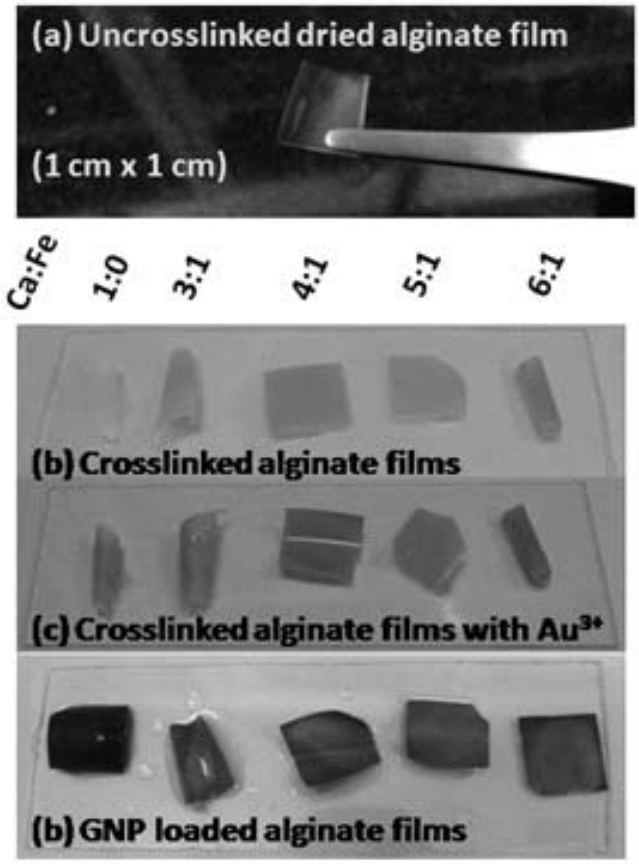

Fig. 2: Photograph of (a) uncross-linked dried transparent alginate film, (b) cross-linked alginate films, (c) Au^{3+} loaded cross-linked alginate films, and (d) GNP loaded alginate films.

GNPs loaded Ca-Alg and Ca-Fe-Alg are designated as Au/Ca-Alg and Au/Ca-Fe-Alg films respectively. The extent of GNPs lost in Au/Ca-Alg and Au/Ca-Fe-Alg films were further measured by recording the supernatant of the reduction reaction by glucose in boiling water bath for 3 minutes as shown in Fig. 3. In case of Au/Ca-Alg and Au/Ca-Fe-Alg films, leached out GNPs showed SPR at 526 nm and 550 nm respectively, as shown in Fig. 3. Moreover, the absorbance of GNPs in case of Au/Ca-Alg films were found to be lower than that of Au/Ca-Fe-Alg films indicating that extent of retention of GNPs is better in case of the former. The SPR of Au/Ca-Fe-Alg films appeared at a higher wavelength than that of Au/Ca-Alg films.

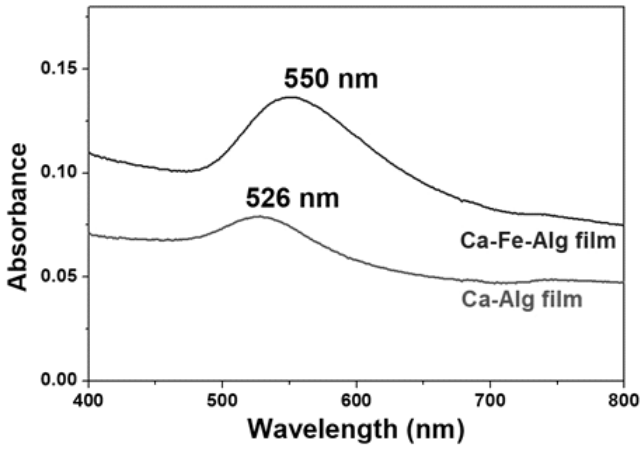

Fig. 3: UV-vis absorption spectra of leached GNPs during reduction of Au^{3+} in Ca-Alg and Ca-Fe-Alg films by 0.05 M glucose for 3 minutes in boiling water bath.

The above supernatant solutions, whose UV-vis absorption spectrum is shown in Fig. 3, were used for recording TEM image as shown in Fig. 4. It can be seen in Fig. 4a, that particles of size ~10 nm are clustered together. Around the particles a dark shadow is also observed which may be due to the capping of alginate. The selected area electron diffraction (SAED) pattern shown in the inset of Fig. 4a shows that the pattern corresponding to Au(0)[34]. Sharp diffraction pattern indicate that the particles are fairly crystalline. In Fig. 4b, a cluster of particles of size ~5 nm is observed. The particles are in close proximity to one another compared to particles observed in Fig. 4a. This suggests that in case of Au/Ca-Fe-Alg (Fig. 4b), there is a possibility of plasmon coupling which may show lead to observation of SPR band at higher wavelength. The above inference is supported by the UV-vis absorption spectra of Au/Ca-Fe-Alg as shown in Fig. 3. The presence of strong plasmon coupling also suggests that the hotspots generated in Au/Ca-Fe-Alg film may be useful for SERS based sensing[35].

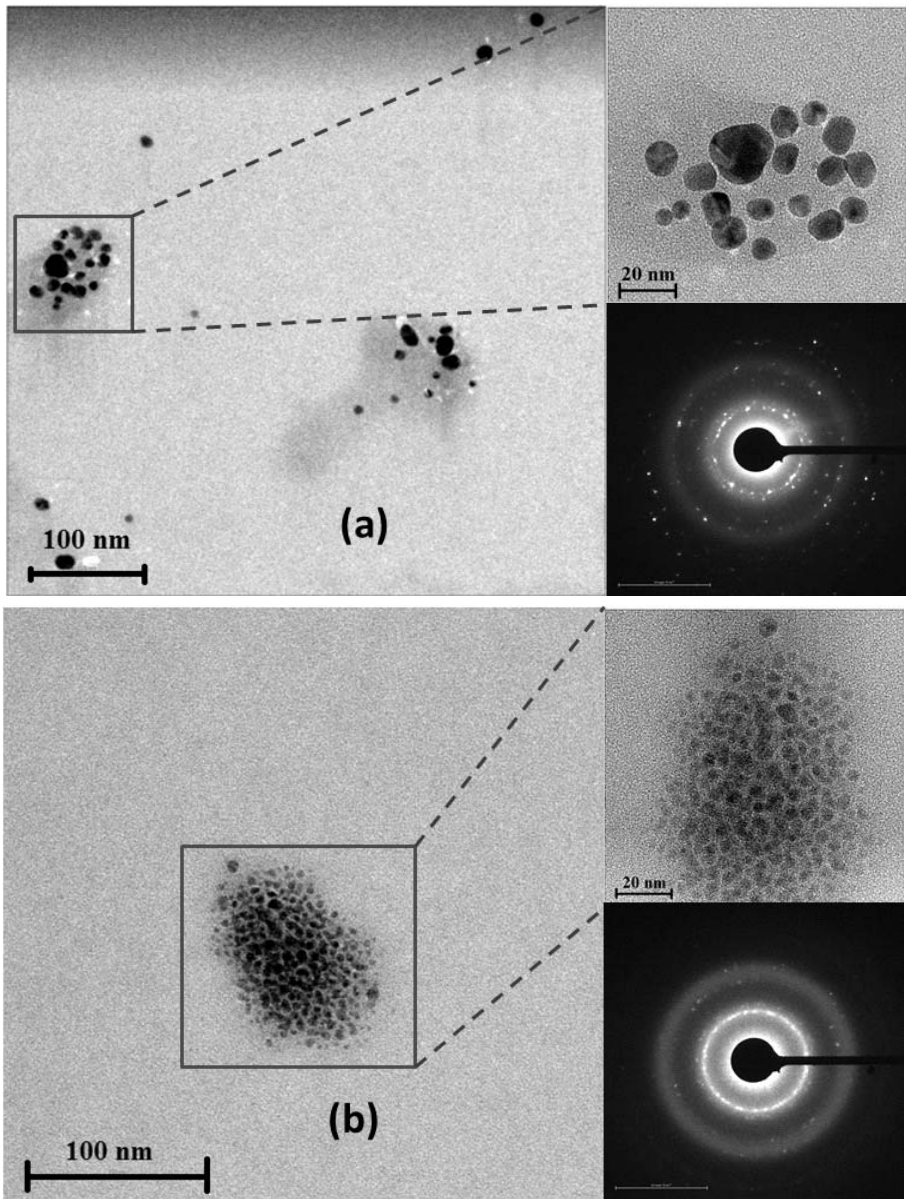

Fig. 4: Transmission electron microscopy (TEM) image of (a) Au/Ca-Alg and (b) Au/Ca-Fe-Alg nanocomposite extracted from the supernatant obtained during reduction of Au^{3+} loaded Ca-Alg and Ca-Fe-Alg films by glucose.

In order to study the interaction of GNPs with alginate, the vibrational spectra of Au/Ca-Fe-Alg films was compared with that of sodium alginate. FT-IR spectra of Au/Ca-Fe-Alg films and sodium alginate shown in Fig. 5 showed no appreciable difference in the vibrational bands of the two samples mentioned above, which indicates that incorporation of GNPs in the alginate matrix does not alter chemical structure of alginate[36]. The above observation further clarifies that the nature of interaction of alginate and GNPs is not chemical in nature. Thus, the GNPs loaded in the alginate films can be used for adsorption of other molecules for sensing applications.

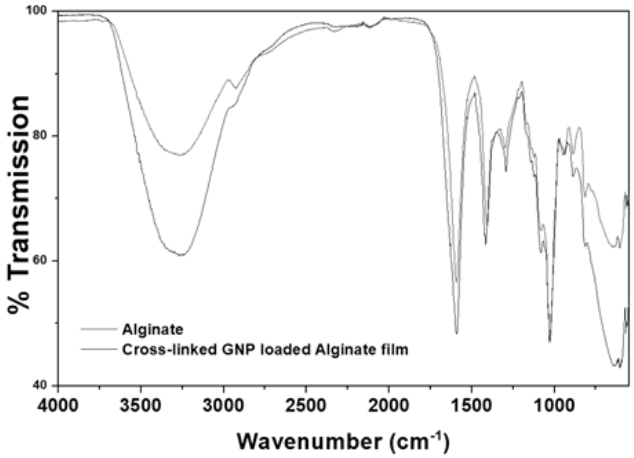

Fig. 5: FT-IR spectra of sodium alginate and GNP loaded cross-linked alginate films

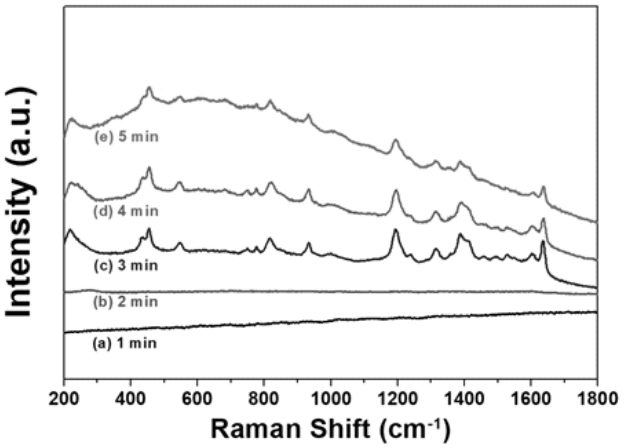

Fig. 6: SERS spectra of 10µl of 10^{-6} M SC drop casted on Ca-Fe-Alg films etched for (a) 1 min, (b) 2 min, (c) 3 min, (d) 4 min and (e) 5 min.

Au/Ca-Alg and Au/Ca-Fe-Alg films were used to record SERS spectra of CV. For the above purpose, 10µL of 10^{-5} M CV was drop casted on the films. None of the films showed SERS spectra. This may be due to loss of GNPs from the surface of the films during reduction of Au^{3+} adsorbed in the films by 0.05 M glucose for 3 minutes. As a result, GNPs are present beneath the layers of cross-linked alginate. The above observation was also encountered by Mele E. et al.,[29] where GNPs were not found on the surface of the anisotropic alginate biocomposites. In order to remove a layer of alginate, the films were immersed in 0.2 M HCl for a fixed interval of time. Au/Ca-Alg films showed no SERS signal whereas Au/Ca-Fe-Alg film showed SERS signal. The SERS signal was found to increase with increasing etching time up to 3 minutes and then decreased was observed as shown in Fig. 6. The above observation indicates that etching up to 3 minutes exposes GNPs present beneath the layer of cross-linked alginate (Fig. 6a-c). Further etching might have released GNPs from the pores of the alginate films, which had led to lowering of the SERS intensity as shown in Fig. 6 (d-e). Thus, acid-etched Au/Ca-Fe-Alg films were observed to be the best substrates for SERS.

Raman spectrum of CV is well studied in literature[37]. Raman spectra of CV in solid form as well as in aqueous solution, recorded at 632 nm excitation, is shown in fig. 7a and 7b, respectively. Raman spectrum of aqueous solution of 10^{-4} M CV (fig. 7b) shows vibrational bands at 441, 602, 670, 765, 803, 913, 1171, 1299, 1389 and 1614 cm^{-1} which correspond to 435, 605, 628, 767, 803, 915, 1170, 1299, 1390 and 1582 cm^{-1} peaks of CV as observed by Canamares et al.[37] Raman spectrum of solid CV (fig. 7a) also shows a good match with the reported values.[37]

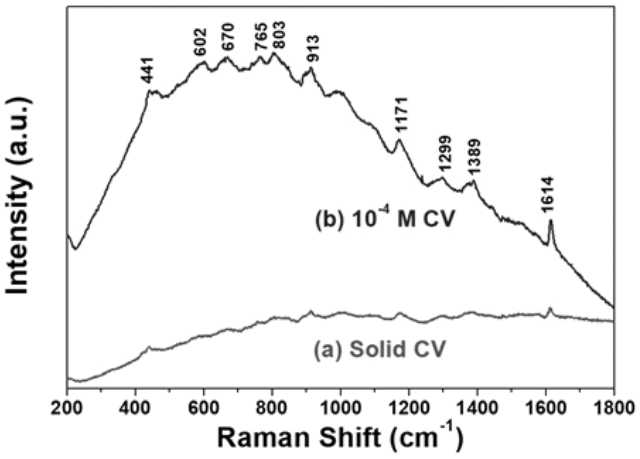

Fig. 7: Raman spectra of (a) solid CV and (b) 10^{-4} M CV at 632 nm excitation recorded for 1s and 10s respectively.

For SERS based detection of CV, acid-etched Au/Ca-Fe-Alg films were used as a substrate. 10 µL of varying concentrations of CV were added to each etched Au/Ca-Fe-Alg film prior to recording of SERS signal for 1 second under 632 nm excitation. In Fig. 8, the SERS signal of varying concentration of CV on Au/Ca-Fe-Alg films is shown. SERS spectrum of 10^{-6} M CV adsorbed on etched Au/Ca-Fe-Alg film excited at 632 nm showed vibrational bands corresponding to that of CV reported earlier.[37] Strong bands were observed at 455, 470, 1205, 1399 and 1651 cm^{-1} which correspond to C-C-C bending, C-N-C bending, C-C-C asymmetric stretching, ring methyl bending and benzene 8a mode[37], respectively. Other medium intensity bands were observed at 791, 831, 944 and 1618 cm^{-1} which corresponded to 10a, 17b, 17a and 8b modes of benzene[37], respectively. Weaker bands at 556, 591, 636, 697, 760, 791, 867, 966, 1252, 1369, 1420, 1473, 1510 and 1566 cm^{-1} were also observed.

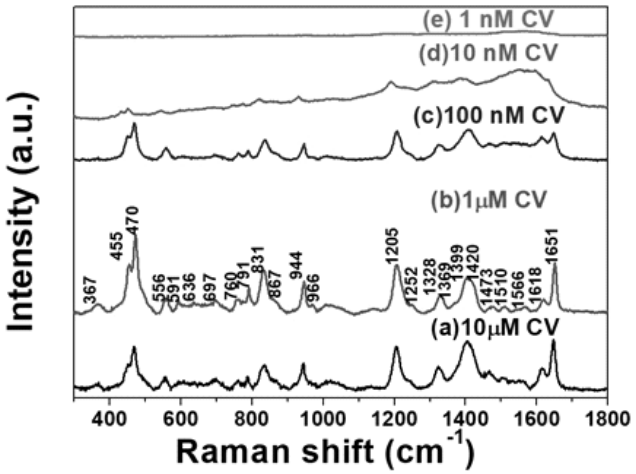

Fig. 8: SERS spectra of (a) 10µM, (b) 1 µM, (c) 100 nM, (d) 10 nM and 1 nM CV drop casted on acid-etched Au/Ca-Fe-Alg films excited at 632 nm.

In order to establish a method to determine concentration of CV detected by SERS using etched Au/Ca-Fe-Alg film, SERS intensity at 455, 470, 1205, 1399 and 1651 cm^{-1} which corresponds to strong peaks, were plotted with respect to varying concentration of CV as shown in Fig. 9. It can be seen that the SERS intensity of peaks at 455, 470, 1205 and 1651 cm^{-1} first increases and then decreases. The increase of SERS intensity may be attributed to monolayer adsorption of CV at a concentration of 10^{-6} M. In Fig. 8, similar observation was made. It was observed that upon lowering the concentration of CV from 10^{-5} to 10^{-6} M SERS, the intensity slightly increased (Fig. 8a-b). Upon further lowering the concentration of CV to 10^{-7} M and lower, SERS signal was found to decrease owing to sub-monolayer occupation of CV on the surface of GNPs (Fig. 8c-e).

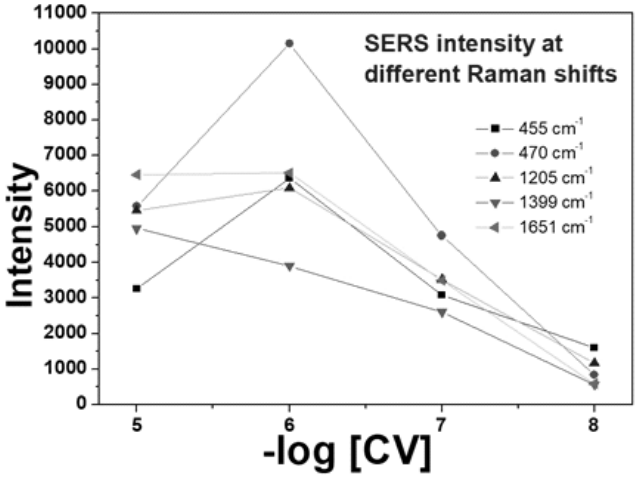

Fig. 9: SERS intensity of different concentrations of CV adsorbed on etched Au/Ca-Fe-Alg films at (a) 455, (b) 470, (c) 1205, (d) 1399 and 1651 cm^{-1}.

Since Fig. 9 does not show a linear trend, a suitable calibration curve cannot be obtained. Thus, this method can only qualitatively to detect CV in aqueous solution up to a concentration of 10^{-8} M or 10 nM.

Conclusions

In this work, *in-situ* synthesis of GNPs in cross-linked alginate matrix was successfully demonstrated. D-glucose was chosen as a suitable reducing agent due to its excellent compatibility with alginic acid, which is an oxidized polysaccharide. Rapid reduction of Au^{3+} by D-glucose and immobilization of GNPs in the matrix of Ca-Fe-Alg films requires a SERS substrate where GNPs are not dislodged from the polymeric matrix. Acid solubility of alginate further adds a facet to the features of

Ca-Fe-Alg films. GNPs dislodged from the surface of Au/Ca-Fe-Alg films during reduction process, rendered the surface of the film SERS inactive. Acid ething of the above film removed the inert matrix layer and exposed fresh GNPs for SERS detection of CV. Lowest concentration of CV that was detected by this method is 10 nM or ~4 ppb. CV is reported to be toxic as well as carcinogenic above a dose of 1 ppb.[38] Thus, acid-etched Au/Ca-Fe-Alg films synthesized in this work are inexpensive, easy-to-fabricate SERS substrate capable of detecting CV in aqueous medium within toxic concentration range. Detection of other dyes as well as pollutants is of future interest.

Acknowledgement

The authors are thankful Krishankant Singh, Radiation & Photochemistry Division, Bhabha Atomic Research Centre, Mumbai, India for support in FT-IR spectroscopy.

References

1. Pérez-Mayen L., Oliva J., Torres-Castro A. and De la Rosa E., 2015, *Nanoscale*, **7**, 10249.
2. Tian F., Bonnier F., Casey A., Shanahan A. E. and Byrne H. J., *Analytical Methods*, 2014, **6**, 9116.
3. Amendola V., Pilot R., Frasconi M., Maragò O. M. and Iatì M. A., 2017, *Journal of Physics: Condensed Matter*, **29**, 203002.
4. Ringe E., Langille M. R., Sohn K., Zhang J., Huang J., Mirkin C. A., Van Duyne R. P. and Marks L. D., 2012, *The Journal of Physical Chemistry Letters*, **3**, 1479.
5. Nehl C. L. and Hafner J. H., 2008, *Journal of Materials Chemistry*, **18**, 2415.
6. Derkachova A., Kolwas K. and Demchenko I., 2016, *Plasmonics*, **11**, 941.
7. Du L., Lei D. Y., Yuan G., Fang H., Zhang X., Wang Q., Tang D., Min C., Maier S. A. and Yuan X., 2013, *Scientific Reports*, **3**, 3064.
8. Ghosh S. K. and Pal T., 2007, *Chemical Reviews*, **107**, 4797.
9. Wang X., Li M., Meng L., Lin K., Feng J., Huang T., Yang Z. and Ren B., 2014, *ACS Nano*, **8**, 528.
10. Sanz J. M., Ortiz D., Alcaraz de la Osa R., Saiz J. M., González F., Brown A. S., Losurdo M., Everitt H. O. and Moreno F., 2013, *The Journal of Physical Chemistry C*, **117**, 19606.
11. Laurent G., Félidj N., Truong S. L., Aubard J., Lévi G., Krenn J. R., Hohenau A., Leitner A. and Aussenegg F. R., 2005, *Nano Letters*, **5**, 253.
12. Bruzas I., Lum W., Gorunmez Z. and Sagle L., 2018, *Analyst*, **143**, 3990.
13. Venkata P. G., Aslan M. M., Mengüç M. P. and Videen G., 2006, *Journal of Heat Transfer*, **129**, 60.
14. Maiti N., Chadha R., Das A. and Kapoor S., 2015, *Spectrochimica Acta Part A: Molecular and Biomolecular Spectroscopy*, **149**, 949.
15. Zhu T., Vasilev K., Kreiter M., Mittler S. and Knoll W., 2003, *Langmuir*, **19**, 9518.
16. Deraedt C., Salmon L., Gatard S., Ciganda R., Hernandez R., Ruiz J. and Astruc D., 2014, *Chemical Communications*, **50**, 14194.
17. Nuopponen M. and Tenhu H., 2007, *Langmuir*, **23**, 5352.
18. Tian Y., Liu H., Zhao G. and Tatsuma T., 2006, *The Journal of Physical Chemistry B*, **110**, 23478.
19. Kho K. W., Shen Z. X., Zeng H. C., Soo K. C. and Olivo M., 2005, *Analytical Chemistry*, **77**, 7462.
20. Palgrave R. G. and Parkin I. P., 2007, *Chemistry of Materials*, **19**, 4639.
21. Pilot R., 2018, *Journal of Raman Spectroscopy*, **49**, 954.

22. Wei W., Du Y., Zhang L., Yang Y. and Gao Y., 2018, *Journal of Materials Chemistry C*, **6**, 8793.

23. Lee M., Oh K., Choi H.-K., Lee S. G., Youn H. J., Lee H. L. and Jeong D. H., 2018, *ACS Sensors*, **3**, 151.

24. Dos Santos D.S., Goulet P. J. G., Pieczonka N. P. W., Oliveira O. N. and Aroca R. F., 2004, *Langmuir*, **20**, 10273.

25. Lee K.Y. and Mooney D.J., 2012, *Progress in Polymer Science*, **37**, 106.

26. Grant G.T., Morris E. R., Rees D. A., Smith P. J. C. and Thom D., 1973, *FEBS Letters*, **32**, 195.

27. Lee B.B., Ravindra P. and Chan E.S., 2013, *Chemical Engineering & Technology*, **36**, 1627.

28. Benavides S., Villalobos-Carvajal R. and Reyes J.E., 2012, *Journal of Food Engineering*, **110**, 232.

29. Mele E., Anyfantis G.C., Fragouli D., Ruffilli R. and Athanassiou A., 2014, *RSC Advances*, **4**, 20449.

30. Banerjee A., Nayak D. and Lahiri S., 2007, *Biochemical Engineering Journal*, **33**, 260.

31. Min J. H. and Hering J. G., 1998, *Water Research*, **32**, 1544.

32. Suhandy D. and Yulia M., 2017, *Int J Food Sci.*, **2017**, 6274178.

33. Brus J., Urbanova M., Czernek J., Pavelkova M., Kubova K., Vyslouzil J., Abbrent S., Konefal R., Horský J., Vetchy D., Vyslou•il J. and Kulich P., 2017, *Biomacromolecules*, **18**, 2478.

34. Phukan S., Bharali P., Das A. K. and Rashid M. H., 2016, *RSC Advances*, **6**, 49307.

35. Maher R.C., 2012, Raman Spectroscopy for Nanomaterials Characterization, Springer Berlin Heidelberg,p. 215-260.

36. Das A., Chadha R., Maiti N. and Kapoor S., 2015, *Materials Science and Engineering: C*, **55**, 34.

37. Cañamares M.V., Chenal C., Birke R.L. and Lombardi J.R., 2008, *The Journal of Physical Chemistry C*, **112**, 20295.

38. Mani S. and Bharagava R.N., 2016, Reviews of Environmental Contamination and Toxicology Volume 237, Springer International Publishing,p. 71-104.

RNI No. MAHENG/2017/74063
ISSN No. (Print) 2581-5911
ISI Impact Factor 0.883 (2018)

Efficiency of Magnetic-Impulse High Frequency Cavitation of Used Vegetable Oils to High Quality Biodiesel

A. Bissessur[1*], J.C. Ngila[2], P. Govender[2] and TAM Msagati[3]
[1]School of Chemistry and Physics, University of KwaZulu-Natal, Private Bag X54001, Durban, 4000 South Africa
University of Johannesburg, Department of Chemical Technology,
Corner Nina and Beit Street, P.O. Box 1701, Doornfonfein 2028, South Africa
[3]Nanotechnology and Water Sustainability Research Unit,
College of Science, Engineering and Technology
Papha Building, UNISA Science Campus, Florida, Johannesburg
Email*: bissessura@ukzn.ac.za

Abstract
This article evaluates the method of magnetic-impulse high frequency cavitation to effectively transesterify especially used vegetable feedstock oils to a high quality biofuel. The parallel transesterifications of crude palm and virgin sunflower oils were evaluated as direct comparators to justify the effectiveness and applicability of the method. The focal advantage of this method ensures a one-step conversion with minimal pre-treatment, with no modifications, additives and complex homogeneous/heterogeneous catalytic activities as pursued by many other others. Further, benefits are achieved through efficient reaction conditions without heating of the feedstock oil and improvement of the esterification reaction, low cost implications and high-end quality fatty acid methyl esters. Transesterification with over 95% biodiesel yields is achieved with relatively low power input of 15 kW, a 1:8-10 methanol to oil molar ratio, a 2.2 wt. % catalyst, reaction temperature of 50°C and a reaction time of 40 min. The grading of biodiesel from used vegetable feedstock oils and confirmation as a high quality one was evaluated through its high calorific value (39.50 MJ kg^{-1}), high viscosity (6.1-6.9 mm^2 s^{-1}), high flash point (190 - 192°C), low total glycerol (1.01 - 1.03%), low moisture (0.04 - 0.06%), acceptably low acid value (1.20 - 1.51%), negligible or trace sulfur and phosphorus levels which compared favourably to crude palm and virgin sunflower feedstock oil sources. Monitoring and confirmation of complete transesterifications was characterized through: FTIR-ATR; GC-MS; ^{1}H NMR; and ^{13}C NMR spectroscopy showing saturated and unsaturated ester signals.

Keywords: *Alkaline-catalyzed transesterification, Biodiesel, Magnetic-impulse high frequency cavitation, Gas chromatography-mass spectrometry, Vegetable oils*

Introduction

The increasing need for biofuels as a result of reducing oil reserves and heightening costs has, according to Fonseca et al[1] driven the production of biodiesel from renewable and sustainable sources. Barnwal and Sharma[2] have highlighted the twin crisis of fossil fuel depletion and extensive environmental hazards and the need to look at alternative sources of extraction of liquid fuels. However, according to Junne et al[3], although there is a move towards renewable sources the application of suitable biotechnological processes has restricted these

feedstock sources to be applied as a true alternative from an economic and sustainable standpoint. Hence, the investigation of the efficiency of magnetic-impulse high frequency cavitation as a method for producing a high quality biodiesel from used/waste vegetable oils has highlighted the availability of suitable biotechnological processes to sustain the use of renewable and sustainable feedstock sources. Biodiesel is regarded as environment-friendly and non-toxic; and microorganisms in soil or water can decompose biodegradable fuel. In addition to its high flash point, biodiesel has higher combustion efficiency than petro-diesel, produces less toxic air pollutants in that it has little or no sulfur, no lead, and no carbon monoxide and contains substantially reduced unburned hydrocarbons and low particulate matter as pointed out by Gustafson [4] and Yin et al[5]. Gustafson [4] and Yin et al[5] have also highlighted the point that biodiesel is also free of harmful aromatics components such as benzene, toluene and xylene which can be as high as 40 % in petrodiesel. The major disadvantage of biodiesel, however, is that it is more expensive to produce over its petro-diesel competitor when vegetable oils are used as starting material (Yin et al,[5]). It is thus necessary to find ways to minimize the production cost of biodiesel. The use of cheaper feedstock such as non-edible oils according to Yin et al[5] is one way; the other is to use a more efficient process to reduce the amount of catalyst used, energy consumption and reaction time.

Ramchandran et al [6] and Zayed et al[7] suggested that one way of reducing the cost of biodiesel is to employ low quality feedstock such as waste cooking oils, non-edible oils and soap stock (by-product of vegetable oil refinery), which are cheaply available and can be regarded as attractive feedstock for the production of biodiesel. A homogeneous basic catalyst is used in conventional biodiesel production, which is known to be a high conversion rate process. However, this process generates a large volume of water and the used catalyst cannot be recovered. Most previous and current transesterification of triglycerides involve reactions with alcohols (methanol, ethanol, propanol, butanol or amyl alcohol) that are catalysed by alkalis, acids or enzymes. Transesterification reactions being an equilibrium process according to Barnwal and Sharma[2] and Pal et al[8], requires excess of alcohol to drive the reaction toward ester production.

The most important variables according to Barnwal and Sharma[2] include:
a) reaction temperature, b) ratio of alcohol to vegetable oil, c) heterogeneous or homogeneous catalysts, d) mixing intensity and d) purity of source material. Most of the studies on transesterification of vegetable oils according to Fonseca et al[1] are based on batch processes. Problems associated with batch processes as compared to continuous processes according to Fonseca et al[1] are need for large reactor volumes, low efficiency due to start-up and shut-down nature, variability in quality of end products from batch to batch and high capital investment and labour costs. For these reasons, the biodiesel industry moved toward continuous processes.

Recent developments on continuous reactors according to Fonseca et al[1] include: replacement of classical stirring with ultrasound by Staravache et al[9]; a membrane reactor by Cao et al[10]; a liquid-liquid packed bed reactor investigated by Ataya et al[11]; a film reactor demonstrated by Narváez et al[12]; a gas-liquid reactor tested by Behzadhi et al[13] and microwave radiation experimented by Lertsathapornsuk et al[14]. Recent developments in sonochemistry reported by Veljkovic[15] has implemented the use of ultrasonic radiation as an efficient mixing tool in biodiesel production. The use of low frequency ultrasound in biodiesel production improved mass transfer between immiscible reactants via ultrasonic cavitation. Maniam et al[16] used ultrasound assisted in-situ transesterification of bio-waste from palm oil to produce renewable green fuel.

In their investigation, they achieved an 85% methyl ester conversion within 1-hour reaction time using experimental parameters of a MeOH to oil mass ratio of 6:1 and a catalyst content of 2.30 wt. % at a reaction temperature of 55°C. According to Atabania et al[17], biodiesel is currently not economical and feasible as an

alternate energy, and further research and development on the technical aspects are required. It is for these reasons that in this paper we investigate the production of high quality biodiesel using magnetic-impulse high-frequency cavitation and highlight its advantages.

Cavitation, according to Flint et al[18], Suslick[19] and Bang et al[20] is the process of formation in liquids of cavities (or voids) filled with gas, vapor or their mix (cavitation bubbles or caverns). Cavitation bubbles as described by Suslick[21] and Bang et al[20] emerge in the places, where the pressure in liquid goes below critical point (in a real liquid, the value of critical point is approximately equal to pressure of saturated vapor of the liquid at a given temperature). In liquids sonicated at high intensities as described by Suslick[22], sound waves propagate into the liquid media alternate in high-pressure and low-pressure cycles known as compression and rarefaction cycles whose rates depend on the wave frequency[22]. It is during the application of the low-pressure cycle that the high-intensity ultrasonic waves generate voids or small vacuum bubbles in the liquid medium.

The bubbles collapse at attainment of maximum volume and are no longer able to absorb energy; this occurs violently during a high-pressure cycle and termed cavitation[22].

Biodiesel production through hydrodynamic cavitation using *Citrillus colocyntis* (Thumba oil) by Pal et al[8] indicated that the process was simple, efficient, time saving, eco-friendly and industrially viable process. Thanh et al[23] transesterified canola oil with methanol using a potassium hydroxide base catalyst via an ultrasound-assisted (UA) process. The ultrasonic irradiation was set at a low frequency of (20 kHz) with an input power of 1 kW. The yield of FAME was more than 99% using a methanol to oil ratio of 5:1, a 0.7 wt. % KOH and a reaction time of 50 min.

The process of cavitation in essence can be implemented via two major processes:

a) Acoustic cavitation is an effective resource of concentration of low-density sound wave energy into high density of energy, related to pulsations and collapse of cavitation bubbles[19,21-23].

b) Magnetic-impulse high-frequency cavitation processing proceeds within the reactor at molecular level. Magnetic-impulse is an electromagnetic *pulse* consisting of short burst of electromagnetic energy of short duration hence spreading over a range of frequencies. Such pulses are characterized by the type of energy viz. radiated, electric, magnetic or conducted energies.

All components are exposed to impulses of magnetic-direction cavitation. Magnetic-impulse high-frequency cavitation differs from usual cavitation effect with influence of magnetic field on microplasma formations, emerging by active cavitation[24].

A process known as micro-explosions induces splitting of the fatty acid molecules, which decreases the viscosity, increases the cetane number and energetic parameters of the biofuel coupled with acceleration and improvement in the quality of the transesterification reaction. Furthermore, using this process, the transesterification reaction proceeds at room temperature circumventing the need to heat up the feedstock oil [24]. Additionally, feedstock oils of varying quality can be applied as source product coupled with the fact that cavitation modules do not require the preliminary preparation of feedstock oil.

This process works successfully with both crude and refined oil. A variety of oils can be used to produce biodiesel – sunflower oil, rapeseed oil, linseed oil, palm oil, mustard oil etc. with almost any acid number as well as waste vegetable oil from restaurants and bakeries – and thus no need to re-adjust the reactor equipment for all kinds of oil [24]. While traditional methods of biodiesel production are based on heating of oil up to 67-70°C, the method of magnetic-impulse high-frequency cavitation has low energy usage. It requires significant electric power inputs; besides the recovery of methanol (the necessary requirement for the reaction proceeding in traditional technologies), additional

re-esterification as well as vacuum dehydration results in great electric power consumption. By cavitation, there is no need for processing in all the above-mentioned stages and the result is 5-7 times higher in electric power saving [24]. Another advantage of magnetic-impulse cavitation technology lies in its ability to function as a one-pass reactor conversion process where there is no need for re-esterification reaction, like in old "tank" technologies wherein reagents are added and mixed physically. One of the serious problems of "tank" technologies is the requirement to add an excess of methanol in the reactor that further necessitates recuperation. It requires the installation of additional equipment and electric power input. In cavitation technology, the quantity of alcohol used by reaction meets the chemical formula, i.e. the minimal amount.

The expensive and dangerous equipment for methanol recuperation is excluded which improves the aspect of explosion safety and the ecological situation [23]. According to Veljkovic, [15], recent developments in sonochemistry has implemented the use of ultrasonic radiation as an efficient mixing tool in biodiesel production catalyzed by acid, base or enzyme catalysts. The use of low frequency ultrasound in biodiesel production improved mass transfer between immiscible reactants via ultrasonic cavitation.

The objectives of this research technology are development, optimizing and implementation of magnetic-impulse high-frequency cavitation via a one-step batch process using a homogeneous alkali catalysed methanol transesterification reaction for the production of biodiesel from various feedstock sources including crude palm oil (*CPO*), virgin vegetable oil (*VSO*) and waste vegetable oil (*UVO*).

Materials and Methods

Raw Feedstock

Crude palm oil (*CPO*), virgin sunflower oil (*VSO*) and used vegetable oil (*UVO*) served as the three main feedstock sources of oil used in the transesterification reactions. Samples analyses as shown in Table 1 comprised BD 1 – 5 = (CPO), BD 6 = (VSO), BD 7-8 = (UVO). CPO and VSO were purchased from local suppliers in South Africa while UVO were sourced from local restaurants and waste oil suppliers in South Africa.

Reagents

All reagents used for the transesterification and purification process were of biodiesel standard: B100 soy-based NIST 2772 biodiesel standard (Sigma-Aldrich), methanol 99.9% (high purity grade, Merck), potassium hydroxide 85% pellets (GR grade from Merck), hydrochloric acid 37% (GR grade for analysis, Merck). Millipore water and spectroscopic grade solvents were used in all analytical determinations. All feedstock samples were filtered.

Methodology for Biodiesel Production

Transesterification by High-Frequency Magnetic-Impulse (HF-MI) Cavitation

The induction of magnetic-impulse high-frequency cavitation by the PULSAR-ST 215-B batch transesterification reactor (Figure 1, OPERATION MANUAL of the device PULSAR-ST 215-B) using low alcohol and reagents in a one-step reactor conversion has been found to produce high quality biodiesel using various kinds of feedstock.

A Typical Transesterification Batch Process

Production of a typical 20 L (~18 kg) batch of biodiesel from used vegetable oil, crude palm and virgin sunflowers feedstock oils: The feedstock oil is filtered using 13 μm filter and added to the mixing vessel of the batch reactor. A 2.30 L aliquot of methanol that is 10 % by mass of the feedstock oil is added to the mix vessel, and the mix-circulating pump is immediately activated. An aliquot mass of 400 grams of potassium hydroxide was dissolved in 500 mL of methanol and immediately added to the mixing vessel. The reactants were allowed to mix for approximately 12 min. The reactor was subsequently activated and the oil-catalyst mixture was

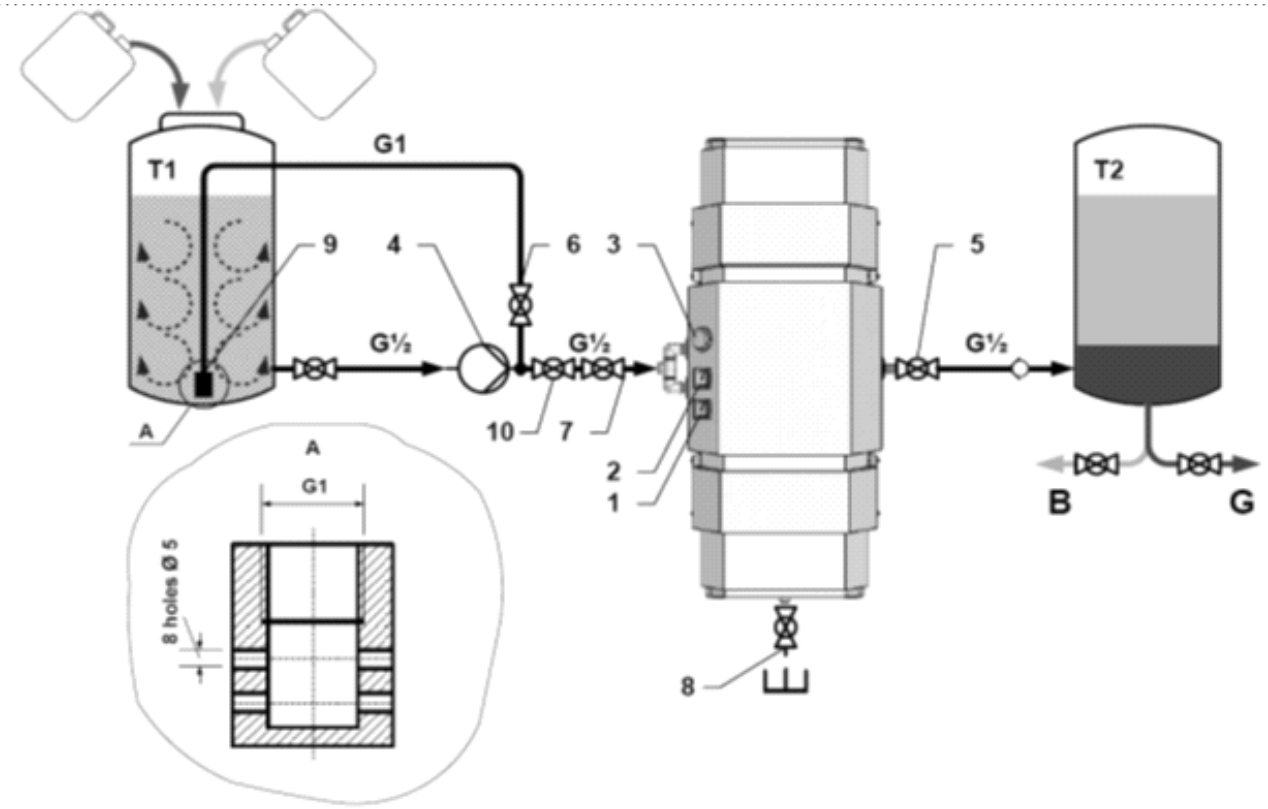

Fig 1: Diagram of a batch biodiesel PULSAR-ST 215-B mixing machine, capacity 500 L [24]. The numbers represent 1. Temperature sensor; 2. Pressure sensor; 3. Temperature relay; 5. Mixture consumption control valve; 6. Reverse mixture control valve; 7. Pressure control valve; 8. Drainage; 9. Reverse supply pipeline muzzle; 10. Valve; T1 – preliminary mixing reservoir; T2-separating reservoir; B-Biodiesel rundown pipeline; G – glycerol rundown pipeline.

circulated through the reactor until temperature reached above 50°C. Upon attaining a set-point temperature, the transesterified product, glycerol and water mixture were sent to a separation tank and the final temperature of the mixture reached approx. 65°C. The biodiesel separated from the glycerol within a duration of 40 min containing approximately 16% glycerol content (based upon source of the feedstock oil).

Separation and Purification of Biodiesel

The mixture was allowed enough setting time whereby the heavier phase residual methanol and glycerol were separated from produced biodiesel and unreacted oil. Separation was complete in 40 minutes. After draining of the bottom layer, the oil layer was washed three times to remove remaining catalyst and glycerol.

For the first wash, a small volume aliquot of dilute HCl (~0.5 N) solution was added to neutralize the alkali catalyst. Washing continued until the drainage pH matched that of distilled water. The product was heated to 105°C for about 15 min to remove any residual water.

Chemical and Physical Analysis of Biodiesel

Total Acid Number (TAN)/Free Fatty Acid (FFA) Value

The D 664 Standard Test Method for Acid Number of Petroleum Products by potentiometric titration [24] was used to calculate the FFA in biodiesel. The acid number represents the total amount of acidic components

present, which is an indication of the amount of free fatty acids (FFA) found in biodiesel. The acid value was determined by using ASTM D 974 [26]. The ASTM biodiesel standard D 6751 [26] specifies a maximum limit of acid value for biodiesel to be 0.50 - 0.80 mg KOH/g).

Moisture Content of Biodiesel

The content of water according to EN 14214 and ASTM D 6751 standards was limited to 0.05% (w/w) [27]. The moisture content of biodiesel was carried out by the Karl Fischer method on a Metrohm® 901 Titrando instrument.

Higher Heating Value (HHV) or Calorific Value (CV) [28]

The DRYCAL Modular Calorimeter and DRYCAL 2010 Energy Instrumentation Microsoft Windows Build software measured the higher heating value (HHV) or calorific value of biodiesel. The equipment was calibrated with benzoic acid according to ASTM method D-240-02 [29]. Subsequent to calibration, biodiesel samples were weighed and inserted into a crucible, a "bomb" was set-up and the system was pressurised to 250 kPa and higher heating or calorific values were recorded in MJ/kg.

Kinematic Viscosity of Biodiesel Samples

The standard method ASTM D 445 was used for measuring the kinematic viscosity and subsequent calculation of the dynamic viscosity [30]. Kinematic Viscosity is the ratio of absolute or dynamic viscosity to density - a quantity in which the force is external and independent of the mass of the fluid. Kinematic viscosity can be obtained by dividing the dynamic viscosity of a fluid by its density as shown in Equation 1 below:

where ν = kinematic viscosity, μ = absolute or dynamic viscosity, ρ = density. The SI unit is expressed in $m^2\ s^{-1}$ [27, 29]. The prescribed kinematic viscosity at 40°C of a high quality biodiesel ranges between 1.9 and 6.0 $mm^2\ s^{-1}$ [28,30]. Viscometer calibration was carried out using the certificate of calibration issued by Poulten Selfe and Lee LTD calibration laboratory, (February 2005) for N10 and S20 standard viscosity oils [31]. The viscometer constant was calculated at 40°C. The appropriate oil standard was selected according to the viscometer bore size. The viscometer was cleaned with acetone and dried before use. The viscometer was placed in the constant temperature waterbath at 40°C ± 1°C and allowed to equilibrate for at least 10 minutes. Biodiesel samples were filtered through a 0.45 mm filter, drawn up the viscometer and replicate efflux times were measured to within 0.1 s of each other and the viscosity measured according to Equation 2.

Viscosity in centipoise (cP) = Time in seconds × viscometer constant **(2)**

Flash Point of Biodiesel Samples [32]

Flash point is defined as the minimum temperature at which the vapor pressure of a particular hydrocarbon (biodiesel) is adequate for the generation of the vapor needed to spontaneously ignite the biodiesel in the presence of oxygen (air) using a flame or spark as an external heat source [30]. The flash point of biodiesel was measured using the Pensky-Martens closed-cup tester of fuel oils according to ASTM. [30]

Inorganic Analysis of Biodiesel by Inductively Coupled Plasma- Optical Emission Spectroscopy (ICP-OES)

The sulfur content was analysed according to the methodology outlined by ASTM D 6751 [6]. The calcium and magnesium was analysed according to the methodology outlined by ASTM D 6751 [6]. The level of phosphorus was determined according to ASTM method D 6751. The sulfur content was analysed according to the methodology outlined by ASTM D6751. The calcium and magnesium was analysed according to the methodology outlined by ASTM D6751 [6]. The level of phosphorus was determined according to ASTM method D6751 [6]. The determination of sodium and potassium was carried out in accordance to ASTM D 6751 using a flame photometric method.

Sample Preparation and Analysis for Metal Ions by ICP-OES

An aliquot of biodiesel was digested with aqua regia, filtered and diluted to volume with millipore water. Samples were filtered with a 0.45 μm filter directly into ICP vials and analysed using a radial plasma of the Perkin Elmer Optical Emission Spectrometer Optima 5300 DV against a multi-element Ca, Mg, Al, Zn, S, P standards.

Sample Preparation and Analysis for Sodium and Potassium by Flame Photometry

A volume aliquot of biodiesel was digested with aqua regia and made up to volume with millipore water. The solution was filtered using 0.45*m*.m filter and analysed using Jenway Flame Photometer.

Qualitative Analysis of Biodiesel Samples by Gas Chromatography-Mass Spectrometry (GC-MS)

All GC-MS analyses of biodiesel samples was carried out on the Agilent GC System 6890 Series and all mass spectroscopic data was recorded using the Agilent, 5973 Network, Mass Selective Detector. The analysis of biodiesel was performed by the 6890 GC method with flame ionization detection (FID). Details of instrument conditions and settings for a full scan is shown in Table 2 The GC analysis of biodiesel was carried out in accordance with EN 14103 [33]. The retentions times and mass spectra of the FAMEs were recorded and analysed using the NIST spectral library.

GC-MS Analysis of Biodiesel

All samples were analysed using the Agilent GC 6890 Series GC and 5973 MS System**.** Instrument settings included initial oven temperatures of 50°C and ramping to 260°C at a ramp rate of 10°C min^{-1} using capillary Zebron ZB-5 MS column of length 30 m, diameter 250 mm, film thickness 0.25 mm, flow rate of 1.0 mL min^{-1}, inlet pressure of 52 kPa, mass spectral detection temperature of 280°C, mass spectral source temperature of 230°C and quadrupole temperature of 150°C.

Spectroscopic Analysis of Biodiesel Samples

Spectroscopic Analysis of Biodiesel by Fourier Transform Infra Red-Attenuated Total Reflectance (ATR-FTIR)

All transesterification reactions were diagnostically monitored by ATR-FTIR particularly functional groups of FAMEs were characterised. The ATR-FTIR characterisations of the feedstock oils and transesterified biodiesel samples were analysed using the Perkin Elmer 100 Fourier Transform Infrared Spectrophotometer with a Universal sample diamond ATR accessory attachment. An average of 32 replicate sample scans preceded by a background scan using air as a blank. All samples were scanned at ~23±1°C.

Analysis of BD using Proton Nuclear Magnetic Spectroscopy (^{1}H-NMR) and Carbon 13 Nuclear Magnetic Spectroscopy (^{13}C-NMR)

Corroboration of transesterification and positive identification of the synthesized FAMEs was elucidated using ^{1}H and ^{13}C-NMR spectroscopic analysis. NMR spectroscopic analysis of feedstock, synthesized and purified biodiesel samples were recorded on Bruker AVANCE III 400 MHz NMR spectrometer at room temperature (20-25°C). Biodiesel and feedstock oil samples was dissolved in deuterated chloroform ($CDCl_3$) and all spectra were resolved using the Topspin® software.

Results and Discussion

The technology of magnetic-impulse high frequency cavitation was successful and highly efficient in producing good quality and appreciable yields of biodiesels (FAMEs) from used vegetable feedstock oil sources with minimal (mainly filtering) pretreatment. The short burst of electromagnetic energy of short duration arising out of magnetic impulses spreading over a range of frequencies coupled with high frequency (15 kWh) magnetic-direction cavitation produced micro-explosions inducing splitting of the fatty acid molecules, during the transesterification reaction. It is this reaction mechanism, otherwise not produced by other acid/based catalyzed transesterifications, which makes it unique in

efficiently transesterifying the waste vegetable feedstock oil into useful biodiesel in comparison to crude palm and virgin sunflower.

In addition to excellent yields, the moisture content (Table 1) is seen to be within acceptable ASTM D 6751 limits, which is one of the crucial parameters in attaining a high quality biofuel. The technology has been useful in that it has shown to be receptive to a highly difficult matrix in the form of crude and used vegetable oil sources, which in most cases require intense, sensitive and successive step-wise pre-treatments prior to biofuel synthesis. The discussion that ensues corroborates the claim that FAMEs produced from such *'troublesome'* feedstock sources are a high quality fuel which satisfies the criteria as specified for both ASTM (D6751) and CEN (EN14214) so as to be considered as a commercial biodiesel commodity.

Yield, Free Fatty Acid, Glycerol and Moisture Content of Synthesised Biodiesels

Bautista et al [34] have highlighted the use of potassium hydroxide-catalysed methanolysis of waste cooking oil (EN 14214) which produce esters which are 96.5% by weight or more.

In this study, close such yields have been attained as shown in Table 1, thus endorsing this criterion. The technique of MI-HF transesterification is an effective and efficient method in delivering a high quality biodiesel at advantageously favourable yields. An added advantage of the transesterification technique is highlighted by the low glycerol content (Table 1) obtained for all FAMEs from various sources. The acid number represents the total amount of acidic components present, which is an indication of the amount of free fatty acids (FFA) which is found in biodiesel.

The FFA is directly correlated to the corrosiveness and stability of biodiesel over a prolonged time whereby a low FFA value infers a high quality biofuel. The measurement of the total acid number of FFA or acid formed is carried out by a non-aqueous potentiometric acid-base titration. While the acid values shown in Table 1 in this study slightly exceeds specified values and are technically not within specifications according to ASTM D 6751, other commercial biodiesels according to Salamantinia et al [26] have generated higher acid values to the extent of 2.76 mg KOH/g. A higher acid value of biodiesel is a direct consequence of the type of feedstock used (containing a high FFA content) which impacts on the quality of the transesterified methyl esters. While the acid values in this study are not significantly high, it is imperative to keep these values to the prescribed minimum so that it does not pose a potential threat by causing system deposits and corrosion.

The acid values can be controlled to a desired minimum by ensuring process control during the transesterification. The free and total glycerol content of the biodiesel (Table 1) show opposing value trends in that the free glycerol are within specification limits in most cases with the exception of the used vegetable oil which is expected based on the formation of heat degraded products and oxidation from prior use.

However, it is marginally higher than the prescribed specified limits that makes it acceptable as a borderline value. On the other hand the total glycerol values exceeds the maximum permissible amount which makes it undesirable in that it could lead to carbon residue during combustion within the engine, thus interfering with the aspiration of the biodiesel into the combustion chamber. Lowering the total glycerol content is a totally washing dependent stage and it is imperative that this stage is carefully monitored or repeated to ensure the attainment of low glycerol levels.

Physical Characteristics of Synthesised Biodiesels

The viscosity, flashpoint and calorific values of biodiesel shown in Table 2 respectively, all conform to the limits specified by ASTM 6751 and EN 14214. The biodiesel produced can thus be qualified as a high quality biodiesel thus validating the HF-MI transesterification batch process. Maintaining the correct viscosity of biodiesel (prescribed kinematic viscosity at 40°C of a high quality biodiesel ranges between 1.9 and 6.0 $mm^2 s^{-1}$) is of

Table 1: Yield, FFA, Glycerol and Moisture Content of Biodiesel.

Biodiesel Sample	Yield (%)	Free Glycerol (%)	Total Glycerol (%)	Moisture (%)	Acid value mg KOH/g oil
BD 1	98.5	0.03	1.02	0.03	0.80
BD 2	97.5	0.03	1.22	0.01	1.18
BD 3	95.1	0.02	2.42	0.02	1.33
BD 4	95.5	0.03	1.32	0.03	1.34
BD 5	95.8	0.03	1.03	0.01	1.17
BD 6	95.3	0.03	1.20	0.02	0.80
BD 7	95.5	0.06	1.01	0.06	1.20
BD 8	95.1	0.07	1.03	0.04	1.51

% Max: Yields (>96, EN 14214); Free glycerol = 0.02; Total glycerol = 0.25; water = 0.05; Acid value = 0.5 [36]

paramount importance thus ensuring easy flow to the combustion chamber and complete atomization in the combustion chamber. A high viscosity may result in incomplete biodiesel combustion, dripping from the fuel delivery outlet-nozzle thus causing hot spots on the head of the piston that may eventually cause damage. In addition, the non-combusted biodiesel is at risk mixing with the lubricating oil. Finally, excessive exhaust smoke fumes would result out of un-combusted biodiesel. The flashpoint of biodiesel is dependent upon the feedstock source from which it is derived, hence variations are expected. According to ASTM 6751, the flash point of B100 biodiesel must exceed 130°C. The flash points of CPO BD1-5 ranges between 82 – 84°C, VSO BD 6 has a lower flash point of 174°C and that of UVO BD 7-8 ranges between 190 – 192°C. This clearly verifies changes in flash points as due to genetic variation of feedstock oil sources. Biodiesel produced from used vegetable oils has the highest flash point, which serves as an advantageous physical characteristic in that it circumvents premature engine ignition thus grossly reducing smoke-rich exhausts, and enhancing the safety aspects of biodiesel as a biofuel.

The measured calorific values or higher heating values (HHV) (approx. 39±0.1 MJ kg^{-1} in Table 2) of the biodiesel samples produced very similar values for all feedstock sources used. These values are much higher than the minimum prescribed value of 35 MJ kg^{-1} in EN 14213 while calorific values is not prescribed by both ASTM D 6751 and EN 14214 [35]. The favourable calorific values is one of the key and crucial parameters that makes biodiesel an attractive and preferred fuel over petroleum based fuels [35]. The MI-HF cavitation transesterification process can be identified as a dominant factor in producing biodiesel with such a favourable parameter.

Table 2: Physical Characterisation of Biodiesel.

Biodiesel Samples	Feedstock Source	Viscosity* ($mm^2 s^{-1}$)	Flashpoint* (°C)	Calorific Value* MJ kg^{-1}
BD 1	*CPO*	4.4	182	39.54
BD 2	*CPO*	5.7	186	39.71
BD 3	*CPO*	4.8	184	39.42
BD 4	*CPO*	5.4	184	39.60
BD 5	*CPO*	4.2	188	39.38
BD 6	*VSO*	3.6	174	39.50
BD 7	*UVO*	6.9	192	39.50
BD 8	*UVO*	6.1	190	39.50

*Average of triplicate analysis

Max Limits: Viscosity (@ 40°C), $mm^2 s^{-1}$ (1.0-6.0, ASTM D6751; 3.5-5.0, EN14214); Flashpoint (°C) (>130, ASTM; >120, EN14214)

The variation in sulfur content, ranging from no sulfur present to approx. 10 ppm, shown in Table 3 confirms its dependence on the feedstock source. The source of sulfur in BD 1 and 2, although not alarmingly high, could be linked to feedstock source or external contamination. The extremely low levels of sulfur in biodiesel (< 10 ppm) [36] coupled with the lubricating ability of sulfur for fuel pump and fuel injector activities makes it a suitable fuel over its diesel and petrol competitors. These low sulfur levels are important in that the sulfur oxide content emitted from exhausts during engine combustion is kept to a minimum. It is therefore imperative that the transesterification process generates a final product within acceptable sulfur levels (10 ppm in most countries). In this case, the MI-HF transesterification process has effectively achieved this. The sulfated ash content of biodiesel, which is a measure of the levels of trace metals such as sodium, potassium, magnesium, calcium, sodium and phosphorus shown in Table 3 are within acceptable limits with the exception of BD1 that shows anomalous levels of aluminium and phosphorus**.** This is possibly linked to the source of the feedstock or perhaps external contamination during transesterification. The presence of magnesium and calcium in the form of soluble metallic soaps or abrasive solids, when present in high quantities, impact negatively on the engine compartment because of wearing of parts, blockage of filters and deposition of residue. An accumulation of Ca and Mg in exhaust pipes may lead to increased build-up of backpressure, which may cause malfunctioning of exhausts, which prescribes a phosphorus content that should not exceed 10 ppm (w/w) due its negative impact on the catalytic converters of automobiles whereby catalyst is coated with phosphorus thus rendering it ineffective in treating exhaust components. Biodiesel is characteristically organic in nature and inorganic components are inherently present at extremely low levels. The levels of potassium and sodium are of particular interest in that they are used as catalysts during transesterification and hence are introduced into the system. Thus, low levels of sodium and potassium are essential markers in highlighting effective washing of the biodiesel.

In this study, almost negligible amounts of Na and K were found to persist, hence indicating effective washing at the final stage. The negative effect of the inorganic ash content mainly contributes to filter blocking, wear on the pistons, fuel pump, injectors and rings in the engine compartment.

Table 3: Inorganic Analysis of Biodiesel.

Biodiesel Samples	Inorganic ions (ppm)						
	Na	K	Mg	Ca	Al	S	P
BD 1	ND	1.0	ND	9.0	23.6	10.1	ND
BD 2	ND	0.9	ND	11.4	ND	5.7	ND
BD 3	ND	0.02	ND	5.6	ND	ND	ND
BD 4	ND	ND	ND	9.5	ND	ND	ND
BD 5	ND	0.06	ND	6.9	ND	ND	ND
BD 6	ND	ND	ND	8.9	ND	ND	ND
BD 7	ND	0.1	ND	8.5	ND	ND	ND
BD 8	ND	ND	ND	8.3	ND	ND	ND

Average of triplicate analysis; ND = Not detected
Max Limits: Na, K, Ca, Mg (<5.0 ppm, EN 14214); S (<10 mg/kg, EN 14214; P(<10 mg/kg, EN 14214)

A phosphorus content that should not exceed 10 ppm (w/w) due its negative impact on the catalytic converters of automobiles whereby catalyst is coated with phosphorus thus rendering it ineffective in treating exhaust components. The presence and accumulation of sodium and potassium in biodiesel is due mainly to their presence in the catalysts used alkaline transesterification reactions.

Sodium and potassium may function as abrasive solids or soluble metallic soaps if allowed to accumulate in biodiesel over a period and therefore may show similar effects as that shown by calcium and magnesium.

The South African Standard for biodiesel, SANS 1935 [36], is a set of chemical and physical tests and values that commercially synthesized biodiesel must conform to and be acceptable for engine combustion. The test defined by SANS 1935 conforms to international tests, that warrants complete transesterification reaction, complete removal of free and bound glycerol, removal of the catalyst and methanol used in the transesterification reaction, no presence of free fatty acids (FFA's) and removal of water. The transesterification process and biodiesel produced in this study have conformed to conditions prescribed by SANS, thus endorsing quality control and quality assurance.

ATR-FTIR analysis of synthesized Biodiesels

The ATR-FTIR spectra shown in Figure 2 of the synthesised FAMEs obtained from different feedstock sources show similar stretching frequencies with comparable intensities in all cases. This is indicative of a consistent MI-HF transesterification reaction process. The main band assignments verifies the production of FAMEs as the main products and differentiates it from the refined oil starting material. The principal spectral region that permits for positive and characteristic identification of FAMEs lies within a range of 1500 cm^{-1} - 900 cm^{-1}, commonly called the "fingerprint" region.

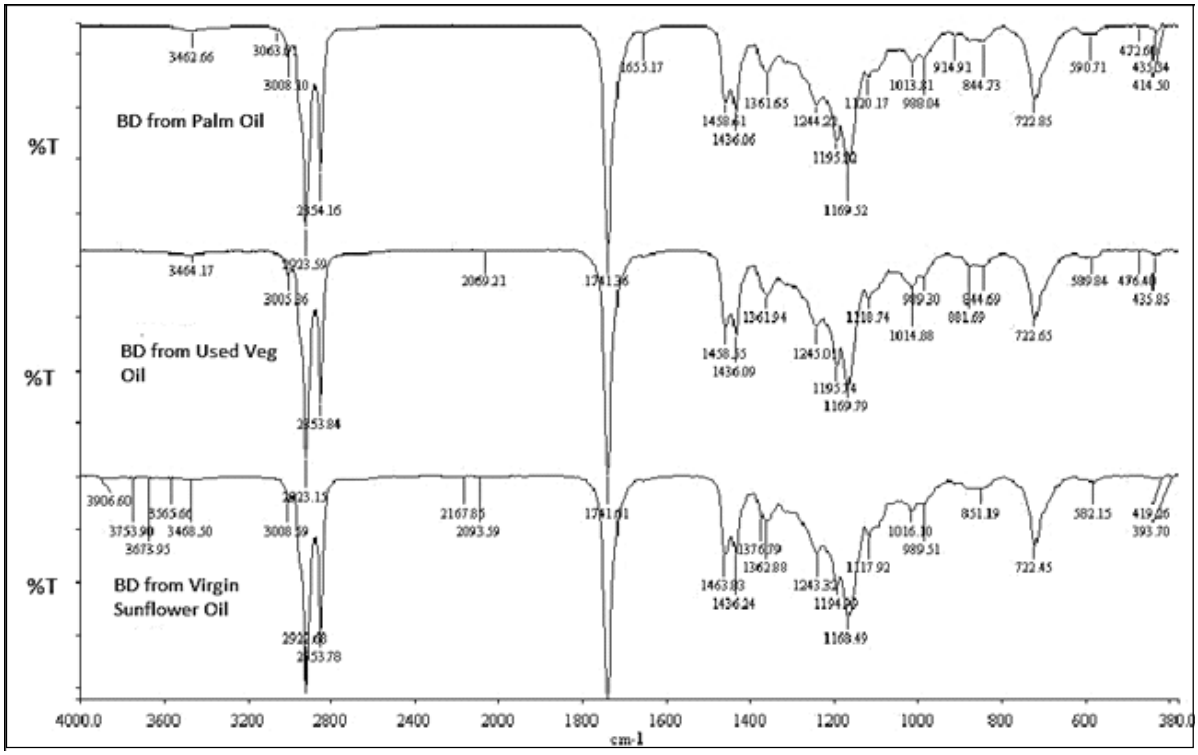

Fig 2: ATR-FTIR spectra of FAMEs synthesised from CPO, UVO and VSO oil feedstock

The principal stretching vibrations attributed to assigned functionalities in the FAMEs are identified as

a) -CH_2 rocking observed at 722 cm^{-1} not exclusively in FAMEs but also in the feedstock oils.
b) C-O stretch at observed 168 – 1169 cm^{-1}
c) -O-CH_3 stretching vibration represented by the peak at 1196 cm^{-1}, is typical of biodiesel.
d) -C=O observed peaks 1741 cm^{-1} is typical of esters, in FAME
e) -(C=O)-O-CH_3 peak at 1436 cm^{-1} is the most characteristic stretching vibration indicative of FAMEs
f) -CH_2 peaks observed at 2853 – 2854 cm^{-1}, also observed in the feedstock oils.
g) -CH_2 peaks observed at 2922 – 2923 cm^{-1}, also observed in the feedstock oils.

The observed band assignments of stretching vibrations for functional groups identified in can be attributed to a –CH_2 rocking at 722 cm^{-1}, C-O stretch at 1168-1169 cm^{-1}, -O-CH_3 stretch at 1194-1195, (C=O)-O-CH_3 stretch at 1436 cm^{-1}, C=O stretch (indicative of esters) at 1741, -C-CH_3 stretch 2853-2854 cm^{-1} and a -CH_2 stretch at 2922-2923 cm^{-1}. The appearance of vibrational stretch at 1435-1436 cm^{-1} in Figure 2 authenticates the transesterification reaction, which is highly indicative of the methyl ester group in FAMEs. Another transesterification monitoring control signal using ATR-FTIR lies in the ester control stretching frequency signal area of approx. 1200 cm^{-1}. The appearance of two characteristic signals at 1168-1169 cm^{-1} and 1194 – 1195 cm^{-1} in FAMEs (Figure 2) is due to separation of a strong, broad signal at 1159 cm^{-1} typically shown in the ATR-FTIR spectrum of the feedstock oils thus confirming attainment of transesterification reaction. The highly noticeable absence of alcohol –OH groups in the spectrum at 3250–3420 cm^{-1} is indicative of complete removal of any unreacted alcohol and highlighting effective washing of the FAMEs.

Gas Chromatography – Mass Spectroscopy (GC-MS) of FAMES

The GC-MS analysis of FAMEs from CPO, VSO and UVO was carried out primarily to confirm the absence of mon-, di- and triglycerides thus ensuring complete conversion during the MI-HF cavitation transesterification. The total ion chromatograms (TIC) of FAMEs derived from CPO, VSO and UVO obtained from GC-MS analysis, showed the separation of 4 major components (Figure 3) at retention times of approximately 18 min, 2 components at 19 min and the third at 20 min (Table 4) in all cases (i.e. BD 1 – 8). ^{1}H and ^{13}C NMR spectroscopy corroborates this claim as shown in the spectra (Figures 6 - 8). The mass spectra of all four components at the specified retention times in Table 4, were positively identified as FAMEs using the NIST 89 library match software referencing system at a similarity index (SI) above 80% against a B100 soy-based biodiesel standard.

The two major FAME components at retention times 18 min and 19.8 min (Figure 3) obtained from the CPO feedstock oil was dominated by the synthesis of saturated and unsaturated FAMES, hexadecanoic acid, 9-Octadecenoic acid, 7-Octadecenoic acid, 8-Octadecenoic acid and 9,12-Octadecadienoic acid methyl esters (Table 4). In the case of BD 5, a slight shift in the retention time observed was due mainly to instrumentation interferences and sensitivities during peak reprocessing. The FAMEs obtained from the VSO feedstock source was dominated by tridecanoic acid and 8-octadecenoic acid methyl esters at retention times of 18.12 and 19.80 respectively (Table 4). In the case of the FAMEs derived from UVO as a feedstock source was dominated by the presence of 14-methylpentadecanoic acid and 7-octadecenoic acid methyl esters at retention times of 18.12 and 19.80 respectively (Table 4).

From mass spectral analysis, straight chained saturated FAMES were confirmed from the appearance of two distinct intense and stable peaks for the fragments at m/z = 74 and m/z = 87 as shown in Figure 5 (a-c). These distinct base peaks according to Jabbar et al [37] are due to electron transfer bond cleavages and neutral loss at carbon-2 and carbon-3 from the corresponding acyl group forming intense and stable m/z fragment base peaks of 74 (most abundant) and 87 (second most abundant) as shown in Figure 4. The retention times of saturated FAMEs and their percentage abundances have

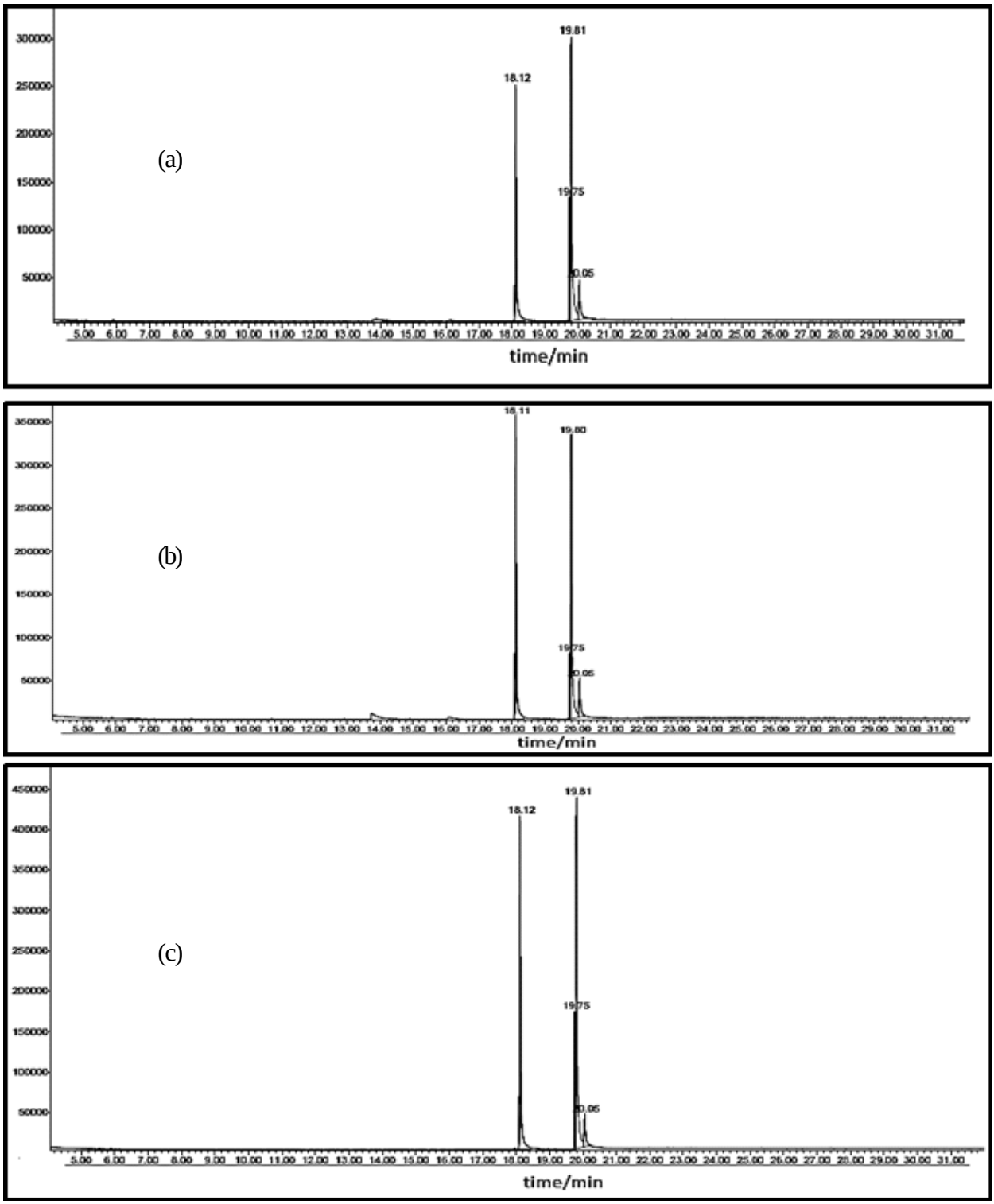

Fig 3: Typical GC-MS chromatograms (Total ion current) of FAMES produced by MI-HF cavitation transesterification analysed by using (a) CPO (b) VSO and (c) UVO feedstock sources

been identified in Table 4. The retention times and percentage abundances of unsaturated FAMEs have also been identified in Table 4, however, identification of the position of the double bonds for unknowns according to Furuhashi et al [38] is difficult to assign as the position of the double bonds cause changes in the retention times in GC analysis. The mass spectra and the NIST 89 library match software referencing system was instrumental in identifying the FAMEs produced as illustrated in Table 4.

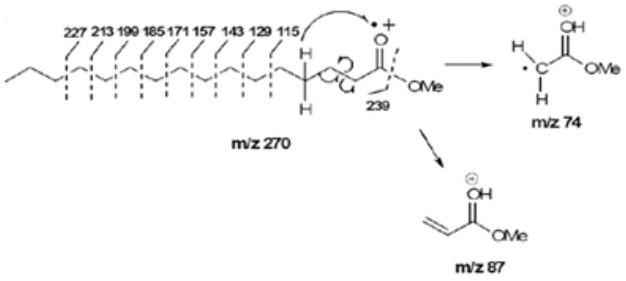

Fig 4: Typical fragment patterns at m/z = 74 and m/z = 87 for tetradecanoic acid as reproduced from Jabbar et al [38].

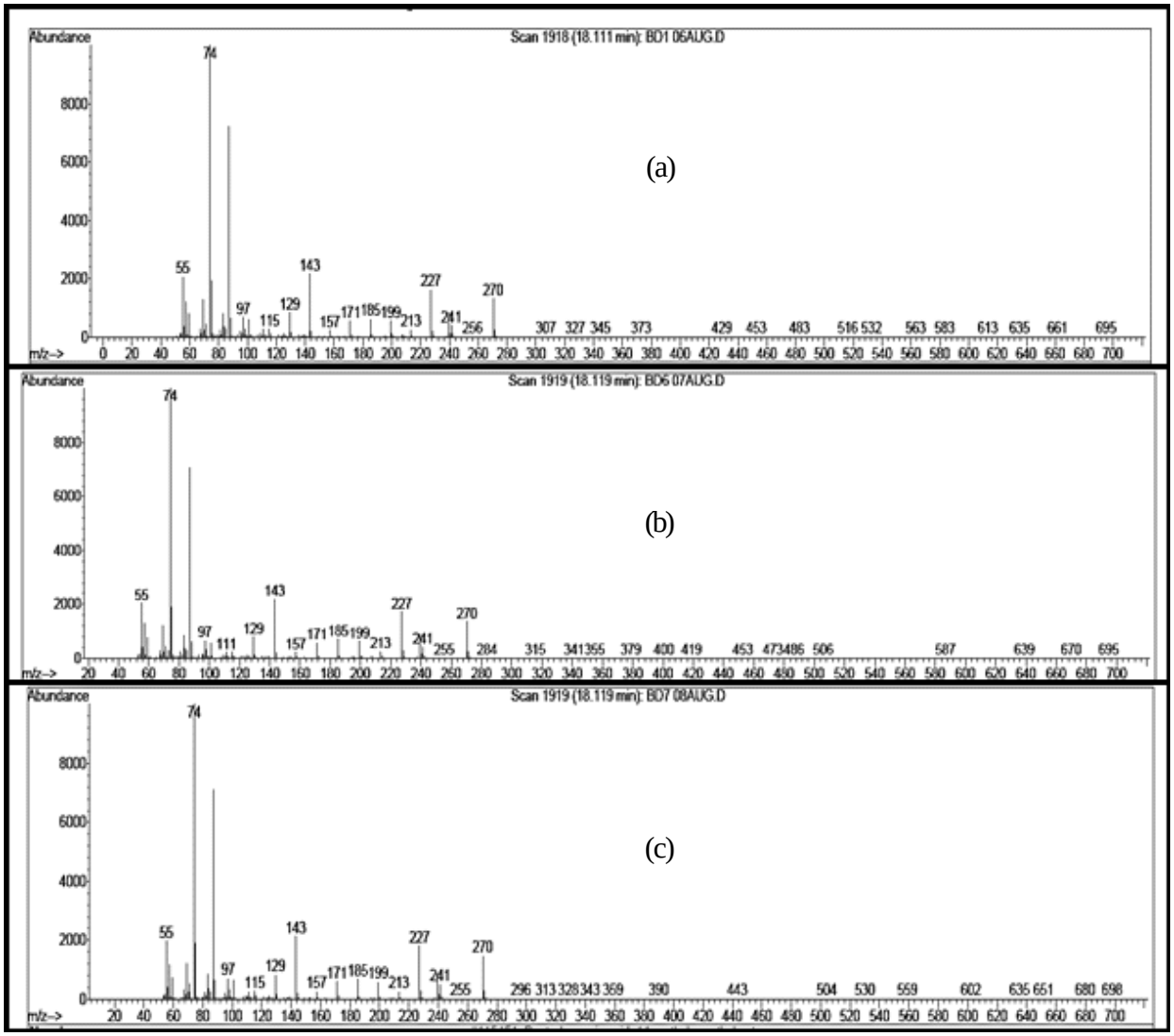

Fig 5: Fragmentation patterns of (a) BD 1 (from CPO) (b) BD 6 (from VSO) and (c) BD 7 (from UVO) showing typical m/z ratios

Table 4: FAME identification from GC-MS data using the NIST 89 Library Resource

Sample	Retention time	Relative Abundance (%)	FAME
BD 1	18.11	41.06	Hexadecanoic acid, methyl ester
	19.75	7.17	9,12-Octadecadienoic acid, methyl ester,
	19.80	43.98	9-Octadecenoic acid, methyl ester,
	20.05	7.79	Octadecanoic acid, methyl ester
BD 2	18.12	29.29	Hexadecanoic acid, methyl ester
	19.75	14.56	9,12-Octadecadienoic acid, methyl ester,
	19.89	49.60	8-Octadecenoic acid, methyl ester
	20.06	6.55	Octadecanoic acid, methyl ester
BD 3	18.12	22.69	Hexadecanoic acid, methyl ester
	19.75	13.56	9,12-Octadecadienoic acid, methyl ester
	19.81	54.65	7-Octadecenoic acid, methyl ester
	20.05	9.10	Heptadecanoic acid, 16-methyl-, methyl ester
BD 4	18.12	26.15	Hexadecanoic acid, methyl ester
	19.74	13.46	8-Octadecenoic acid, methyl ester
	19.80	54.81	9-Octadecenoic acid, methyl ester,
	20.05	5.58	Octadecanoic acid, methyl ester
BD 5	19.08	12.40	Hexadecanoic acid, methyl ester
	20.75	36.83	9,12-Octadecadienoic acid, methyl ester
	20.81	43.76	8-Octadecenoic acid, methyl ester
	21.04	7.01	Octadecanoic acid, methyl ester
BD 6	18.12	32.89	Tridecanoic acid, methyl ester
	19.75	13.38	8,11-Octadecadienoic acid, methyl ester
	19.81	45.56	7-Octadecenoic acid, methyl ester
	20.05	8.17	Heptadecanoic acid, 16-methyl-, methyl ester
BD 7	18.12	37.95	Pentadecanoic acid, 14-methyl-, methyl ester
	19.75	12.25	9,12-Octadecadienoic acid, methyl ester
	19.81	44.20	8-Octadecenoic acid, methyl ester
	20.05	5.60	Octadecanoic acid, methyl ester
BD 8	18.13	26.94	Pentadecanoic acid, 14-methyl-, methyl ester
	19.75	9.52	9,12-Octadecadienoic acid, methyl ester
	19.81	55.39	7-Octadecenoic acid, methyl ester
	20.06	8.18	Octadecanoic acid, methyl ester

Proton and Carbon NMR characterization

FTIR-ATR and GC-MS methods are considered useful techniques to monitor and confirm complete transesterification of feedstock sources to high quality biodiesel. However, both ^{1}H and ^{13}C NMR spectroscopies being sensitive, effective, reproducible and quicker, despite higher instrumentation and maintenance costs, reinforces the monitoring and confirmation of complete transesterification reactions. The ^{1}H and ^{13}C NMR spectra and representative signals identifying complete transesterification of CPO, VSO and UVO feedstock oils used in this study are shown in Figures 6-8, respectively. The assignment of ^{1}H-NMR peaks contained in the synthesized biodiesel was carried out in accordance to the chemical shifts as described by Nakagaki et al [39], Irmawati et al [40] and Sarpal et al [41]. For this study, eight strong chemical ^{1}H-NMR signals at δ (ppm) ranges of 0.78 – 5.31 ppm for BDs 1-5, BD 6 and BD 7-8 were obtained as shown in Figures 6-8 respectively.

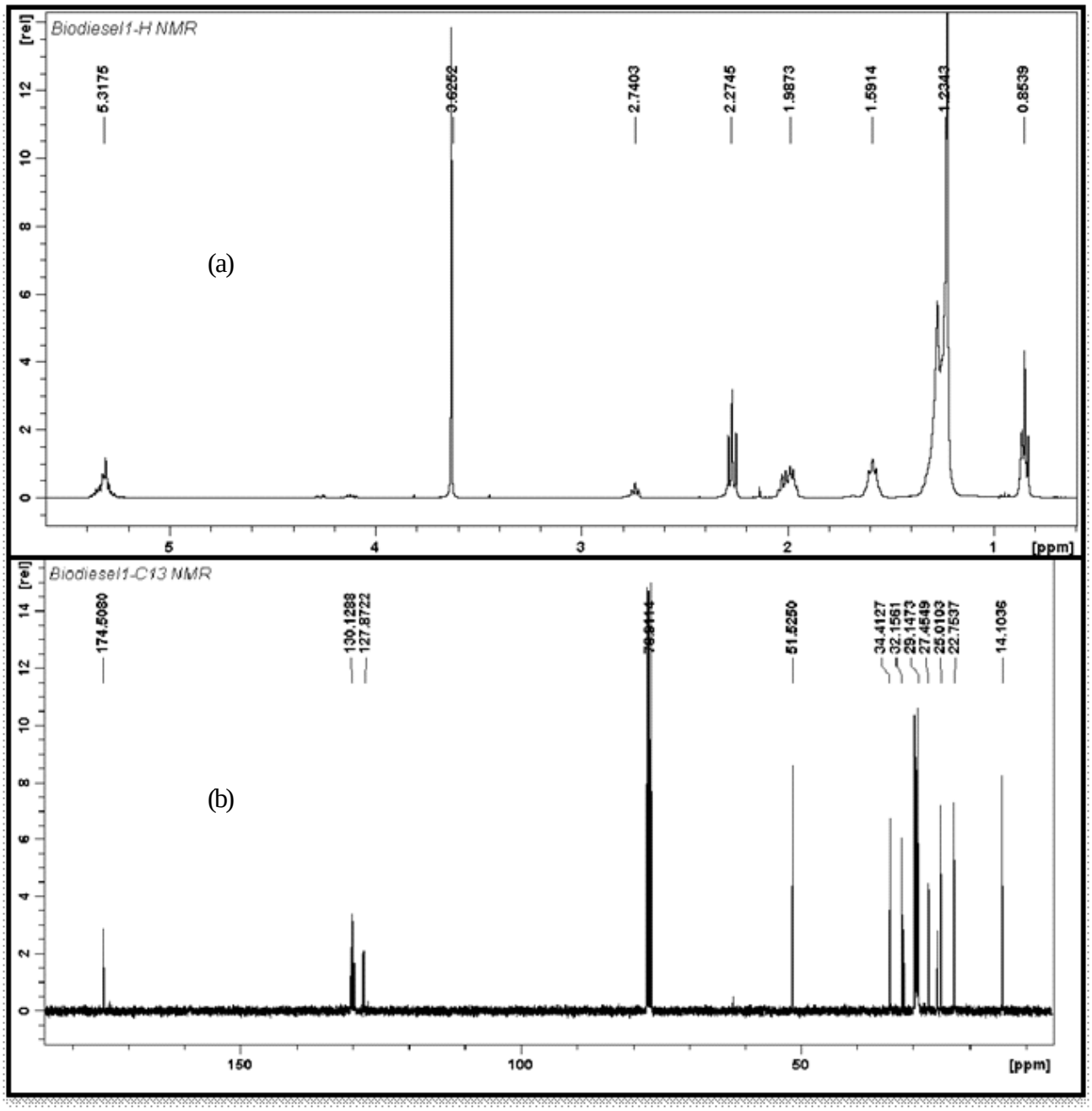

Fig 6: ^{1}H-NMR(a) and ^{13}C NMR (b) spectra of BD 1 produced from a CPO feedstock

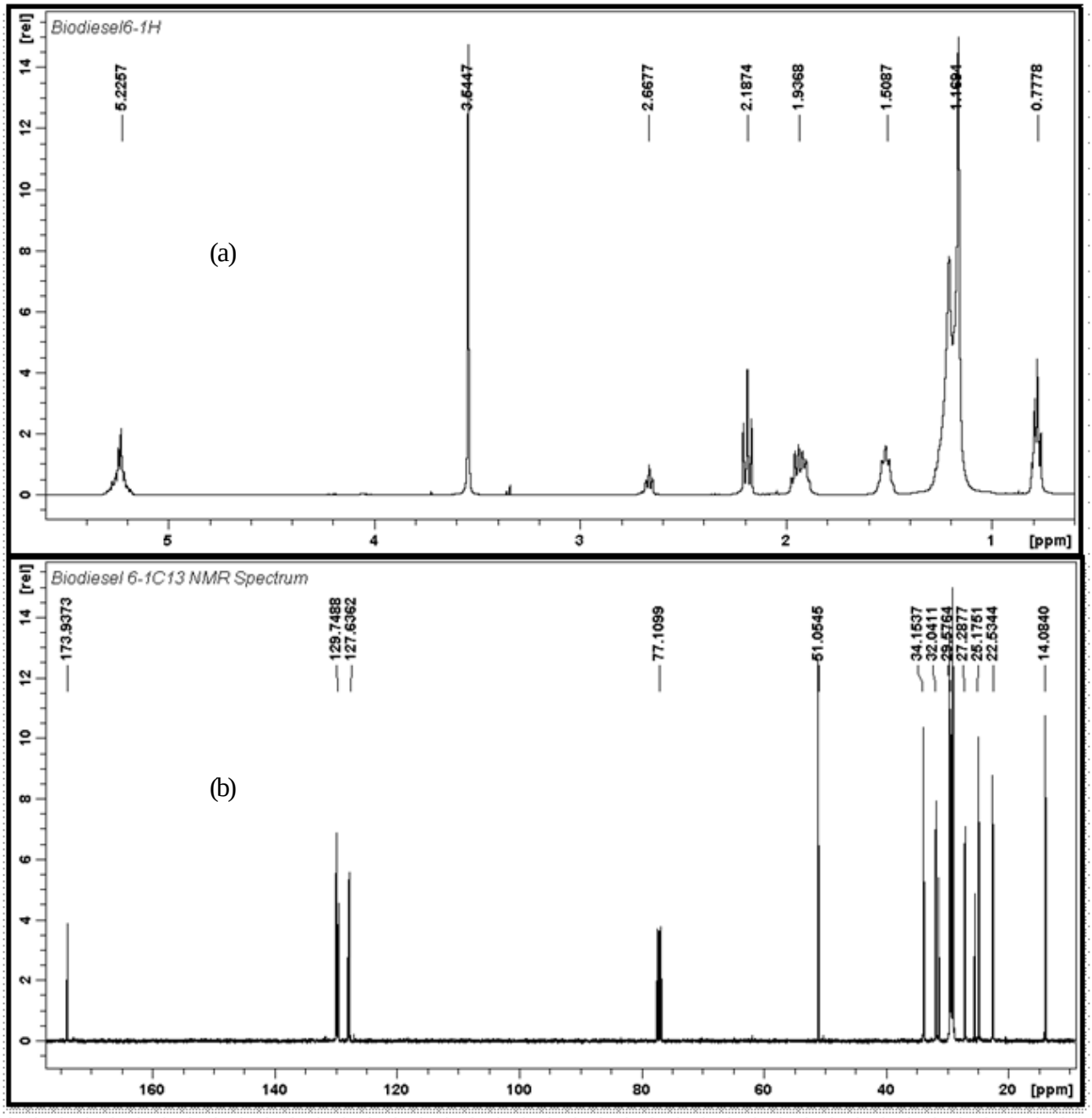

Fig 7: ^{1}H-NMR (a) and ^{13}C NMR (b) spectra of BD 6 produced from a VSO feedstock.

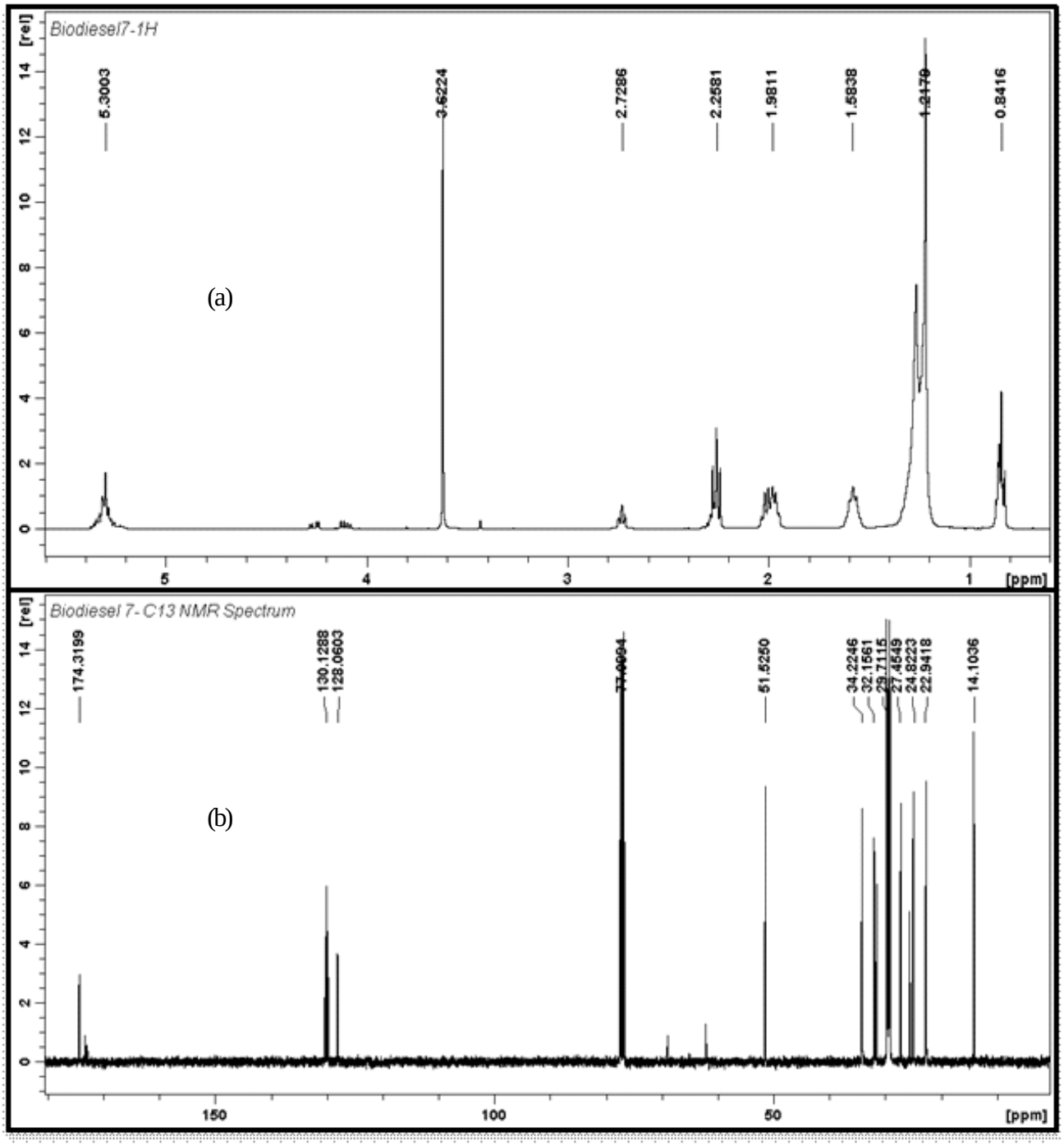

Fig 8: ^{1}H-NMR (a) and ^{13}C NMR (b) spectra of BD 7 produced from a UVO feedstock

The assigned proton shifts in Figures 6-8 from the original feedstock oils revealing complete transesterification and formation of biodiesel are:

Peak 1. Terminal methyl protons (CH_3-C) at δ values of 0.80-0.85 ppm for BDs 1-5 CPO, 0.78 ppm for BD 6, 0.82-0.84 ppm for BDs 7-8; **Peak 2.** Backbone methylenic protons $(-CH_2)_n$- at δ values of 1.18-1.23 ppm for BDs 1-5, 1.18 ppm for BD 6, 1.21-1.22 ppm for BDs 7-8; **Peak 3.** β-Methylenic proton ($-CH_2CH_2COOCH_3$) at δ values of 1.54-1.59 ppm for BDs 1-5, 1.50 ppm for BD 6, 1.55-1.58 ppm for BDs 7-8; **Peak 4.** α-Methylenic proton attached to a single double bond ($-CH=CH_2-$) at δ values of 1.95-1.98 ppm for BDs 1-5; 1.93 ppm for BD 6; 1.98 ppm for BDs 7-8; **Peak 5.** α-Methylenic proton attached to ester ($-CH_2COOR$) at δ values of 2.21-2.27 ppm for BDs 1-5, 2.18 ppm for BD 6, 2.24-2.25 ppm for BDs 7-8; **Peak 6.** α-Methylenic protons attached to two double bonds($=CH-CH_2-C=$) at δ values of 2.69-2.74 for BDs 1-5, 2.66 ppm for BD 6, 2.71-2.72 ppm for BDs 7-8; **Peak 7.** Methyl group protons attached to methyl ester ($-CO(CH_3)O$ at δ values of 3.57-3.62 ppm for BDs 1-5; 3.54 ppm for VSO; 3.60-3.62 ppm for BDs 7-8; **Peak 8.** Olefinic protons (-CH=CH-) at δ values of 5.25-5.31 ppm for BDs 1-5; 5.22 ppm for BD 6; 5.27-5.30 ppm for BDs 7-8.

The characteristic ^{1}H-NMR signals according to Nakagaki et al [39], Irmawati et al [40] and Sarpal et al [41] confirming the presence and subsequent yields of the FAMEs shown in Figures 6-8 can be attributed to the intense singlet at 3.54 - 3.62 due to methyl group protons of the methyl ester and the strong doublet of the methylenic protons at 1.18-1.23 ppm. The absence of signals between δ values of 4.0 – 5.2 ppm is an indication of the high conversion of BDs 1-8 FAMEs, which correlate to the percentage yields as shown in Table 1. Proton signals in this region according to Nakagaki et al [41] typifies hydrogen atoms attached to glycerol. Percentage yield of FAMEs according to Nakagaki et al [39] and Irmawati et al [40] can be calculated from the ^{1}H-NMR signals using Equation 4 as follows:

$$\%\,\text{Yield of FAME} = \left(\frac{2A_{ME}}{3ACH_2}\right)\times 100 \qquad (4)$$

where A_{ME} is area of the strong proton singlet signal of the methyl ester methoxyl group; and ACH_2 is area of the methylenic proton signal. In addition, the derivation factors of 2 and 3 respectively, are derived from the fact that the methylene carbon has 2 protons while the alcohol carbon has 3 protons attached. The ^{13}C NMR spectra are equally useful and sensitive in addition to ^{1}H NMR in confirming complete transesterification and production of FAMEs. The ^{13}C NMR spectra data according to Sarpal et al [41] is advantageous and has a 20 time larger chemical shift range as compared to ^{1}H NMR signals thus displaying highly resolved, sharp and distinct signals. All transesterified feedstock oils showed similar ^{13}C NMR spectra as shown in Figures 6-8. Typical carbon signals have been be assigned to the following functional groups for BDs 1-8 are: α-CH_3 at δ values between 14.08-14.22 ppm;

β-CH_2 and γ-CH_2 at δ values between 22.60 -34.41 ppm;

-OCH_3 at δ value between 51.05-51.57 ppm;

-CH=CH- (unsaturated carbons) at δ values between 127-130 ppm;

-C=O (carbonyl of the saturated and unsaturated fatty esters at δ values between 173.13 - 174.50 ppm. The key characteristic carbon signals positively identifying the FAMEs according to Sarpal et al [41] and those observed typically in these results are the saturated and unsaturated ester signals at 173.13 - 174.50 ppm (C=O) and the methoxy ester group at 51.05 - 51.57 ppm. The consistency seen from the ^{1}H and ^{13}C NMR chemical shifts signals is a strong indication of the consistency and efficiency of the process of MI-HF cavitation transesterification as a useful tool in obtaining complete transesterification, with high yields and a high quality end product in FAMEs.

In the final analysis of data from this study, it can be inferred that most other methods have imposed addi-

tional processing steps, adjustment of acid and base catalysts, and introduction of specialized homogeneous and heterogeneous catalysts in transesterification of used or waste vegetable oils to obtain high yields of an acceptable quality. This method showed an ease of application to the transesterification of used and waste oils without any modifications and additions to the process. The instrument itself is not a complicated system and once assembled allows a stable and easy operation with a high degree of safety thus enabling it to be implemented as a highly cost effective method for the preparation of a clean and high quality biofuel from both used and virgin feedstock oil sources.

Conclusions

The application of magnetic-impulse high frequency cavitation as a one-step batch transesterification process proved to be extremely efficient in transesterifying used or waste vegetable oils into a high quality biodiesel comparable to that obtained from crude palm and virgin sunflower feedstock oil sources. Such a process circumvents and minimizes the need for pre-work up, pre-treatment of virgin and used vegetable feedstock oils, addition of side processes and modifications was achieved at a low electrical power, low reaction temperature of 50°C and a fast reaction time of 40 mins and with yields exceeding 95%. The high quality of biodiesel was confirmed by its high calorific value, high viscosity, high flash point, low total glycerol, low moisture, acceptably low acid value, negligible or low (trace) sulfur and negligible or low (trace) phosphorus levels.

References

1. Fonseca F.A.S., Vidal-Viera J.A. and Ravagnani S.P., 2010, *Bioresource Technology*, **101,** 8151 – 8157.

2. Barnwal B.K. and Sharma M.P., 2005, *Energy Reviews* **9**, 363 – 378.

3. Junne S. and Johannes Kabisch J., 2016, *Eng. Life Sci.,* 1–13.

4. Gustafson C.R., A publication of the American Agricultural Economics Association, Third Quarter, 2003.

5. Yin X., Ma H., You Q., Wang Z. and Chang J., 2012, *Applied Energy*, **91**, 320 – 325.

6. Ramachandran K., Sivakumar P., Suganya T. and Renganathan S., 2011, *Bioresource Technology*, **102**, 7289 – 7293.

7. Zayed M.A., Mamoun S.M. El-Kareem A. and Zaky N.H.S., 2017, *J. Pharm. Appl. Chem.*, **3** (2), 109-116.

8. Pal A., Verma A., Kachcwaha S.S. and Maji S., 2010, *Renewable Energy*, **35**, 619 - 624.

9. Stavarache C., Vinatoru M., Maeda Y. and Bandow H., 2007, *Ultrasonics Sonochemistry* **14**, 413 – 417.

10. Cao P., Dubé M.A. and Tremblay A.Y., 2008, *Biomass Bioenergy*, **32**, 1028–1036.

11. Ataya F., Dubé M.A. and Ternan M., 2008, *Energy Fuels*, **22**, 3551–3556.

12. Narváez P.C., Sánchez F.J. and Godoy-Silva R.D., 2009, *J. Am. Oil Chem. Soc*., **86**, 343–352.

13. Behzadi S. and Farid, M.M., 2009, *Bioresour. Technol.,* **100**, 683–689.

14. Lertsathapornsuk V., Pairintra R., Aryusuk K. and Krisnangkura K., *100 Fuel Process. Technol.,* **89**, 1330–1336.

15. Veljkoviæ V.B., Avramoviæ O.S. and Stamenkoviæ O.S., 2012, *Energy Reviews*, **16**, 1193 – 1209.

16. Maniam G.P, Hindryawati N, Nurfitri I., Jose R., Rahim M.H.A. and Yusoff M.M. Proceedings Venice 2014, Fifth International Symposium on Energy from Biomass and WasteSan Servolo, Venice, Italy; 17-20, November 2014.

17. Atabania A.E., Silitonga A.S., Badruddina I.A.,

Mahliaa T.M.I., Masjukia H.H. and Mekhilefd S., *Renewable and Sustainable Energy Reviews,* **16,** 2070 – 2093.

18. Flint E. B. and Suslick K.S., 1991, *Science*, 253, 1397.

19. Suslick K.S., 1989, *Scientific American.*

20. Bang J.H. and Suslick K.S., 2010, *Adv. Mater.*, **22**, 1039–1059

21. Suslick K.S., 1995, *MRS Bull.* **20,** 29.

22. Suslick, K.S., 1998, Kirk-Othmer Encyclopedia of Chemical Technology; 4th Ed. J. Wiley & Sons: New York, **26**, 517-541.

23. Thanh L.T., Okitsu K., Sadanaga Y., Takenaka N., Maeda Y. and Bandow H., 2010, *Bioresource Technology,* **101**, 639 – 645.

24. Operation Manual to the device PULSAR-ST 215-B, Cavitation Technology, 2011.

25. Van Gerpen J., Shanks B., Pruszko R., Clements D., and Knothe G. Biodiesel Analytical Methods. National Renewable Energy Laboratory, NREL/SR-510-36240, 2004.

26. Salamantinia B., Abdullah A.Z. and Bhatia S., 2012, *Fuel Processing Technology,* 97, 1-8.

27. Monteiro R.M., Ambrozin A.R.P., Lião L.M. and Ferreira A.G., 2008, *Talanta,* **77**, 593 – 605.

28. Ramírez-Verduzco L.F., Rodríguez- Rodríguez J.E. and Jaramillo-Jacob A. del R., 2012, *Fuel* **91**, 102 – 111.

29. Pinzi S., Gandía L.M., Arzamendi G., Ruiz J.J. and Dorado M.P., 2011, *Bioresource Technology,* **102**, 1044 – 1050.

30. Ghanei R., Moradi G.R., Taherpour Kalantari R. and Arjmandzadeh E., 2011, *Fuel Processing Technology*, **92**, 1593-1598.

31. Certificate of calibration issued by the Poulten Selfe and Lee LTD calibration laboratory, 2005.

32. ASTM D 93, Annual Book of ASTM Standards, Vol. 05.01, Petroleum Products and Lubricants, 1983.

33. Munari, F., Cavagnino, D. and Cadoppi, A., 2007, Thermo Fisher Scientific, Milan, Italy, **13**, Application Note: 10212.

34. Bautista L.F., Vicente G., Rodríguez R. and Pacheco M., 2009, *Biomass and Bioenergy*, **33**, 862 – 872.

35. Rashid U., Farooq Anwar F. and Knothe G., 2009, *Fuel Processing Technology,* **90**, 1157–1163.

36. South Africa National Standard (SANS 1935:2011). Automotive biodiesel – fatty acid methyl esters (FAME) for diesel engines – requirements and test methods, 2011.

37. Jabbar A., Ali A., Tawab A., Haque A and Iqbal M., 2014, *J. Chem. Soc. Pak.,* **36(1)**, 140-149.

38. Furuhashi T., Nakamura T., Fragner L.1, Roustan V, Schön V and Weckwerth W., 2016, *Biotechnol. J.*, **11**, 1262–1267.

39. Nakagaki S., Bail A., dos Santos V.C., de Souza V.H.R., Vrubel H., Numes F.S. and Ramos L.P., 2008, *Applied Catalysis A: General* **351**, 267 - 274.

40. Irmawati1 R., Shafizah I., Nur Sharina A., Ahangar H.A. and Taufiq-Yap Y.H., 2014, *Energy and Power*, **4(1):** 7-15 DOI: 10.5923/j.ep.20140401.02.

41. Sarpal A.S., Silva P.R.M., Monteiro T.V., Fonseca M., Cunha V.S., and Daroda R.J., 2016, *J. Sci. Ind. Metrol.*, 1:3, 1 - 25.

RNI No. MAHENG/2017/74063
ISSN No. (Print) 2581-5911
ISI Impact Factor 0.883 (2018)

Environment friendly Ca/Zn Stabilizers for the Thermal Stability of Rigid PVC Applications and Comparative study with Conventional One Pack Stabilizer

Mahesh B. Waykole[1], Rama S. Lokhande[1] and Anand P. Gokhale[2],
[1] School of Basic Sciences, Department of Chemistry, Jaipur National University, Jaipur (Rajasthan), India.
[2] Head Research and Development Lab, Galata Chemicals Pvt. Ltd.
Galata Chemicals India Pvt. Ltd, Mumbai, India.
Email: maheshbw72@yahoo.co.in

Abstract
Environment concern over replacement of lead stabilizers from PVC industries is forcing PVC pipe manufacturers to redesign the formulation. New developed one pack stabilizing system based on calcium and zinc salt offers good early color retention and long-term stabilization efficiency in rigid formulation. Comparative studies have been done with conventional stabilizers like lead one pack system, Ca-Organic, tin and new innovative stabilizers. The thermal stability was evaluated by Congo red testing in air at 200^{0}C, thermal aging test, thermo gravimetric analysis and Torque rheometry study at 200^{0}C. Visual color evolution and thermal stability time were examined at 190^{0}C in air. The experimental results showed that combination of innovative stabilizers is able to extend stabilization time of PVC and postpone zinc burning and exhibit greater stabilizing efficiency than lead one pack stabilizer.

Keywords: *Poly (vinyl chloride) (PVC), Ca/Zn stabilizers, Thermal properties, Degradation, Torque rheology*

Introduction

Chlorine containing polymer such as PVC, is an important thermoplastic polymer and widely used in water pipes, floor, roof tiles, packaging films and sheets due to cost performance benefit. More attention has been drawn towards their applications, modifications and degradation[1,2,3,4,5,6]. The advantage of Poly vinyl chloride is its non-flammable nature and good performance[7]. It is a cost competitive polymer with excellent properties, flexibility and rigid application. However, it is known that PVC is very thermally unstable at elevated temperatures and releases Hydrochloric acid (HCl) that accelerates degradation process. The processing range of temperature is much higher than glass transition temperature 70^{0}C. PVC undergoes several changes in inherent structural chain. The thermal degradation creates autocatalytic dehydrochlorination reaction, which may produce unacceptable discoloration due to formation of conjugate double bonds or polyene sequences–$(–CH=CH–)_n$, and loss of mechanical strength[8]. Mainly carboxylate salts of calcium and zinc are used for stabilization of PVC. Zinc carboxylate which produces $ZnCl_2$ can cause sudden dehydrochlorination of PVC during stabilization. The HCl released causes several colorations of polymer. The color changes from white

to yellow, brown and finally black. It was due to labile sites that dehydrochlorination was prominent in allylic chlorines and tertiary chlorines. Proper stabilizers must be added in order to restrain the degradation of PVC during processing [9,10]. Stabilizers can inhibit degradation of removal of HCl due their special properties of adsorption of HCl [11].

However, to retard dehydrochlorination of PVC, stabilizers such as lead salts, metal soaps, organotin and rare earth metals are used. However, some of them are toxic and cause environment problems, as most of them leave residue after degradation of polymer [12]. Applications of lead salts and organo stabilizers are limited due to their toxicity and heavy metals, though they have high efficiency to stabilize PVC. Ca/Zn stabilizers are restrained as they have low stabilizing efficiency. New kind of high efficiency stabilizers such as polyols[13,14], hydrotalcite (LDH) like materials have very important application in stabilization of PVC[15,16,17,18]. Researchers have done studies on Ca/Zn thermal stabilizers as they are nontoxic and environment friendly, but they still have problems of long-term stability[19]. The synergistic mechanism of $CaSt_2$ and $ZnSt_2$ was widely investigated by many researchers. Calcium stearate and zinc stearate play an important role in PVC stabilization as they are nontoxic. However, they need long term stabilization by adding some co-stabilizers for improvement [20]. Generally, addition of auxiliary stabilizers like polyols[21,22], α–diketones [23,24] to $CaSt_2$/$ZnSt_2$ is necessary to get improved performance. Studies on the calcium salt of metilox acid (CaM) as thermal stabilizer for rigid PVC have not been reported. The present study investigates the possible thermal stabilizer which can bind liberated HCl from PVC. In this research, a new developed one pack system is compared with Lead one pack, Tin and Ca-organic stabilizers.

Materials and Methods

Materials

The PVC, used in this work was PVC K value 67 resin supplied by Reliance Industries Ltd, India, calcium carbonate was purchased from MRB, Vietnam. Calcium stearate ($CaSt_2$), Zinc stearate (ZnSt2) was supplied by FACI Singapore PTE. Acetone AR grade was obtained from SDFCL. Lead stabilizer (Lead content: 19-21% as per TDS) was supplied by Mona Chem Additives, Vadodara, India. Titanium dioxide was provided by Dupont India Ltd, and lubricants like polyethylene wax and oxidized polyethylene wax were supplied by Honeywell Corporation. B-22 impact modifier was obtained from Kaneka Corporation.

PVC sample preparation

All experiments were performed with master batch of PVC dry blend. The PVC samples for static oven test and evaluation of colour test were prepared by mixing master batch with additives as reported below:-

Table 1. Specific components of the PVC master batch without stabilizer before milling

Rigid PVC Formulation	Qty Phr
PVC K-67	100
$CaCO_3$	8
TiO_2	1
External Lubricant	1.2
Internal Lubricant	0.3
Impact modifier	4.3
Ca. St_2	0.7

Synthesis of Novel thermal stabilizer

The synthesis of novel stabilizer was a two step reaction. Calcium salt of metilox acid was synthesized through reaction of metilox acid with Calcium hydroxide.

The synthesis had two steps. In the first step, reaction hydrolysis of Metilox ester was done.

Initially 100 mL methanol was added to a four neck one litre round bottom flask equipped with Dean-Stark apparatus, thermometer pocket, overhead stirrer, reflux condenser with drying tube and dropping funnel for addition. Metilox ester 50g (0.17mol) was added slowly under vigorous stirring at 300 rpm to the reaction flask. Mixture of NaOH (0.17mol) solution in 100 mL methanol was added slowly to the reaction flask using dropping funnel over a period in 20 min. After addition,

reaction mixture was refluxed for 1 hr by applying external heating. Then methanol was reovered by means of Dean Stark apparatus by adding demineralized (DM) water to the reactor simultaneously. Reaction mass was cooled to room temperature and acidified with (10%) dilute HCl. Reaction mass was stirred for 30 min and filtered off and the mass was washed by DM water and then acetone. The product metilox acid was obtained. The yield of metilox acid was (44.9g) 94.5% which was powdered for use after drying.

In the second stage, metilox acid obtained from first stage 30g (0.107 mol) was used for preparation of calcium salt. Calcium salt was synthesized from calcium hydroxide and metilox acid. Initially the metilox acid (0.107 mol) was introduced in 200 mL toluene in a four neck round bottom flask equipped with Dean-Stark apparatus and reflux condenser, thermometer pocket and overhead mechanical stirrer. Then, to the reaction mass, 0.053 mol of calcium hydroxide was added slowly at 50^0C in 1 hr. The reaction was carried out at 80^0C for 1 hr and the generated water was recovered by Dean Stark apparatus. Finally, toluene was recovered by stripping with methanol. The reaction mixture was cooled to RT and then 20^0C and filtered. Wet cake was washed with 50 mL acetone. The product calcium metilox was dried under vacuum for 3 hrs. The reaction yield was 91.6%.

Table 2. Stabilizer composition

All composition quantity in PHR		
Compounds	Expt. 1	Expt. 2
Zn St_2	0.4	0.4
Ca. St_2	0.6	0
Ca. M	0	0.6
β-diketone	0.2	0.2
Assisting additives	1.3	1.3
Total	2.5	2.5

The PVC master batch was prepared by blending of PVC having value K-67, CaCO3 (powder), Titanium dioxide pigment (powder), polyethylene wax (AC617A) as external lubricant, oxidized polyethylene wax (AC316A) as internal lubricant and $CaSt_2$ in high speed mixture for 2min. The specific components are shown in Table 1. The master batch was mixed with 2.5 phr (per hundred resin) Ca/Zn stabilizer for evaluation of stabilizing efficiency and 2phr of market control lead stabilizer. Then the above prepared PVC master batch (Table 1) was mixed with 2.5 phr experimental stabilizers. Seventy grams of blend with stabilizer was placed on Twin Roll Mill (Neoplast Ahmedabad, India). The front roll and rear roll temperatures were 195°C and 190°C respectively and the sheet drawn after 3 min. The prepared sheet having thickness 1mm was used for further study.

Measurements

Congo Red Test

A Congo red test was done to evaluate the rate of PVC dehydrochlorination when heated at 200^0C in air. Congo Red measurement test was done according to IS-5831. PVC film was prepared as per Table 1 with 2.5 phr of Ca/Zn and 2phr market control lead stabilizer. The thermal stability static time (tss) of stabilizer was obtained by heating 0.0500g of PVC sample (by fragmentation of PVC sheet into 0.2 mm squares) in the test tube. Congo Red paper was placed at the top of the test tube. The test tube was placed in Congo Red stability apparatus [Veekay Apparatus, Mumbai] having electrical heating at 200^0C ±1. Congo Red paper changed colour from red to blue by degradation of PVC sample, which was due to liberation of HCl. The time required for colour change represents the thermal stability of that sample.

Thermal Ageing Test

The thermal aging test was carried out in hot air circulating temperature-controlled by oven [ELE, Ahmedabad]. The thermal aging test was performed as per ASTM D-2115. The PVC samples were cut in to 30mm x 20mm rectangular shapes strips and put into the oven at 190^0C. Samples were removed after every 5min interval and subjected to visual examination. Colour scanning was done using colourscan 5100H [Premier colour scan 5100H]. Color measurement of PVC sheets

were investigated by spectrophotometer and whiteness and yellowness index values measured according to ASTM E313.The effect of stabilizers was evaluated by colour difference of PVC samples. Whiteness and yellowness index clearly indicated differences of stability of stabilizers.

Impact Strength of Various Stabilizers

The impact strength test was used to measure directly the total energy required to break the test specimen by impact [25]. PVC, especially rigid products at risk of possible damage by impact at some point during their lifetime, either through accidental hits or drops. (e.g. PVC product during transport, installation and storage) were tested. First the samples were prepared using compression moulding press, then cut to standard size. The method of testing employed was ASTM 256. The rigid PVC samples were cut in 64 x 12.7 x 3.2 mm sizes. Test samples were conditioned at 23^0C for 5 hrs. Readings were taken as an average of three samples. The tests were carried out by cutting the PVC samples to a depth of 1 mm.

Rheological study of Stabilizers on Brabender

In this study, Brabender torque rheometer was used to study the process ability of PVC compound with stabilizers. The shear flow properties of PVC master batch with experimental stabilizers were studied using Brabender plasticodore PL2000. Fusion behaviour and degradation time of compounds were studied using Brabender torque plastogram at 200^0C at rotor speed at 60 rpm. 65 g of above master batch (Table 1) was mixed with stabilizer and placed in mixing chamber. A 5 kg loading chute was used to introduce material into the mixer chamber as quickly as possible to get reproducibility. The fusion behaviour was studied by observation of changes in torque, temperature and time.

Results and Discussion

The stabilisers used in the study are given in Table 3. The dosage of the lead stabilizer was 2phr, whereas the dosage of the Ca/Zn stabilisers was 2.5 phr and tin stabilizer 1 phr. It is accepted in the pipe industry that Ca/Zn stabilisers are weaker than lead or tin stabilisers and a higher dosage of Ca/Zn stabilisers are required. Generally, a 25 -50% increase in the dosage is accepted. We have conducted our studies at 25% dosage.

Thin Layer Chromotography (TLC)

Hydrolysis of metilox ester to metilox acid were monitored by TLC with respective to the starting material. During synthesis, Benzene propanoic acid and 3,5-bis(1,1-dimethylethyl)-4-hydroxy -methyl ester (Metilox) were converted to Metilox acid. Formation of acid was confirmed by TLC with suitable mobile phase under UV light (254 nm) using silica gel (60-120 mess). All the spots of acid and ester were visible under UV and Iodine clearly. Ester compound got hydrolysed to acid.

TLC of after hydrolysis of Metilox ester

TLC in suitable module phase

1. Metilox (Ester)
2. Acid of Metilox

TLC in iodine chamber

Fourier Transform Infrared Spectroscopy analysis was used to confirm the presence of functional group of metilox acid. In first stage, hydrolysis of metilox ester occured and the resulting compound metilox acid was taken for FITR analysis. Figure 4.2 shows IR spectrum recorded at Miracle ATR and scanned FTIR range was 4000cm^{-1} to 600 cm^{-1}. The bands at 3628 cm^{-1} are due to -OH stretching frequency of hindered phenolic group. The bands at 3003 cm^{-1} for OH stretching frequency correspond to acid group. The IR spectrum reveals the presence of -COOH group. The nature of IR spectrum is broad over 3043 cm^{-1} and shows a sharp strong peak at 1701 cm^{-1}. In FTIR spectrum (Figure 4.3) the conversion of -COOH group to -COOZn is clearly seen. Calcium salt does not show characteristic peak at 1701 cm^{-1}. The peaks at 1543,1431 cm^{-1}are due to stretching vibrations of carboxylic soaps.

Characterization of Calcium Metilox

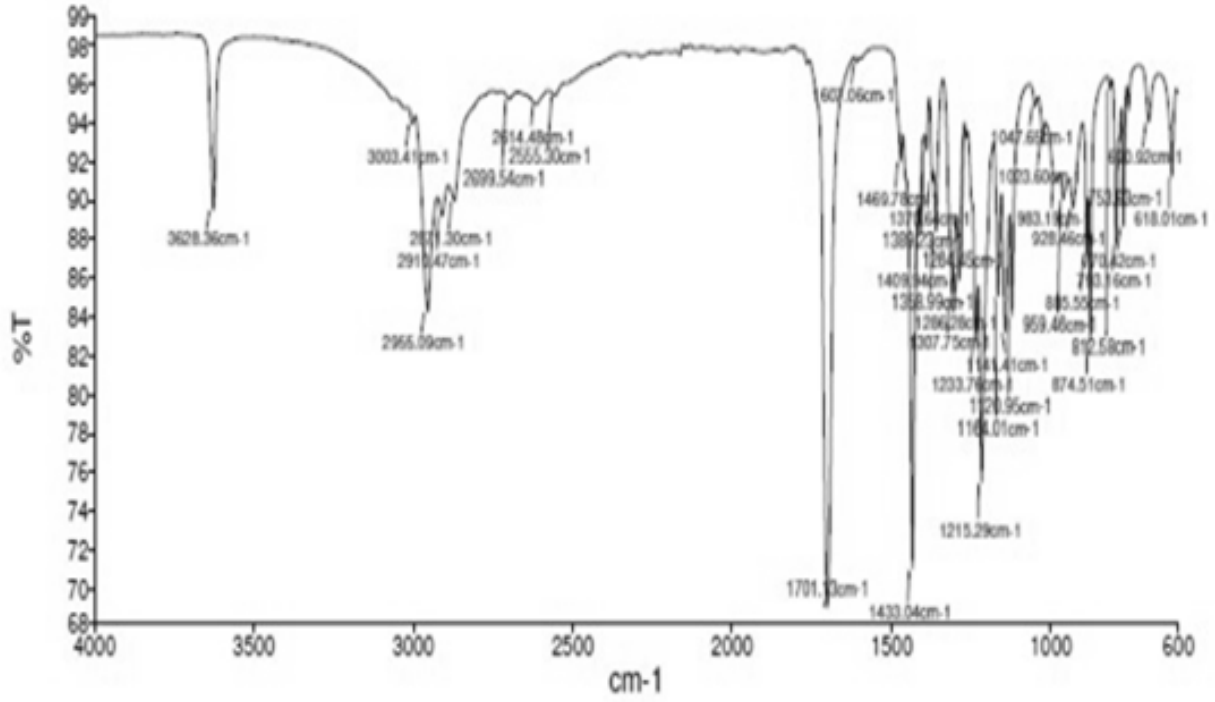

Fig 2. FTIR of Metilox acid

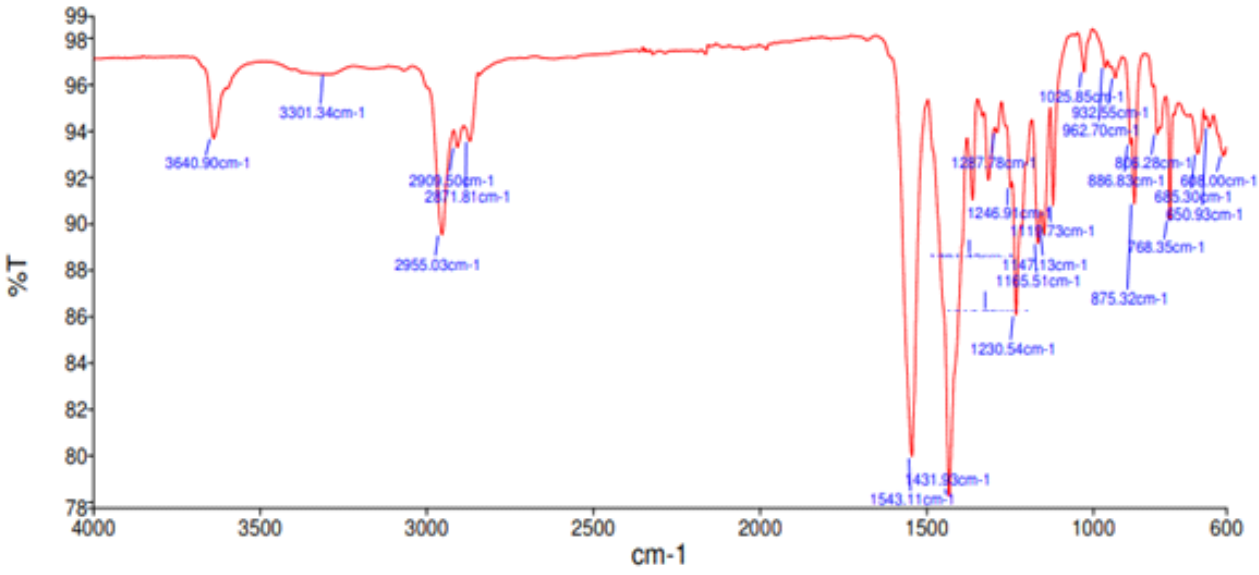

Fig 3. Calcium salt of metilox acid

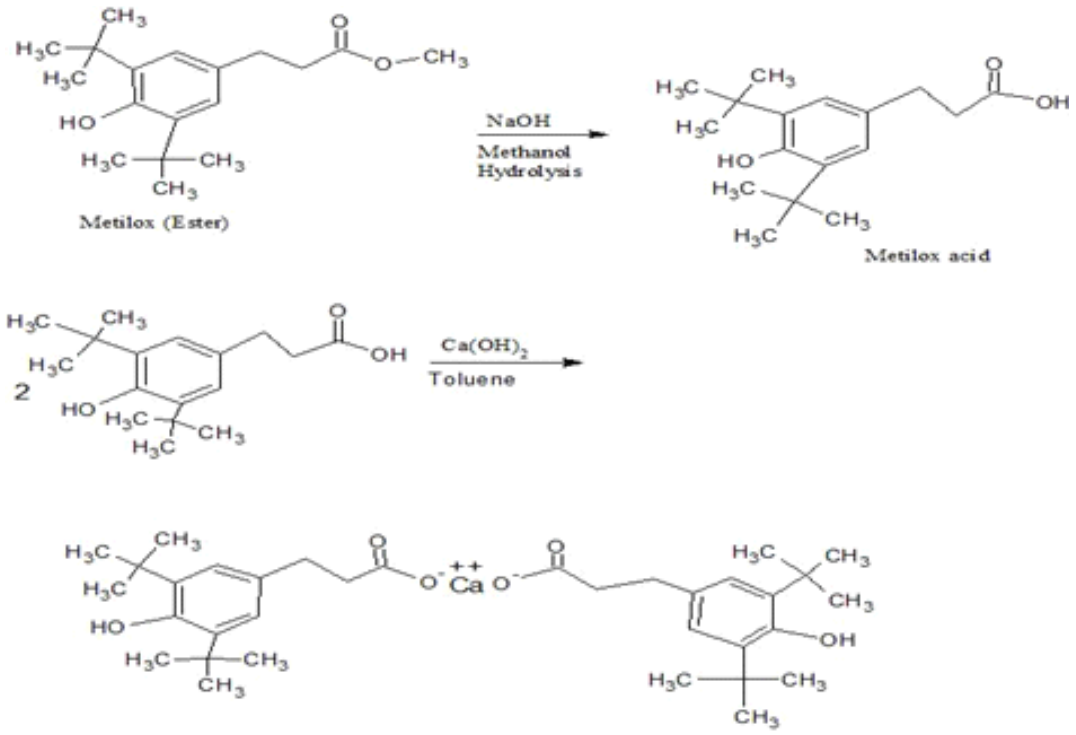

Calcium Salt of Metilox Acid

Structure of Calcium Salt of Metilox Acid

Congo Red Testing

In order to get proper thermal heat stability of PVC, strong heat stabilizers are needed. The dehydrochlorination rate of stabilizers is measured as stability time (ts). The one pack system made from Zinc stearate and Calcium salt of metilox acid in the presence of other assisting additives shows better thermal of stability time (ts) of PVC as compared to the market control lead one pack stabilizer. It is seen that thermal stability time (ts) of CAM incorporated PVC is 25min, while PVC stabilized with calcium organic stabilizer showed 17min. Tin stabilizer shows highest thermal stability among all stabilizers at 29 min. Tin based stabilizer, in the stabilization mechanism adds to the defective site on PVC backbone and tin chloride is formed. It has been seen that CaM with zinc stearate along with other additives exhibit greater thermal stability and increases stability time(ts) substantially. PVC stabilized with Ca/Zn shows weak thermal stability. Lead stabilizer has 22 min stability time i.e. dehydrochlorination rate is slow compared to other stabilizers. It retards the release of HCl from PVC during degradation as it has higher efficiency to bind HCl. During degradation, lead chlorides are formed which do not take part in further PVC degradation.

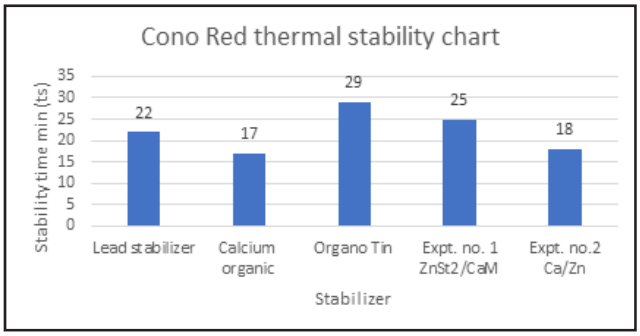

Fig 4. Congo red stability time (ts) min

Discoloration of Rigid PVC sheets containing Various type of stabilizers

Fig 5. Oven Stability test for stabilizers. Color changes of PVC strips at 190^{0}C.

Experiment 1: $ZnSt_2$/CaM, Experiment 2: Ca/Zn

The thermal ageing test gives discoloration behaviour for the thermally degraded PVC. For yellowness and whiteness index, ASTM E313 method was used. Lead one pack system has strong stability as the formation of lead chloride is one of the significant advantages in lead stabilization and has no destabilising effect on PVC molecule. Organo tin stabilizers have long term stability among all stabilizers. Additives based on tin bonded to at least one sulphur bond (thiotins) or sulphur free organotin compounds bonded to derivatives of carboxylic acid are strong thermal stabilizers. Thio tin is able to substitute labile chlorine atoms. They are also capable of hindering autoxidation which make them powerful long-term stabilizers. As shown in Fig. 5, tin stabilizer shows no color change till 15 min. Initial color remains till 30 min. While lead stabilizer initially was white, the onward discoloration was very slow. Calcium organic stabilizer stability is up to 10 min. Calcium salt of metilox acid with stabiliser shows excellent thermal stability. Metilox ester is starting compound for reaction of antioxidant like Irganox 1010 and 1076, which improves and extends discoloration of PVC. The same logic has been used for preparation of CaM. As seen from Figure 5, the thermal stability of stabilizer containing of Ca/M shows excellent thermal stability.

There is no change in color till 15 min, onwards from 20 min to 35 min brown color develops gradually. This shows the ability of CaM to retard degradation of PVC.

Whiteness Index of PVC sheets

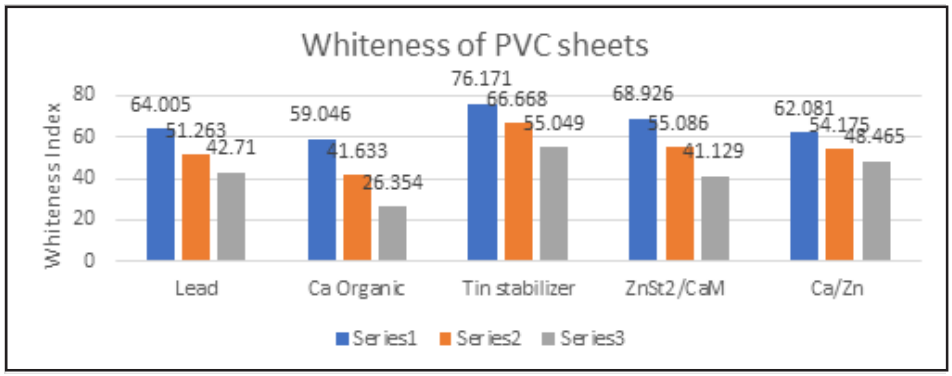

Fig 6. Colorimeter data of whiteness for PVC strip made with different stabilizer

Table 3. Yellowness Index value of PVC sheets stabilized with various stabilizers

Time(min)	0	5	10	15	20	25	30	35
Lead	8.111	14.552	19.221	23.846	28.172	29.869	34.034	37.535
Ca Organic	13.067	22.297	30.748	42.438	48.144	51.676	56.58	59.779
Tin	2.153	6.971	13.683	18.838	29.322	32.529	37.451	38.646
$ZnSt_2$/CaM	5.475	13.723	18.192	21.216	26.885	30.390	33.265	35.270
Ca/Zn	11.056	29.934	36.979	44.130	50.128	59.223	60.618	59.888

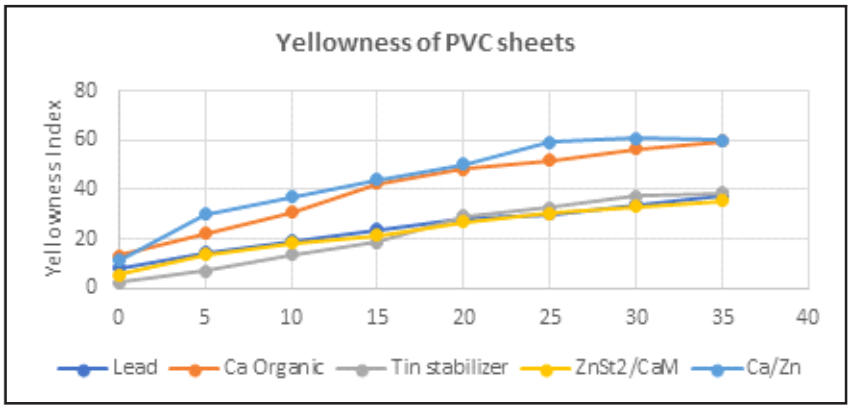

Fig 7. Thermal stability of experimental stabilizers compared with lead one pack stabilizer. Color changes for PVC samples in Oven Stability Test @190^{0}C [Yellowness Index].

The ability of various stabilizers like Lead, Ca-organic, Tin, $ZnSt_2$/CaM and Ca/Zn was evaluated by comparison of colorimeter data. Discoloration of PVC stabilized with Tin stabilizers have high stabilizing among all stabilizers. The method indicates that there is close relation between discoloration and formation of HCl, which increases intensity of yellowness. Lead stabilizer has strong color retention. From the color index data, it is concluded that stabilizing efficiency of stabilizer containing CaM through the replacement of labile chlorine, shortened the polyene sequences which is responsible for PVC degradation.

Izod impact test of various stabilizers

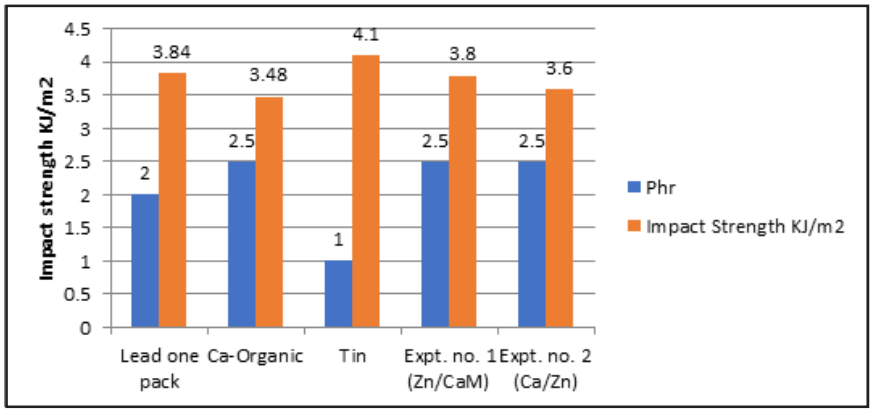

Fig 8: Impact strength of various stabilizers

Rheology of experimental stabilizers with commercial stabilizers

Rheology of commercial and experimental stabilizers have been studied. The data obtained from Brabender Plasticodore 2000 is shown in Table 5. Fusion torque, time and stability study ws done for stabilizers. Lead, Tin, Ca-Organic, Experiment No.1 (Zn/CaM) and Experiment No.2 (Ca/Zn).

Brabender Plastogram

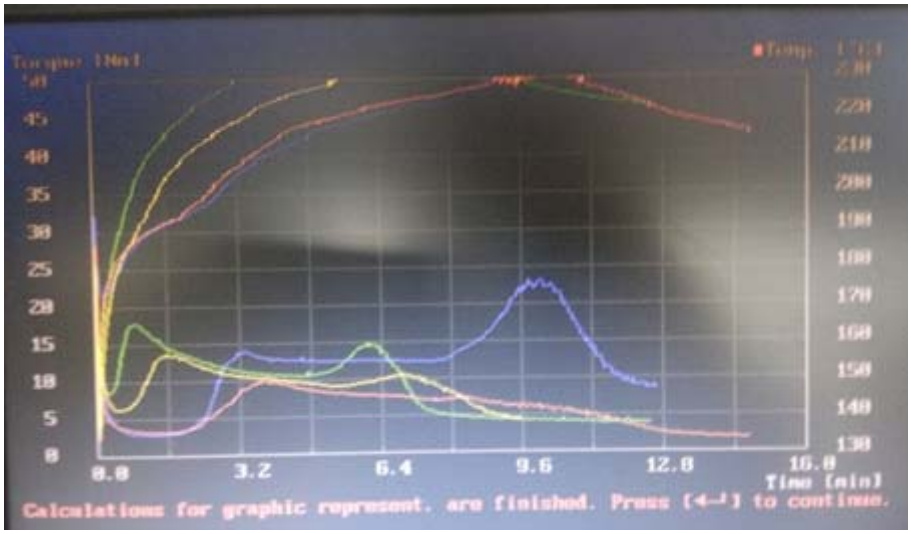

Fig 8. Torque curve of Lead, Ca-Organic, Tin and experimental stabilizers.

Color code	Stabilizer
Blue	Lead one pack
Green	Tin stabilizer
Yellow	Expt. no.1 (ZnSt2/CaM)
Red	Expt. no.2 (Ca/Zn)

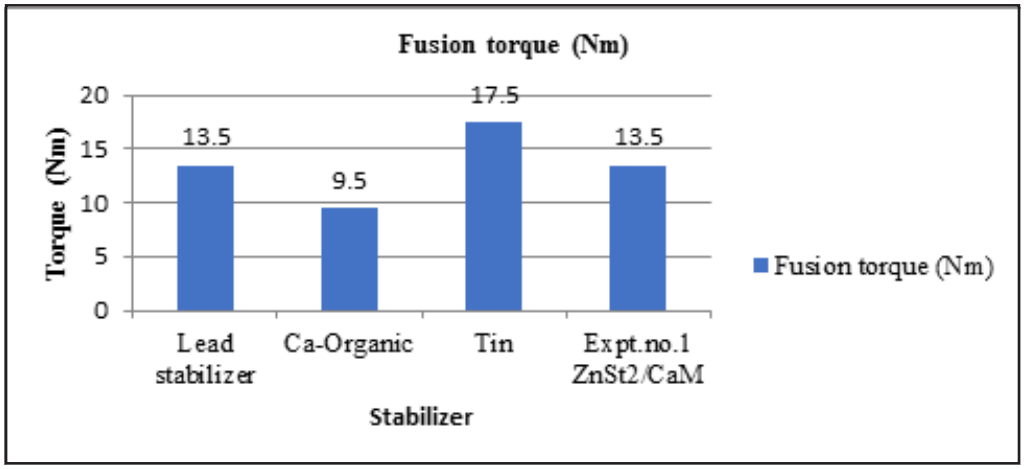

Fig 9. Fusion torque of commercial and experimental stabilizers

Tin stabilizer has higher torque which consumes more energy during process, but has long-term stability. Organotin mercaptides are a very effective and universally applicable group of tin stabilizers. Though the fusion torque is high and fusion time is early, its stability efficiency is more than other stabilizers even at low phr dosage. Tin stabilizer binds the HCl which is released during process. They substitute unstable chlorine atoms in the polymer chain and prevent further degradation of the PVC. Lead stabilizers have fusion time 3.3 min which give sufficient time for proper mixing, though the initial color is not as good as tin stabilizer, it holds the color till the end and changes very gradually. While the experimental stabilizer which is a combination of Zinc stearate and Calcium metilox with other assisting additives show good rheology as compared to tin stabilizer. Gelation time is early but fusion torque is not high compared to tin.

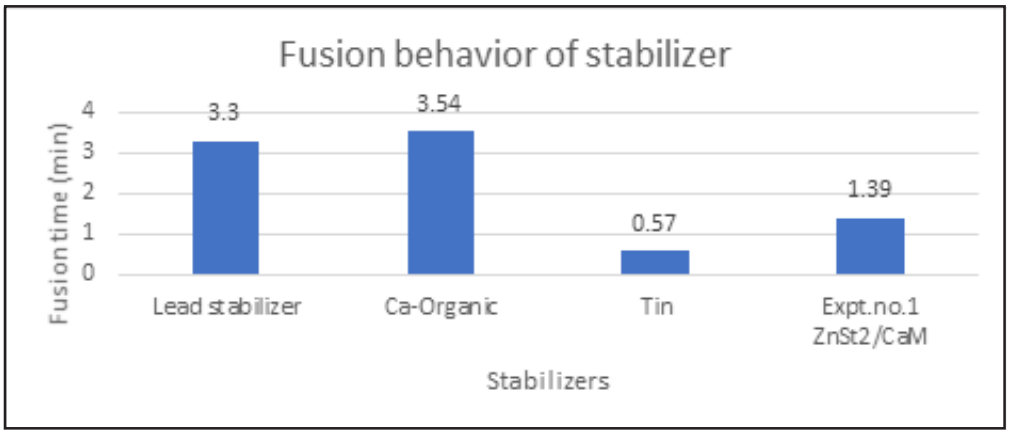

Fig 10. Fusion behaviour of Stabilizers

Torque Rheology study of Stabilizer

The effect of calcium stearate and calcium metilox salts on rheology of stabilizers have been studied. The stability of prepared selective stabilizer (contents of calcium salt of metilox acid) was evaluated on Brabender plasticodore PL2000. Fusion torque, time and thermal stability studies were carried out for stabilizers. ZnL with CaM and calcium stearate demonstrates fast gelation, fusion torque 15 Nm and short stability as compared with other stabilizers. This is the effect of calcium stearate which promotes early fusion but further stabilizers shortened the stability time. Calcium metilox and zinc stearate has fusion torque 12.5 Nm Ca-Organic stabilizer has weak stability compared to other.

Conclusions

In response to removal of lead stabilizer, the new one pack stabilizer with novel compound Calcium salt of metilox acid has better thermal stability than commercial lead stabilizer and retards effectively the degradation during process.

References

1. Chen, G.M., 2007, *J. Appl. Polym. Sci.*, **106**, 817–820.
2. Folarin, O.M. and Sadiku, E. R., 2011, *A Review, International Journal of Materials Science.*, **6,** 4323-4330.
3. Tawfik S.Y., Asaad J.N. and Sabaa M.W., 2006, *Polym Degrad stab,* **91(2),** 385-392.
4. Stranes W.H. Jr., 2005, *J. Polym. Sci. Part. A Polychem*, **43,** 2451-2467.
5. Stranes W.H. Jr., 2002, *Prog Poym Sci.*, 2133-2170.

6. Murphy, J., 1999, *Plastic. Add. Compound.,* **1,** 24-29.

7. Sabaa M.W. and Mohamed R.R., 2007, *Polym Degrad stab.*, **92(4),** 587-595.

8. Yang, Z.H., Shu, W.Y., Long, H.Z., Li and X.H., 1999, *Chin. Rare Earths*, **20,** 60-62.

9. Steenwijk J., Langerock R., Vanes D.S., Haveren J.V., Geus J.W., 2006, *Polym Degrad Stab.*, **91,** 52-9.

10. Lin Y.J., Wang J.R., Evans D.G. and Li D.Q., 2006, *J Phys Chem Solids*; **67,** 998-1001.

11. Vaccari, A., *Catal, Today*, **41,** 53-71.

12. Vaccari, 1999, *Appl, Clay Sci.,* **14,** 161-198.

13. Van der Ven, L., Van Gemert, M.L.M., Batenburg, L.F., Keern, J.J., Gielgens, L.H., Koster, T.P.M. and Fischer, H.R., 2000, *Appl. Clay Sci.*, **17,** 25-34.

14. Xu SL, Li DG, and Yu XJ., 2012, *J. Appl Polym Sci.*, **126(2),** 569-574.

15. Abbas K.B. and Sorvik E., 1980, *J. Vinyl Additives Technol*, **2,** 87–94.

16. Manzoor, W., Yousaf S.M. and Ahmad, Z., 1996, *Polym. Degrad. Sta.*, **51,** 295.

17. Xiaopeng Xu., Si Chen, Bozhen Wu., Meng Ma., Yangin Shi. and Xu Wang., 2015, *J. Therm Anal Calorin*, **119,** 597-603.

18. Mengliang Tong., Hongyan Chen., Zhanhong Yang and Runjuan Wen, *International Journal of Molecular Sciences*, ISSN 1422-0067.

19. Vrandecic N., Stipanelov, Klaric I. and Roje U., 2001, *Polym Degrad Stab.*, **74,** 203–211.

20. Steenwijk J., Langerock R., van Es DS., van Haveren J., Geus JW. and Jenneskens LW., 2006, *Polym Degrad Stab.*, **91(1),** 52-59.

21. Wang M., Xu JY., Wu H. and Guo SY., 2006, *Polym Degrad Stab.,* **91(9),** 2101-2109.

22. Michel A., Van Hoang T., Perrin B. and Llauro MF., 1981, *Polym Degrad Stab.*, **3(2),** 107-119.

23. Benavides R., Edge M., Allen NS., Mellor M., Harvey H. and Schmets G., 1996, *Polym Degrad Stab* **53(3),** 311-318.

RNI No. MAHENG/2017/74063
ISSN No. (Print) 2581-5911
ISI Impact Factor 0.883 (2018)

Degradation of Pollutant Dye in Aqueous Solution using Fenton Reaction: A DFT Study

A. Jaafar [1], H. Ben El Ayouchia [2], Z. Lakbaibi [3,4], A. Boussaoud [1], S. Jodeh [5,], K. Azzaoui [6] and Mohamed Tabyaoui [4]

[1] Laboratory of Process, Signals, Industrial Systems, Computer Science, Superior School of Technology, Cadi Ayyad University, Dar Si-Aïssa Road, 46000, BP 89, Safi, Morocco

[2] Laboratory of Analytical and Molecular Chemistry, Polydisciplinary Faculty of Safi, Cadi Ayyad University, Safi, 46030, Morocco

[3]Department of Chemistry, Faculty of Sciences and Techniques, Moulay Ismail University, Errachidia, Morocco

[4] Laboratory of Materials, Nanoparticles and Environment, University of Mohammed V Faculty of Sciences, BP 1014, Ibn Batouta Avenue, Rabat Morocco

[5] Laboratory of Solid Minerals and Analytical Chemistry, Faculty of Sciences, Mohamed Premier University, P.O. Box 717, 60000, Oujda, Morocco

[6] Department of Chemistry, An-Najah National University, P.O. Box 7, Nablus, Palestine

E-mail: sjodeh@hotmail.com; jaafarfstgm@gmail.com

Abstract

The degradation reaction of Neutral Red dye (NR) by ˙OH radical (Fenton reaction) is one of the most important processes to remove this pollutant dye from wastewater. However, quantum calculations based on the density functional theory (DFT) and electron localization function have recently emerged as greener pathways to study the degradation behaviour of pollutant dyes that exist in wastewater. Furthermore, an exploration of DFT and ELF calculations provide useful information regarding orientation of degradation reaction between NR dye and ˙OH radical. Indeed, the conceptual DFT (CDFT) indices of reagents demonstrate strongly that the ˙OH radical is an electron-acceptor and that the NR dye is an electron-donor. On the other hand, the nitrogen atom N20 is the most nucleophilic site of NR dye, while the most electrophilic site of ˙OH radical is the oxygen atom. Therefore, an ELF study of the electronic structure of NR dye demonstrates that this dye has a pseudoradical electronic structure. Consequently, the first step of the reaction between NR dye and ˙OH was proposed. Additionally, determination of spectroscopic spectra (Fourier-transform infrared (FT-IR) and UV-Visible) of NR dye confirms a good correlation between theoretical and experimental spectra.

Keywords: *Fenton reaction, ˙OH radical, Neutral Red dye, DFT, ELF.*

Introduction

Water pollution occurs when unwanted materials enter into water and influence the quality of water and are thus harmful to environment and human health. The machinery and modern dyeing processes in the textile sector are designed for using synthetic dyes. Dye-containing wastewater discharged from industry is a serious threat to the receiving water bodies around the industrial areas [23] because these toxic organic dyes can affect plant life and thus destroy the entire ecosystem [41]. To avoid the environmental disaster due to the toxic chemical dyes, efficient and low-cost methods must be developed to clean the industrial wastewater.

Neutral Red (NR) is an important colouring agent [31]. It is often used as a linsey-woolsey colouring agent, biological stain and acid-base indicator. Therefore, Neutral Red is an important component in dyeing wastewater.

Fenton reaction ($Fe^{2+} + H_2O_2 + H^+ \rightarrow Fe^{3+} + {}^{\bullet}OH + H_2O$) is an effective and low-cost method for the treatment of aqueous solution containing a NR dye [24,25]. However, the mechanism of this reaction between NR dye and ${}^{\bullet}OH$ radical (degradation of NR dye in aqueous solution using Fenton reaction) is not studied. Nevertheless, the efficiency of the Fenton process is strongly dependent on pH; the optimum pH value is around 3. [24] In this system, the free radicals (${}^{\bullet}OH$) which are responsible for the degradation of organic pollutants into biodegradable compounds undergo complete mineralization into CO_2, H_2O and inorganic ions [10, 44].

In recent years, researchers have been using computation methods for molecular structure description, spectroscopic properties and molecular reactivity. Density functional theory (DFT) which is one of these methods has been widely used in literature because of its efficiency and accuracy with respect to the evaluation of several molecular properties [1,6,7,29,30]. The greenness of these theoretical techniques lies in the fact that they do not require use or discharge of any environmentally hazardous chemicals into the surrounding environment unlike experimental techniques.

In this work, to describe the reaction between NR dye and ${}^{\bullet}OH$ radical, optimisation of the structure of NR dye, determination of its spectroscopic properties (Fourier-transform infrared (FT-IR) and UV-Visible), and determination of global and local reactivity descriptors (such as chemical hardness (η), chemical potential (μ), global electrophilicity (ω), global nucleophilicity (N), local electrophilicity ω_k and the local nucleophilicity N_k indices) of NR dye and ${}^{\bullet}OH$ radical were investigated using the DFT method. Indeed, the electron localisation function (ELF) was established. On the other hand, the bond order was investigated. Finally, the comparison of the theoretical IR and UV spectra with the experimental spectra was carried out.

Materials and Methods

Neutral red dye of analytical grade was purchased from REACTIFS RAL. It has molecular formula $C_{15}H_{17}ClN_4$ (FW =288.8 g/mol) with colour index Number 50040. Water used throughout was distilled water.

The FT-IR spectrum of the neutral red dye was recorded in the 4000-400 cm^{-1} region with BRUKER spectrophotometer using KBr pellet. The Ultraviolet absorption spectrum was examined in the range 200-800 nm using a UV-vis spectrophotometer (Rayleigh UV-1800) with a spectrometric quartz cell (1 cm path length) in water solvent at acidic conditions.

Computational details

The calculations were performed using Gaussian 09 package[18,39] and displayed with Gauss View.[9] Optimized geometrical parameters and vibrational frequencies for the compounds were calculated using DFT with the B3LYP (Three parameter (local, non-local, Hartree-Fock) hybrid exchange functional (B3), with Lee-Yang-Parr correlation functional (LYP)) [4,5], together with the 6–31+G(d,p) basis set. Then, the ELF study [5] was carried with the TopMod program [33,40].

Solvent effects of water were considered by single-point energy calculations using the conductor-like polarizable

continuum model (CPCM) developed by Tomasi's group [22,43]. The UV-Vis absorption in water was simulated by using Time-Dependent density functional theory (TD-DFT [34,36]) employing B3LYP /6-31+G(d,p).

For the neutral red dye, the global electrophilicity index value (ω) [35] was determined by using the following equation, $\omega=(\mu^2/2\eta)$, where $\mu\sim(E_{HOMO}+E_{LUMO})/2$ is the chemical potential, and $\eta=(E_{LUMO}-E_{HOMO})$ is the chemical hardness [12]. The empirical (relative) nucleophilicity index N [13,14,28], based on the HOMO energies obtained within the Kohn–Sham scheme [15], was determined as $N = E_{HOMO}(Nu) - E_{HOMO}$(TCE), where TCE (tetracyano-ethylene) is the reference, because it has the lowest E_{HOMO}. Besides the global electrophilicity and the global nucleophilicity indices, it is possible to define its local (or regional) counterpart condensed to atoms. The local electrophilicity, $\omega_k = \omega P_k^-$, or the local nucleophilicity $N_k = N P_k^-$, condensed to atom k is easily obtained by projecting the global quantity onto any atomic center k in the molecule by using the Parr functions. The electrophilic P^+_k and the nucleophilic, P^-_k, Parr functions, were determined by using the Mulliken Atomic Spin Density (ASD) analysis [16] of the radical anion and the radical cation by single-point energy calculations over the optimized neutral geometry using the unrestricted UB3LYP formalism for radical species.

For the ·OH radical, chemical hardness (η°), chemical potential (μ°), global electrophilicity (ω°) were calculated by the following equations : $\eta^\circ=(E^{\beta,\circ}_{LUMO}-E^{\alpha,\circ}_{HOMO})$, $\mu^\circ=(E^{\alpha,\circ}_{HOMO} + E^{\beta,\circ}_{LUMO})/2$, and $\omega^\circ=\mu^{\circ 2}/2\eta^\circ$ [36] where $E^{\alpha,\circ}_{HOMO}$ is the energy of one electron in α spin state of the frontier molecular orbital HOMO and $E^{\beta,\circ}_{LUMO}$ is the energy of one electron in β spin state of the frontier molecular orbital LUMO. In addition, the global nucleophilicity N° [14] of the radical species is given as: $N^\circ= E^{\alpha,\circ}_{HOMO}$ *(radical)* $- E^{\alpha,\circ}_{HOMO}$(DCM), where DCM is dicyanomethyl radical ($(^\cdot CH(CN)_2$) applied as a reference radical because it leads to positive scale of global nucleophilicity of radicals. For the local reactivity indices, Domingo *et al*. [16] have defined the local electrophilicity $\omega^\circ_{(k)}$ and the local nucleophilicity $N^\circ_{(k)}$ for the neutral radicals species according to the following equations: $\omega^\circ_{(k)}=\omega^\circ P^\circ_k$ and $N^\circ_{(k)} = N^\circ P^\circ_k$, where P°_k is the atomic spin density at atom k of the neutral radical specie.

On the other hand, to study the *pseudoradical* (*pr*) reactivity of NR, the *pr* index has recently been defined as $pr=N/\eta$ where η *is the* chemical hardness and N is the nucleophilicity index of the NR dye [16,37].

Results and Discussion

ELF analysis of NR dye at the ground state electronic structure

An attractive procedure that has given us a direct link between the distribution of electron density and the chemical structure is the quantum chemical topological analysis of ELF established by Becke and Edgecombe [5]. It has become a powerful tool for the study of the bonding changes along an organic reaction. Within the context of ELF, monosynaptic basins V(X) are corresponding to non-bonding regions, while disynaptic basins V(X,Y) are related to bonding regions [32]. The reactivity of NR can be correlated with its electronic structure; consequently, first an ELF topological analysis of NR was performed. The representation of ELF valence attractor positions together with corresponding populations and proposed Lewis structure for NR at the ground state optimised geometry is shown in Figure 1.

As presented in Figure 1, the ELF topology of NR indicates the presence of the following basins: one V(N) monosynaptic basin located at the N20 nitrogen, integrating a total of 2.67e which evidently portrays a *pseudoradical* center over N20 nitrogen atom [3]. For nitrogen atoms N18, N22 and N21, two monosynaptic basin were found for each, V(N18), V2 (N18), V(N22), V2 (N22), V(N21) and V2 (N21), integrating a total electron population of 1.48e, 1.78e and 1.44e, respectively. The C5-C6, C8-C9 and C11-C12 bonding region is characterized with the presence of one V(C5,C6), V(C8,C9) and V(C12,C13) disynaptic basin integrating 3.24e, 3.36e and 3.26e respectively, a values which is close to 4e, indicating a double C5-C6, C8-C9 and C12-C13 bonding.

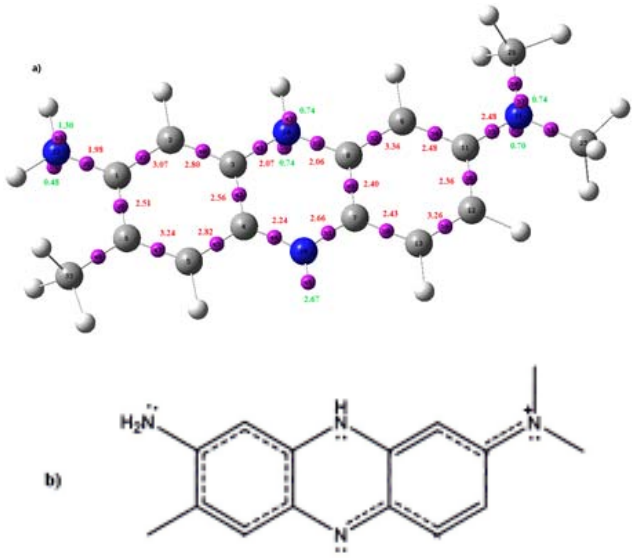

Bond Order

Bond order [42] was calculated for further explanation. Bond order [20] is an electronic parameter related to the electron density among atoms. The values of bond order were obtained from a natural population analysis [19] and provide an indication of the bond strength. A large positive value of bond order indicates strong bonding between the atoms of the molecular entity [17]. Bond order values are shown in Figure 2. It appears from these values that the strong bonding is between 12(C) and13(C) then 5(C) and 6(C). The values are 1.64 and 1.59 respectively. The weak CC and CN bonding is between 6(C) and 33(C) and between 21 (N) and 25(C), 29(C), respectively. The values are 1.04 and 0.95 respectively.

Fig 1. Representation of ELF valence attractor positions together with corresponding populations (values in e) disynaptic basins V(X,Y) values (in red) monosynaptic V(X) values (in green) (a), and proposed Lewis structure (b) of NR dye.

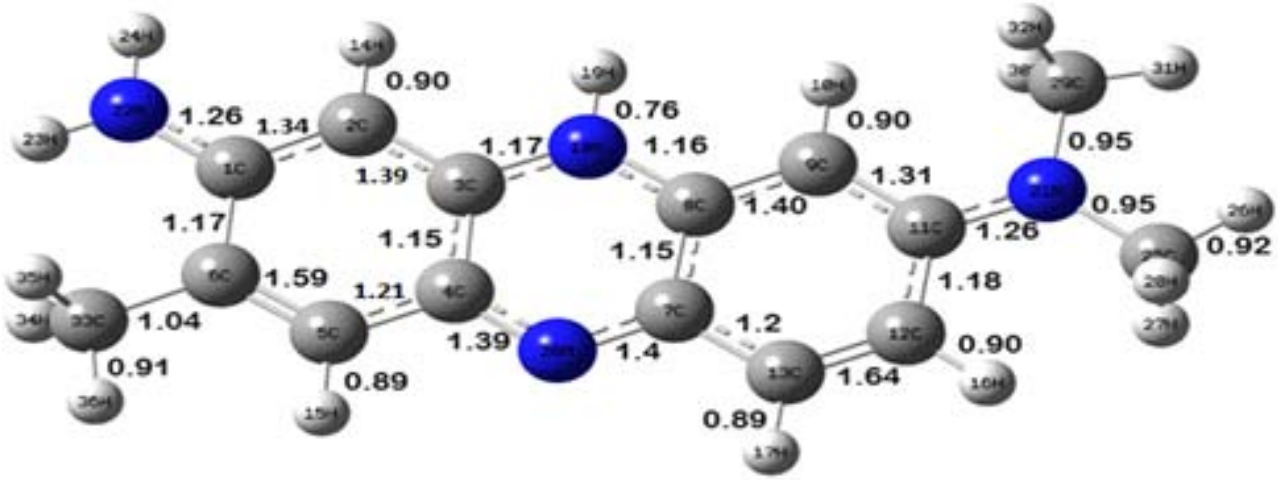

Fig 2. Bond order values

Global electrophilicity/nucleophilicity indices analysis

Numerous works devoted to chemical reactions have proved that the analysis of the reactivity indices defined within the conceptual DFT (CDFT) [8,30] is an efficiency method to explain the reactivity of the reagents involved in organic reaction. Consequently, the global CDFT indices, namely, the chemical hardness, η, electronic chemical potential, μ, global electrophilicity, ω, global nucleophilicity, N and *pseudoradical* index, *pr* of NR and $^{\bullet}$OH radical are reported in Table 1.

Table 1. E_{HOMO} and E_{LUMO} energies (eV), chemical potential *μ* (eV), chemical hardness *h* (eV), global electrophilicity *w* (eV), global nucleophilicity *N* (eV) and *pseudoradical index* of the NR dye and •OH radical.

	E_{HOMO}	E_{LUMO}	μ	η	ω	N	*pr*
NR dye	-5.89	-3.18	-4.53	2.71	3.80	3.10	1.10
•OH radical	-9.74	-5.06	-7.40	4.67	5.87	-	-

Chemical hardness η is associated with the stability and reactivity of a chemical system. In a molecule, it measures the resistance to change in the electron distribution or charge transfer. Electronic chemical potential μ is defined as the negative of electronegativity of a molecule. Physically, μ describes the escaping tendency of electrons from an equilibrium system. Therefore, the global electrophilicity index ω measures the propensity or capacity of a species to accept electrons.

From Table 1, the electronic chemical potential of NR, μ= -4.53 eV is higher than that of •OH radical, μ= -7.40 eV. This means that •OH radical is an electron-acceptor however NR dye is an electron-donor. This means that the NR dye would probably be the favourite entity for electrophilic attacks. Indeed, the electrophilicity index for NR is 3.80 eV and for •OH radical is 5.87 eV. When two molecules react, which one will act as an electrophile (nucleophile) will depend upon higher (lower) value of electrophilicity index. This result confirmed that RN is an electron donor and the •OH radical is an electron acceptor.

On the other hand, NR dye presents high *pr* value, 1.10 (Table 1) in clear agreement with its *pseudoradical* character of nitrogen atom 20 (N), which has a single monosynaptic basin as revealed by the topological analysis of the ELF (see Figure 1).

Local electrophilicity/nucleophilicity indices analysis

In order, to predict the regioselectivity in radical reaction, we have used the electrophilic P_k^+ and nucleophilic P_k^- Parr functions. [16]

The region-chemistry depends in reliability to the electron density distribution at the reactive sites between a separate electrophilic entity and nucleophilic entity involved in the reaction, as given in Figure 3. The calculated nucleophilic P_k^- Parr function at the reactive sites of NR indicates that the N20 nitrogen atom has higher value (0.40) compared with that of nitrogen atoms N18, N21 and N22, which have 0.11, 0,05 and 0.05, respectively, indicating N20 atom is the most nucleophilic center at NR. This result shows that the N20 atom will be considered more activated site towards an electrophilic attack. The other atoms of NR dye (carbon and hydrogen) appear low reactive compared to the nitrogen atoms (all results are presented as supplemental data (Tables S1, S2)). Indeed, the radical Parr function P^o_k of the •OH radical reveals that the oxygen atom O is the most electrophilic center, with a P^o_k value of 1.00 (Figure 3).

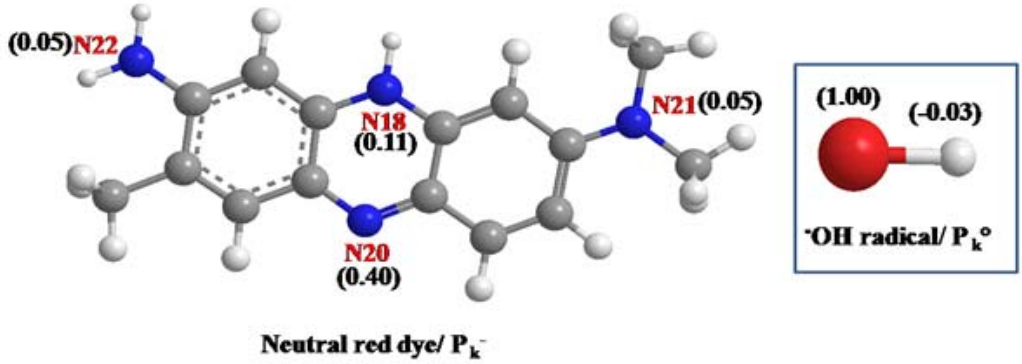

Fig 3. Electrophilic and nucleophilic Parr functions of reagents values (in eV). The most significant centers are considered.

Consequently, the most favourable initial nucleophile/electrophile free radical interaction will occur between the most nucleophilic center of NR, the N21 nitrogen, and the most electrophilic center of ·OH radical, the O oxygen, leading to intermediate **P1**, which has the largest nucleophilic activation at the C11 carbon. Consequently, formation of the second single bond will take place through the nucleophilic attack of the C11 carbon of the NR on the O oxygen of the ·OH radical, leading to intermediate **P2** (Figure 4).

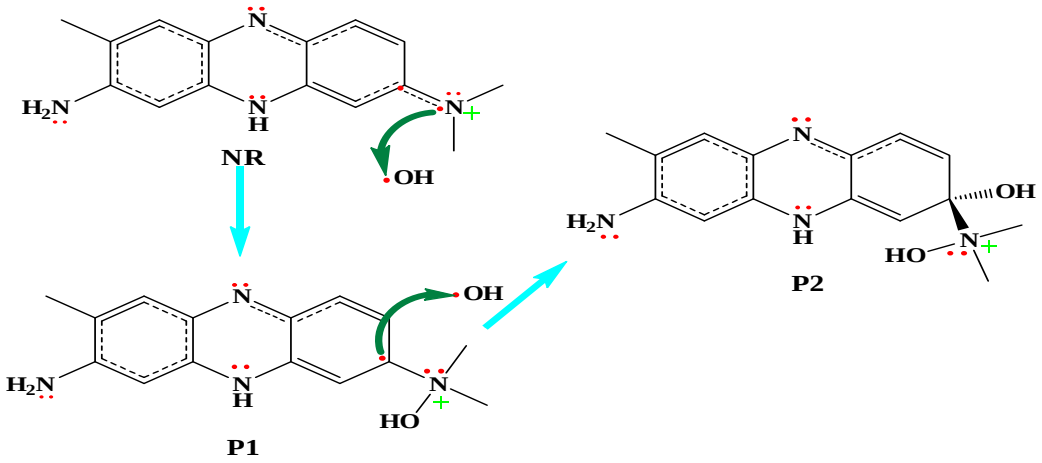

Fig 4. First step proposed for reaction between NR dye and ·OH radical.

IR and UV-vis spectra of neutral red dye

From the theoretical point of view, the UV-vis spectra of neutral red dye out carried by using TD-DFT [34,40b] method at B3LYP/6-31+G(d, p) level. The experimental and theoretical UV-vis spectra are illustrated in Figure 5. One can note that there are two bands observed at 530 nm which can be attributed to the absorption of the n→π* transitions of N=C, and 272 nm ascribed to the π→π* transitions representing of ring system, in experimental spectra (see Figure 5). These bands are calculated at 528 nm and 270 nm which show a good agreement. The difference between the λ_{max} for both spectra is only about 2 nm. This allowed us to say that the DFT analysis of the UV-vis spectrum could be an alternative to the experimental analysis.

Figure 6 shows theoretical and experimental IR spectra of neutral red dye. In the present theoretical study, the IR bands at 3201.32, 3209.64, 3239.41, 3252.71 cm^{-1} are assigned to C-H stretching vibrations for benzene ring. Experimentally, the C-H stretching vibrations are observed at 3202 cm^{-1}. The N_{22}-H and N_{18}-H symmetrical stretching vibrations are observed at 3625 cm^{-1} of the experimental IR spectrum. These bands are calculated at 3614.87 and 3576.65 cm^{-1} respectively (Table 2). However, the C_{29}-H, C_{25}-H, and C_{33}-H stretching band is observed at 3020 cm^{-1} for the experimental IR spectrum. This band is calculated at 3032.16 cm^{-1}.

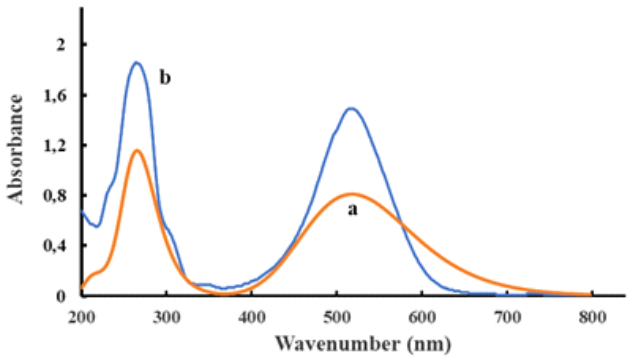

Fig 5. Comparison of the absorption spectra determined theoretically based on the TD-DFT using B3LYP/6-31+G(d,p) level (a) and experimentally (b) for NR dye.

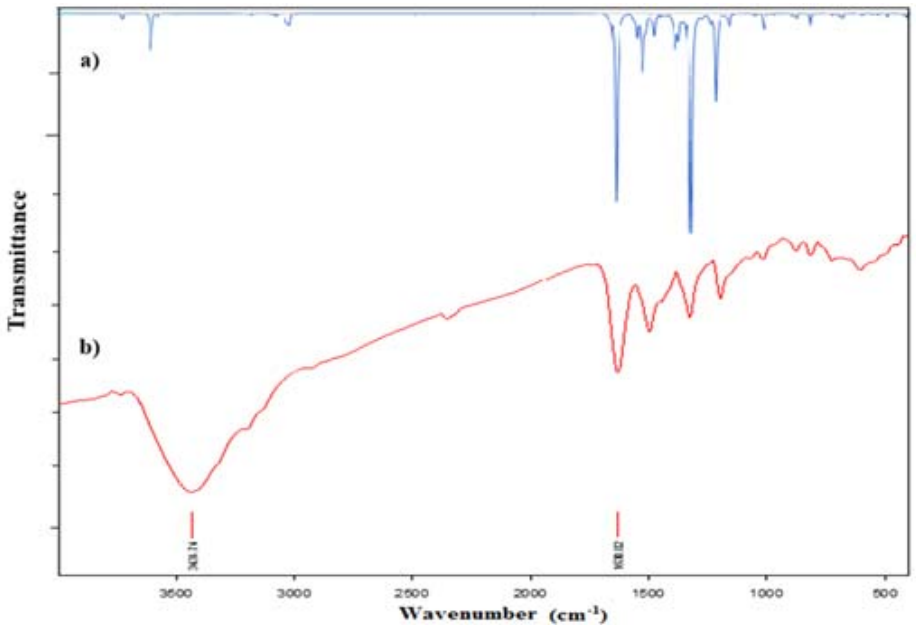

Fig 6. Theoretical (a) and experimental (b) IR spectra of neutral red dye.

Table 2. Some vibrational frequencies (in cm^{-1}) of neutral red dye using the experimental and using ground state-DFT/ B3LYP/6-31+G(d, p).

Experimental	Theoretical	Approximate description [a]
-	1684.60	$\upsilon_{C=C\ (aromatic\ )}$
-	3738.82	$\upsilon_{N_{22}-H\ (asym.)(aromatic\ \ primary\ \ amine\ )}$
3600	3614.87	$\upsilon_{N_{22}-H\ (sym.)(aromatic\ \ primary\ \ amine\ )}$
3600	3576.65	$\upsilon_{N_{18}-H}$
3020	3032.61	υ_{CH_3}
-	1664.35	$\beta_{NH\ (Sciss.)}$
1630.82	1635.65	$\beta_{N_{18}-H}$
725	711.56	$\gamma_{N_{18}-H\ (Twis.)}$
1468	1485.95	$\beta_{CH_3\ \ (Sciss.)}$

[a]υ, stretching; β, in-plane deformation; γ, out-of-plane deformation; (sciss), scissoring; (twis), twisting ; (sym), symmetrical; (asym), asymmetrical.

Conclusions

We have carried out DFT-B3LYP calculation on the structure, UV-visible and FT-IR spectra of NR dye at 6-31+G(d,p) level. A good agreement was found between the computed and experimental wavenumbers. This confirms the validity of the calculation methods used. Therefore, applying global reactivity indices derived from DFT, we have demonstrated that the NR dye has an electron donor behaviour and the •OH radical has an electron acceptor behaviour. Moreover, by using Parr functions we have noted that the local attack is between nitrogen atom N(21) of NR dye and oxygen atom of •OH radical. The ELF topological analysis of the struc-

ture of NR indicates that this dye has a *pseudoradical* electronic structure.

References

1. Al-Sehemi A.G., Irfan A, Aljubiri, S.M. and Shaker, K.H., 2016, *Journal of Saudi Chemical Society*., **20**, S21-S28.

2. Averill, B. and Eldredge P., 2011, General Chemistry: principles patterns and applications.

3. Becke A.D., 1993, *J. Chem. Phys*., **98,** 5648-5652.

4. Becke A.D. and Edgecombe K.E., 1990, *J. Chem Phys.,* **92,** 5397-5403.

5. Ben El-Ayouchia H., Bahsis L., Anane H., Domingo L.R. and Stiriba SE 2018, *RSC Adv.,* **8,** 7670-7678.

6. Ben El-Ayouchia H., Bahsis L., Anane H., Gutiérrez MR., Domingo L.R. and Stiriba S.E., 2018b, *Chemistry Select.,* **3,** 1215-1223.

7. Chattaraj P.K. and Maiti B., 2003, *J. Am. Chem. Soc*., **125,** 2705.

8. Dennington R.D., Keith D.T. Millam T.J. and Gauss J., 2009, Version 5. Semichem Inc. Shawnee. Mission. KS.

9. Dias I., Souza B., Pereira J., Moreira F., Dezotti M. Boaventura A. and Vilar V. 2014, *Chemical Engineering J.,* **247,** 302-313.

10. Domingo L.R., Chamorro E. and Pérez P., 2010, *Lett. Org. Chem*., **7,** 432.

11. Domingo L.R., Chamorro E. and Pérez P., 2008, *J. Org Chem.,* **73,** 4615-4624.

12. Domingo L.R. and Pérez P., 2011, *Org Biomol Chem.,* **9,** 7168-7175.

13. Domingo L.R., Pérez P. and Sáez J.A., 2013, *RSC Adv.,* **3,** 1486-1494.

14. Domingo L.R. and Emamian S.R., 2014, *Tetrahedron,* **70,** 1267.

15. Domingo L.R. and Gutiérrez M.R., 2017, *Molecules.,* **22,** 750.

16. Domingo L.R. Gutérrez M.R. and Pérez P., 2016, *Molecules,* **21,** 748-769.

17. Frisch M.F., et *al*., 2009, Gaussian 09. revision A.02. Gaussian Inc. Wallingford.

18. Geerlings P., Proft F.D. and Langenaeker W., 2003, *Chem. Rev.,* **103,** 1793-1874.

19. Glendening E.D., Landis C.R. and Weinhold F., 2013, *J. Comput. Chem.,* **34,** 1429-1437.

20. Glendening E.D. and Weinhold F., 1986, *J. Comput. Chem*., **19,** 610-627.

21. Gross EKU and Kohn W., 1990, *Adv Quant Chem.,* **21,** 255-291.

22. Hameed B.H., 2009, *J. Hazard. Mater.,* **162,** 344-350.

23. Jaafar A. and Boussaoud A., 2014, *J. Materials. Environmental Science.,* **5,** 2426-2431.

24. Jaafar A., Driouich A., Lakbaibi Z., Ben El Ayouchia H., Azzaoui A., Boussaoud A. and Jodeh S., 2019, *Desalination and Water Treatment,* **158,** 364–371.

25. Jaafar A, Boussaoud A, Azzaoui K, Mejdoubi E, Chetouani A, Hammouti B, Lamhamdi A, and Berrabah M., 2016, *Mor. J. Chem.,* **4,** 759-763.

26. Jaafar A, Boussaoud A, Jodeh S, Azzaoui K, Hamed O, Salghi R, Hanbali G, Hasan AR, and B. Khalaf B., 2016c, *Der Pharma Chemica*., **8,** 345-349.

27. Kohn W. and Sham L., 1965, *J Phys Rev.,* **140,** 1133-1138.

28. Lakbaibi Z, El-Makarim HA, Tabyaoui M. and El-Hajbi A., 2016, *Mor. J. Chem.,* **4,** 437-453.

29. Lakbaibi Z, Jaafar A, Ben El Ayouchia H, Tabyaoui M. and Boussaoud A., 2019, *Mediterr. J. Chem.*, **8,** 25-29.

30. Liu XH, Deng Y, Zhou YH, Xia L, Ding LL. and Zhang Y.C., 2012, *World Journal of Nuclear Science and Technology,* **2,** 133-137.

31. Nic M, Jirat J. and Kosata B., 2012, Compendium of Chemical Terminology (Gold Book), International Union of Pure and Applied Chemistry.

32. Noury S, Krokidis X, Fuster F. and Silvi B., 1999, *Comput. Chem.,* **23,** 597.

33. Parr RG, Szentpaly LV. and Liu S., 1999, *J. Am Chem Soc.,* **121,** 1922-1924.

34. Parr RG. and Pearson RG., 1983, *J. Am. Chem Soc.,* **105,** 7512-7514.

35. Parr RG and Yang W., 1989, Density functional theory of atoms and molecules, Oxford University Press. New York.

36. Silvi B., 2002, *J. Mol. Struct.,* **614,** 3-8.

37. Simkin BY. And Sheikhet I., 1995, Quantum chemical and statistical theory of solutions computational approach, Ellis Horwood, London.

38. Sun YX, Hao QL, Lu LD, Wang X. and Yang XJ., 2010, *Spectrochim. Acta A.,* **75,** 203-211.

39. Tomasi J. and Persico M., 1994, *Chem Rev.,* **94,** 2027-2094.

40. Vektariene A, G. Vektaris and Svoboda J., 2009, *ARKIVOC.,* **7,** 311.

41. Wang SB, Zhu ZH, Coomes A, Haghseresht F. and Lu GQ., 2005, *J. Colloid Interface Sci.,* **284,** 440-446.

42. Wiberg KB., 1968, *Tetrahedron.,* **24,** 1083-1096.

43. Yanai T, Tew DP. and Handy NC., 2004, *Chem. Phys Lett.,* **393,** 51-57.

44. Yee LH, V. Aagaard V, Johnstone A, Lee M, Kjelleberg SJ. and Manefield M., 2010, *Biodegradation.,* **21,** 947–956.

RNI No. MAHENG/2017/74063
ISSN No. (Print) 2581-5911
ISI Impact Factor 0.883 (2018)

Chlorogenic Acid Assisted Green Synthesis of Silver and Gold Nanoparticles and their Applications

Ridhima Chadha[1*], Disha Kukreja[1], Nandita Maiti [1,2], Abhishek Das [1,2], Anand Ballal[3], and Sudhir Kapoor [1,2*]
[1]Radiation & Photochemistry Division, Bhabha Atomic Research Centre, Trombay, Mumbai 400085, India
[2]Homi Bhabha National Institute, Anushaktinagar, Mumbai 400094, India
[3] Molecular Biology Division, Bhabha Atomic Research Centre, Trombay, Mumbai 400085, India
Email: ridhima@barc.gov.in; sudhirk@barc.gov.in

Abstract
We report a facile method to synthesize water soluble Ag and Au nanoparticles (NPs) using chlorogenic acid (CGA), a naturally occurring polyphenol as reducing as well as stabilizing agent. The main emphasis of the work is the methods reported in the literature are mostly done at higher temperature. In the present work, the synthesis is carried out at ambient conditions i.e. at room temperature. The effect of pH and concentration is studied on the formation of NPs. The particles synthesized are characterized using UV-vis spectroscopy and transmission electron microscopy (TEM). The synthesized Ag and Au NPs are tested for their catalytic response towards reduction of o-nitro aniline by sodium borohydride. Au NPs synthesized are also investigated as substrate for surface enhanced Raman spectroscopy (SERS).

Keywords: *Chlorogenic acid, Silver nanoparticles, Gold nanoparticles, Catalysis, SERS*

Introduction

Noble metal nanoparticles (NPs) show many unique properties and one of them is the appearance of surface plasmon resonance (SPR) band in the visible region. This band can be tuned to wider range of wavelength depending on the size and shape of the particles. Noble metal NPs also display intense colors that too depend on the shape and size of the particles[1-3]. For this reason, pre-synthesized metal NPs with and without modification are widely used in analytical chemistry for spectrophotometric determination of metal cations[4–7], anions [8,9] and organic compounds[10–13]. There are various methods reported in literature for the synthesis of NPs. The methods used are top down and bottom up approach. In bottom up approach, they are most often synthesized by chemical reduction method. The most common methods include sodium borohydride or sodium citrate as the reducing agent[1-3, 14-17]. Due to environmental concerns, the use of toxic and hazardous substances which are responsible for various biological risks are being avoided now-a-days. Hence, the new synthetic routes based on green chemistry principles are suggested. The main reason behind this is that the synthesized particles can also

be probed for bio-applications among others. In this respect, bio-compounds as well as plant extracts are seen as a viable route because they contain phenolic moieties which are known to undergo oxidation. Hence, during the past few years various natural products such as biological organisms[18–20] and plant extracts[21–26] have been used as environmentally friendly and safe reducing agents for the synthesis of Ag and Au NPs. Both Ag and Au nanomaterials attract major interest as reflected in numerous literature reports in the field of their methods of preparation, bio-functionalization, and applications in various fields of applications[27-31]. In recent years, the main attention was focused on their use for biosensing, diagnostic immunoassays, and in vivo imaging[32-35]. However, despite an extensive range of practical applications, relatively few experimental works were devoted to systematic studies of Ag and Au NPs preparation using green synthesis at ambient conditions.

Bio-organic moieties containing diol groups attached to the benzene ring have been reported to behave as both reducing and stabilizing agent. Catechol, hydroquinone, resorcinol, n-propyl gallate (n-PG) are some of the phenol derivatives that behaved as reductants for the synthesis of noble metal NPs like Cu, Ag and Au [36-38]. In Asia, the use of herbal medicines is in practice from ancient time. In literature, there are some reports about the use of herbal medicines as reductants for the synthesis of metal NPs [39-41].

Interestingly, as mentioned above most of the plant extracts contain organic compounds that are useful against oxidative stress. Chlorogenic acid (CGA) is a naturally occurring polyphenol which is a biologically important molecule as well since it is an intermediate in lignin biosynthesis. It exists widely in nature because it is a secondary phenolic metabolite in plants. CGA is one of the main polyphenols found in coffee beans, bamboo, peach, apples and onions, as well as many other fruits and vegetables. It is one of the main products responsible for the browning of apples products (fresh-cut apples, apple juices, apple pomace). It is a caffeic acid ester of quinic acid (Scheme-1).

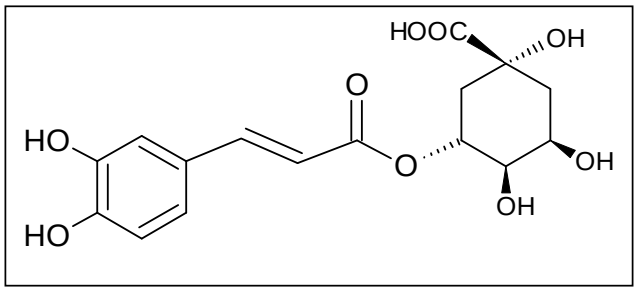

Scheme 1. Structure of chlorogenic acid

It has been reported that CGA acts as an anti-oxidant, anti-inflammatory, antiarthritic, anti-thrombotic [42], anti-diabetic and anti-tumorigenic agent [43,44]. It has also been shown that CGA has chemopreventive properties [45]. Hence, in the present report, CGA is used as a bioreducing agent for the synthesis of Ag NPs and Au NPs. Though, there are reports on the synthesis of Ag and Au NPs using CGA [37,41] but in all the reports, work was carried out at high temperature. In present work, an attempt has been made to synthesize Ag and Au NPs at room temperature. We have shown that CGA not only acts as reductant but also it stabilizes the particles. The experimental conditions such as concentration of metal ions, concentration of reductant, pH of final solution were optimized to get the stable particle dispersions. The synthesized NPs were characterized by using UV-vis spectroscopy, transmission electron microscopy (TEM). The as synthesized particles were tested for their catalytic activity for the reduction of 4-nitrophenol by $NaBH_4$. The particles were also tested as a substrate for the detection of fungicide, crystal violet (CV) using SERS.

Materials and Methods

Materials

Silver nitrate (S.D. Fine Chem. Ltd.), Chlorogenic acid (Sigma-Aldrich), Sodium tetrachloroaurate (III) dihydrate (Sigma- Aldrich), 3,4-dihydroxy mandelic acid (Sigma-Aldrich) were used as received without any further purification. All other reagents were of analytical grade. All aqueous solutions were prepared with Millipore purified water having a resistivity of 18.0 MΩ/cm.

Methods

Synthesis of Ag NPs in presence of CGA was carried out in 10 ml pyrex glass beaker. In each synthesis the same procedure was followed. Stock solutions of $AgNO_3$ (0.01 M) and CGA (0.01M) solutions were prepared. Firstly, the synthesis was done by keeping 1:1 ratio of $AgNO_3$ (0.5mM) and CGA (0.5mM) and varying the pH of the solution with NaOH. After optimization of pH, the synthesis was carried out with different ratios of $AgNO_3$ and CGA at pH ~6.1. After observing the stability of NPs, the concentration of $AgNO_3$ and CGA was kept at 0.5mM in the ratio of 1:1 for further experiments. Similarly, synthesis of Au NPs in presence of CGA was carried out in 10 mL pyrex glass beaker. Stock solutions of $NaAuCl_4$ (0.01M) and CGA (0.01M) solutions were prepared. The synthesis was done by keeping concentration of $NaAuCl_4$ constant at 0.5mM and varying the concentration of CGA. In the synthesis of Au NPs, the pH of the solution was not varied. The particles were found to be stable at 1:1 ratio of $NaAuCl_4$ and CGA.

Synthesized particles were characterized by various techniques. UV-vis absorption spectra were collected on JascoV– 650 spectrophotometer at room temperature using quartz cell. Particle size and distribution was determined by TEM using Zeiss-Carl (Libra-120) instrument. Samples for TEM analysis were prepared by drop casting sample on carbon-coated 200 mesh copper grid and then air-drying of the sample. The mean particle sizes of Ag and Au NPs were determined from image analysis of at least 200 particles of TEM micrographs.

Catalytic activities of the synthesized NPs were checked by a standard catalytic reaction of reduction of o-nitroaniline in presence of sodium borohydride. For the reaction, an aqueous solution containing 2 mL of $1x10^{-4}$M o-nitroaniline (o-NA) was mixed with 1 mL of ice cold 0.1 M sodium borohydride solution followed by the addition of various amounts of NPs in 1cm path length quartz cuvette. The solution was stirred vigorously to avoid diffusion limitation. After the addition of NPs, absorption spectra were collected at various time intervals.

SERS activity of synthesized Au NPs was checked by recording Raman spectra of CV over the surface of Au NPs. For recording the SERS spectra, CV dye solution (6.0/ ×/ $10^{"6/}$ M) was added to the Au NPs solution and mixed well. SERS spectrum was recorded using the 632/ nm He-Ne laser line using a CCD (Synapse, Horiba Jobin Yvon) based monochromator (LabRAM HR800, Horiba Jobin Yvon, France) together with an edge filter, covering a spectral range of 200–1800/ $cm^{"1}$.

Results and Discussion

Synthesis of Ag NPs in presence of CGA

For the synthesis of Ag NPs, $AgNO_3$ ($5x10^{-4}$M) was added to the solution containing CGA ($5x10^{-4}$ M) which showed no change in the color of the solution. Then, the pH of the solution was varied using NaOH which shows a visible change in color from colorless to yellow. The synthesis was carried out at different pH values and their UV-vis absorption spectra were recorded. Figure 1 shows the UV-vis absorption spectra of synthesized Ag NPs at four different pH values (4.9, 6.1, 7.1 and 8.7).

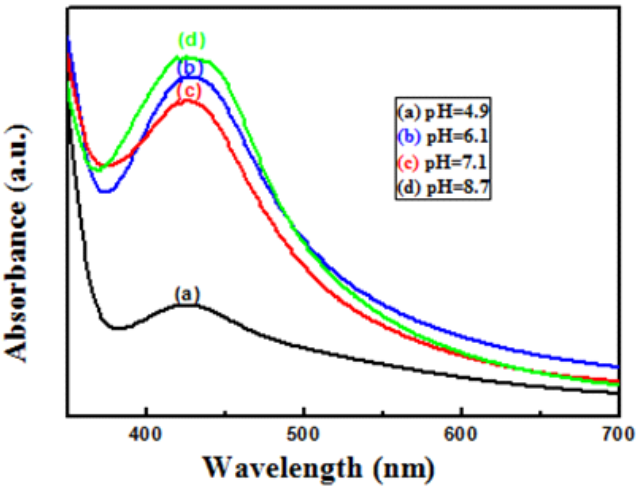

Fig. 1 Variation in the surface plasmon absorption band of Ag NPs synthesized in presence of CGA with change in pH.

The UV-vis spectra of the formed yellow colored Ag NPs showed broad surface plasmon absorption band with maximum at around 425 nm indicating the presence of spherical or roughly spherical Ag NPs. The absorption intensity was found to increase with increase in pH. With time, the yield of particles was found to be same but the width of absorption band at pH 6.1 and 7.1 was narrow with respect to other pH showing uniform distribution of NPs. The stability of the particles was checked by observing the optical absorbance with time. The particles were found to be stable for more than a month. The sequence of addition of reagents was also found to play a vital role. When NaOH was added before the addition of CGA followed by $AgNO_3$, no visible change in color was observed. But, when NaOH was added later after the addition of CGA followed by $AgNO_3$, a visible change in color from colorless to light yellow was observed.

CGA contains two alcoholic groups attached to the benzene ring, one carboxylic group and two alcoholic groups attached to the cyclohexane ring. The pKa_1, pKa_2, pKa_3 values of CGA are 3.36, 8.10, 11.51, respectively [46]. The pKa_1 value corresponds to the carboxylic acid attached to the cyclohexane ring. The pKa_2 and pKa_3 values correspond to the two alcoholic groups attached to the benzene ring. It has been reported that when CGA behaves as reducing agent, it itself undergoes oxidation. The two hydroxy groups attached to the benzene ring get oxidized to the quinone moiety [37]. When the pH of the solution is less than the pKa_2 and pKa_3 values, the two alcoholic groups attached to the benzene ring would remain intact. The only moiety which can undergo ionization is the carboxylic group attached to the cyclohexane ring. The carboxylic group would get ionized and forms carboxylate ion which help to stabilize the nanoparticle. Thus, pH 6.1 was chosen for further experiments. It was observed that at pH 6.1, the Ag NPs were not only stable as well as they had uniform size distribution too.

After optimization of pH, the concentrations of CGA and $AgNO_3$ were optimized by varying the ratio of [CGA]: [$AgNO_3$] by keeping the pH constant at 6.1. After studying the stability of the NPs synthesized at various ratios, the particles synthesized at $5x10^{-4}$ M concentration of each of $AgNO_3$ and CGA in ratio of 1:1 at pH 6.1 were found to be stable as can be seen by UV-vis absorption spectra (Fig. 2).

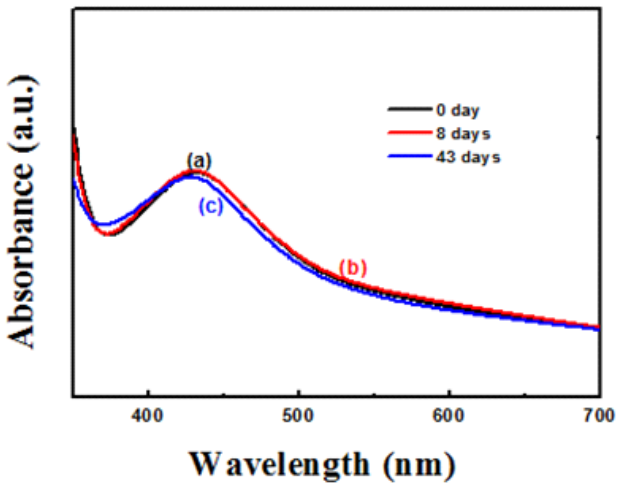

Fig. 2 Variation in the surface plasmon absorption band of Ag NPs with time.

TEM image of particles formed is shown in Figure 3a. As it can be seen from the image, the particles were spherical in shape and individually dispersed with average size of 40±7 nm.

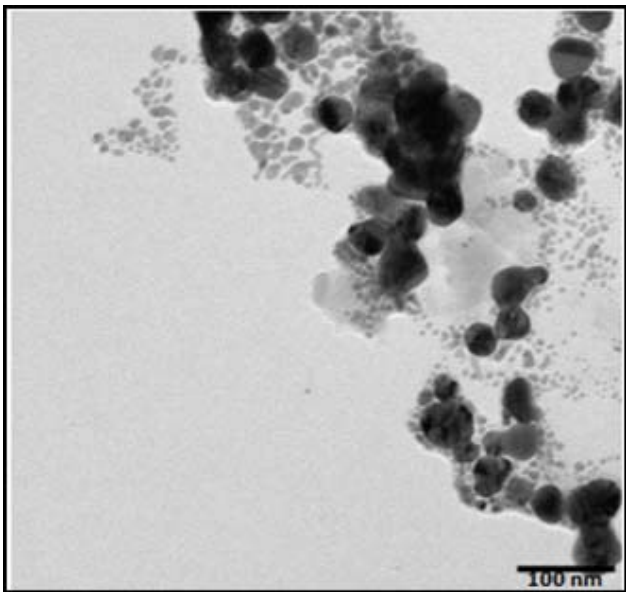

Fig. 3 (a) TEM image of synthesized Ag NPs

The agglomeration which can be seen in the image might have taken place during the sample preparation for TEM. Figure 3b is the histogram depicting the particle size distribution of Ag NPs. It is reported in literature that

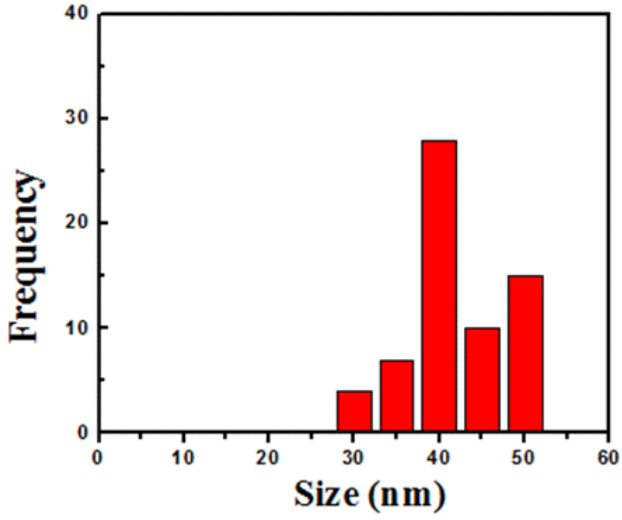

Fig. 3 (b) Size distribution of particles obtained from TEM image in Fig. 3(a)

small molecules with diol moiety like hydroquinone, resorcinol, etc. are not able to stabilize the particles without stabilizer. We have utilized 3, 4-dihydroxy mandelic acid which also contains a catechol moiety as well as carboxylic group to synthesize Ag NPs. There are reports that small acid molecules like mandelic acid helps in directing the assembly of metal NPs.[47] For the synthesis, experimental conditions like pH and concentration of 3, 4-dihydroxy mandelic acid and $AgNO_3$ were optimized. For optimization of pH, $1x10^{-4}$M concentration of both 3, 4-dihydroxy mandelic acid and $AgNO_3$ was chosen. Synthesis was carried out at three different pH values 6.1, 8.0 and 9.1. Slower reduction of silver ions was observed at lower pH value. But when pH was raised from 8.0 to 9.1, increase in absorbance value was observed as shown in Fig. 4. Nanoparticles synthesized at pH 8.00 were found to have good stability.

Synthesis of Au NPs in presence of CGA

For the preparation of Au NPs in presence of CGA, synthesis at various ratios of CGA and $NaAuCl_4$ was

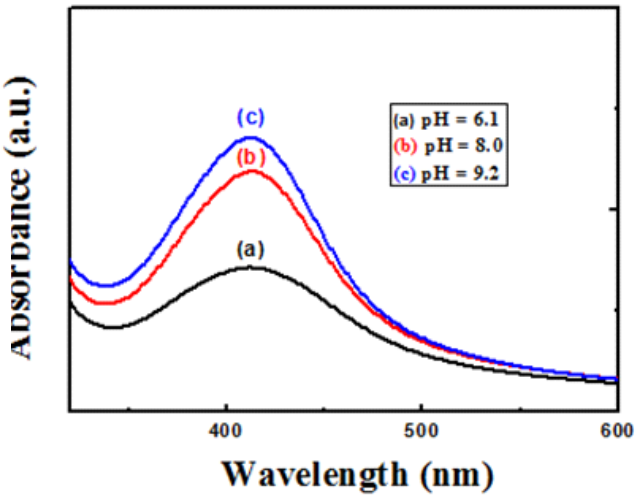

Fig. 4 Variation in the surface plasmon absorption band of Ag NPs synthesized in presence of mandelic acid with change in pH.

carried out. The concentration of $NaAuCl_4$ was kept constant at $5x10^{-4}$ M while concentration of CGA was varied. When $5x10^{-4}$M $NaAuCl_4$ was added to $2.5x10^{-4}$ M CGA, a sudden color change from colorless to reddish pink was observed which turned into pink in the very next day (Fig. 5a). Similar result was observed with $5x10^{-4}$ M CGA (Fig. 5b). When concentration of CGA was further increased to $7.5x10^{-4}$M, NPs started aggregating leading to blue color (Fig 5c). Figure 5 shows the photograph of the Au NPs synthesized with $5x10^{-4}$ M $NaAuCl_4$ in presence of different concentrations of CGA after 24 hours of synthesis.

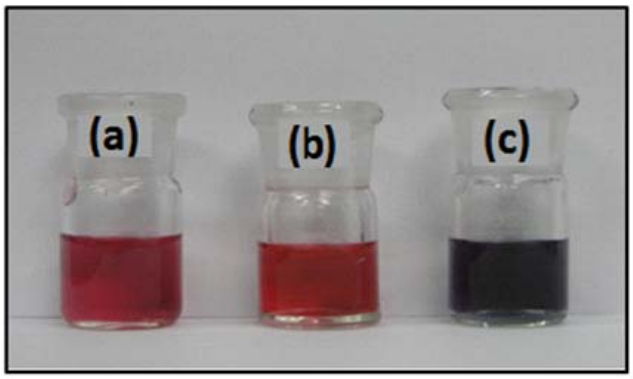

Fig. 5 Photographs of synthesized Au NPs at different concentrations of CGA in presence of 5x10-4 M $NaAuCl_4$ (a) 2.5x10-4 M CGA (b) 5x10-4 M CGA (c) 1x10-3 M CGA.

UV-vis absorption spectrum of these Au NPs shows an absorption peak at 400 nm and at around 525 nm (Figure 6). Absorption peak at 400 nm is because of the complex formed between Au^{3+} ion and CGA and the peak at 525 nm is the SPR band of Au NPs. The peak at 400 nm was found to be decreasing with time while the absorbance of peak at 525 nm increasing with time.

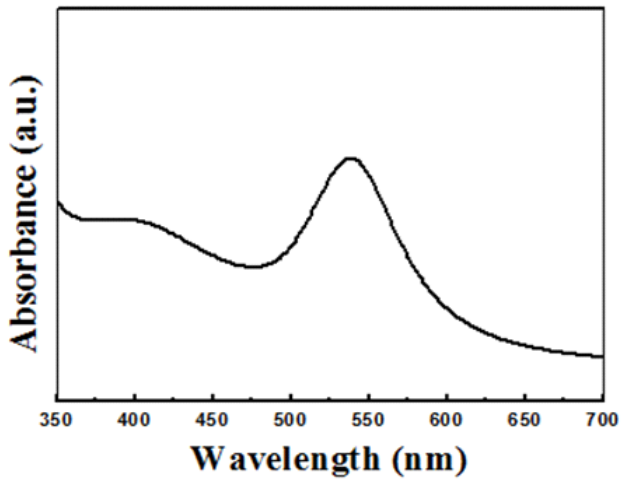

Fig. 6 Surface plasmon absorption band of Au NPs synthesized in presence of CGA

Thus, it can be stated that the complex formation between Au^{3+} and CGA leads to the reduction of Au^{3+} ions. Similar observation has been reported with Cu^{2+} ions and catechol by Jasmine et. al., [36]. Catechol is a dihydoxy benzene with two alcoholic groups at ortho position, CGA also contains the same diol moiety attached to the benzene ring thus it can be stated that the behavior of CGA is quite similar to that of catechol with copper ions. The concentration of $NaAuCl_4$ was also varied from $2.5x10^{-4}$ M to $1x10^{-3}$ M. At lower concentration of $NaAuCl_4$, complex formation at 400 nm was not observed in good amount as it was formed at high concentrations of $NaAuCl_4$. The absorption spectra for the Au NPs synthesized indicate the formation of aggregated particles. When the concentration was changed to $5x10^{-4}$ M, narrow particle size distribution was observed and the synthesized NPs were stable for quite long time. Thus, the best results in terms of stability and size distribution were obtained when the concentration of both CGA and $NaAuCl_4$ were kept $5x10^{-4}$ M. Shape and particle size distribution of synthesized Au NPs were obtained by utilizing TEM (Fig. 7a).

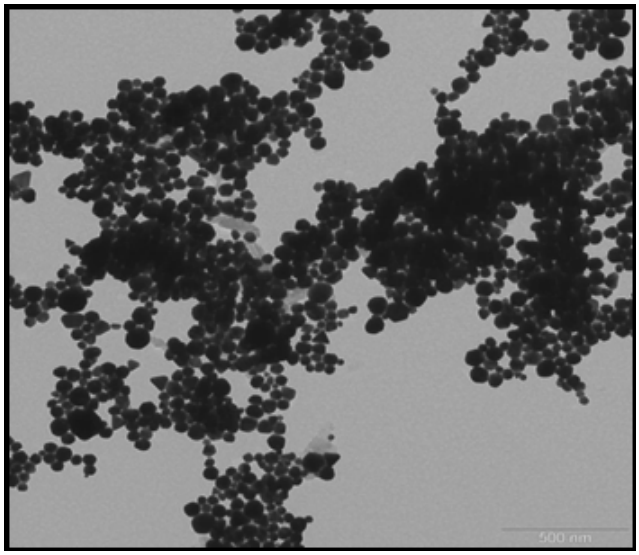

Fig. 7 (a) TEM image of synthesized Au NPs

From the TEM data, the synthesized particles were spherical in shape with average diameter of ~50±14 nm with few particles triangular in shape. A closer look at particles illustrated that they were individually dispersed. Agglomeration at some places might have taken place during sample preparation for TEM. Figure 7b represents the histogram depicting the particle size distribution of Au NPs.

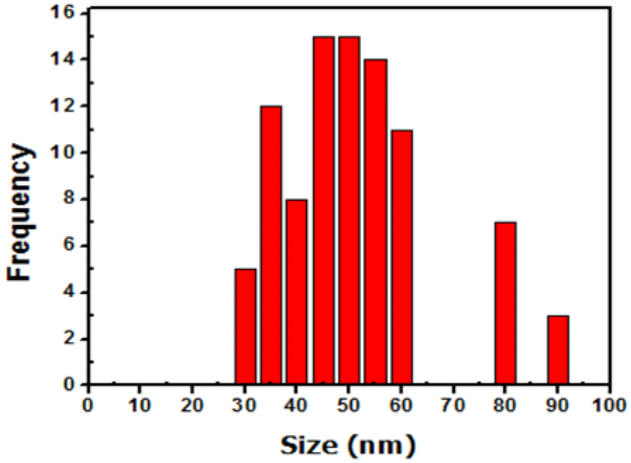

Fig. 7 (b) Size distribution of particles obtained from TEM image in Fig. 7(a)

Catalytic activity of Ag and Au NPs

Catalytic activity of Ag and Au NPs synthesized by using CGA acid was investigated for the reduction of o-nitroaniline to 1, 2 benzenediamine by $NaBH_4$. The catalytic reaction was monitored by using time dependent UV-vis absorption spectroscopy. The absorption spectrum of aqueous solution of o-nitroaniline shows maxima at 410 nm due to $n \rightarrow \pi^*$ transition. It was observed that on addition of the above synthesized NPs to the solution containing o-nitro aniline in the presence of $NaBH_4$, the absorbance at 412 nm decreased and completely disappeared with time. Typical UV–vis absorption spectra for the reaction in the presence of Ag NPs are shown in Fig. 8a.It can be seen that after the addition of Ag NPs, the peak at ~410 nm almost disappeared after 10 minutes indicating the completion of the reduction reaction. As the amount of $NaBH_4$ is taken in excess (>100 times of reactant, o-nitro aniline), the reaction could be considered as pseudo-first order reaction with respect to o-nitro aniline according to the reaction $[I_t] = [I_0]e^{-kt}$, where, I_t represents the absorbance at time 't' which corresponds to the concentration of the o-nitro aniline; I_0, absorbance at the initial stage, i.e. initial concentration of the o-nitro aniline and k, pseudo-first order rate constant. Fig. 8b represents the rate of reduction of o-nitro aniline and rate constant was found to be 0.26 min^{-1} for 0.5 pg/mL of Ag NPs.

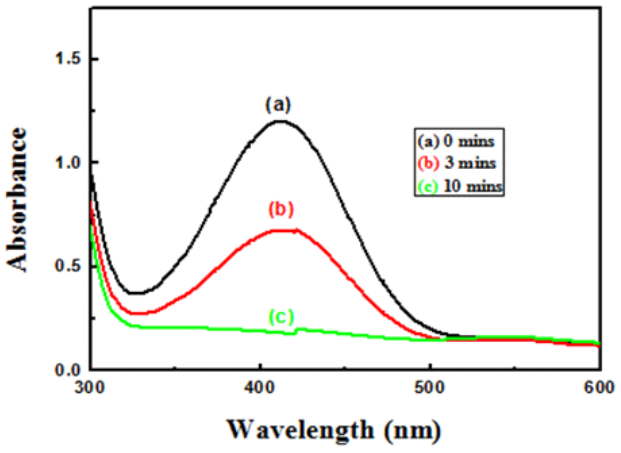

Fig. 8(a) Time-dependent variation in the absorption spectrum of o-nitro aniline in the presence of 0.5 pg/ml Ag NPs (CGA stabilized) and $NaBH_4$.

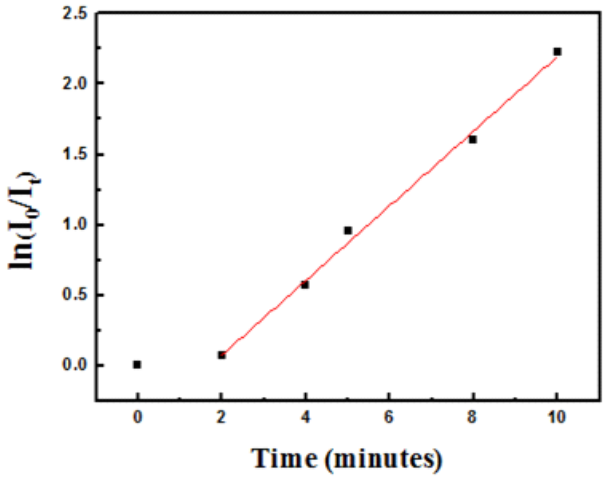

Similarly, the reaction was carried out in the presence of Au NPs, the reaction got completed in 10 minutes and the rate constant obtained was almost found to be similar for the same amount of catalyst that was used in reaction with Ag NPs (Figures 9a and 9b).

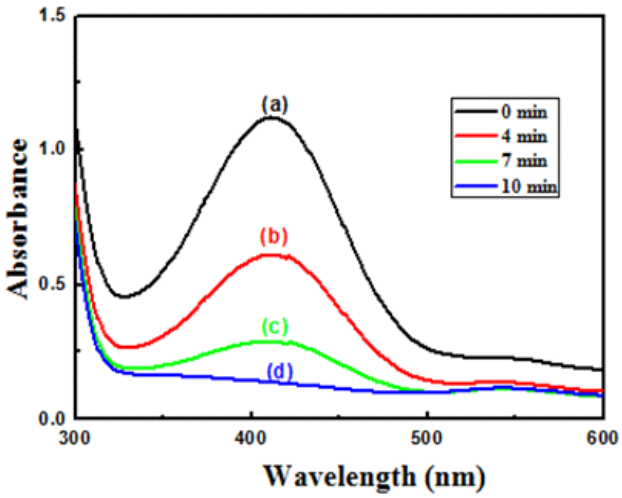

Fig. 9(a) Time-dependent variation in the absorption spectrum of o-nitro aniline in the presence of 0.5 pg/ml Au NPs (CGA stabilized) and $NaBH_4$.

SERS Study

To investigate the SERS activity of synthesized Au NPs, CV dye was chosen as probe molecule. Normal Raman spectra of CV dye was recorded and shown in Fig. 10(a). Then CV dye ($6x10^{-6}$M) was added to the synthesized Au NPs and Raman spectra was recorded as

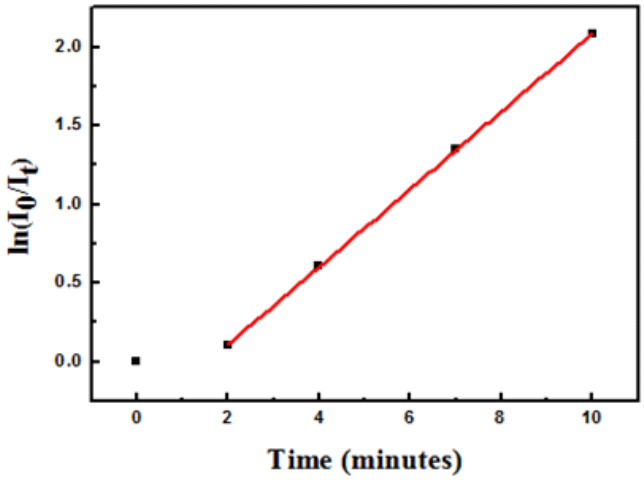

Fig. 9 (b) Logarithmic plot of relative absorbance vs. time.

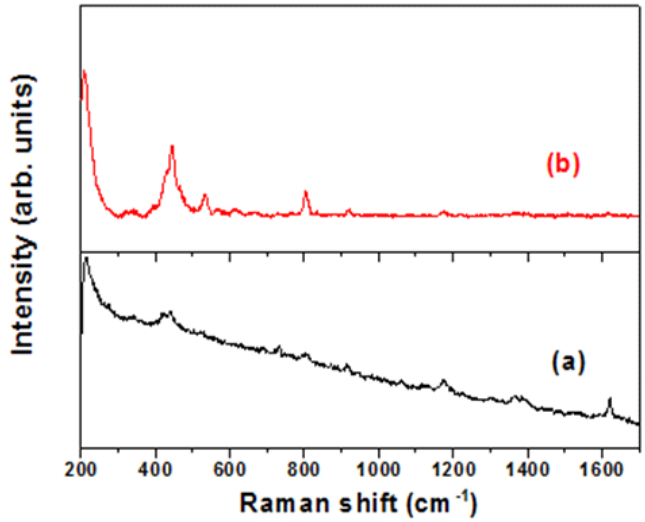

Fig. 10. (a) Raman spectra of 6x 10^{-6} M CV in aqueous solution (b) SERS spectra of 6x 10^{-6} M CV in presence of Au NPs synthesized in presence of CGA.

shown in Fig.10 (b). It can be seen that fluorescence of CV is quenched in presence of Au NPs. Raman intensity of few bands of CV was enhanced which shows interaction of CV molecules with surface of Au NPs. Thus, it is possible to detect CV at a very low concentration on CGA stabilized Au NPs. The observed Raman bands are in agreement with previous studies reported in the literature [48]. Thus, above prepared Au NPs can be employed efficiently as SERS substrate.

Conclusions

In this work, stable Ag and Au NPs were successfully synthesized and stabilized using green reduction method. UV-visible absorption spectroscopy confirms the formation of NPs. It was found that pH and ratio of CGA to metal ion precursor play a very important role in stabilization of particles. At pH 6.1, Ag NPs formed were stable may be due to the ionization of carboxylic group which helped in stabilization. For synthesis of Au NPs, the complex formation between Au^{3+} and CGA is observed which leads to the reduction of Au^{3+} ions. The synthesized NPs were found to be catalytically active towards the reduction of o-nitroaniline by $NaBH_4$. The above synthesized Au NPs in presence of CGA showed good SERS activity for detection of CV which shows that they can be explored as SERS substrate for various applications.

References

1. Daniel M.-C. and Astruc D., 2004, *Chem. Rev.*, **104**, 293.

2. El-Sayed M.A., 2001, *Acc. Chem. Res.*, **34**, 257.

3. Henglein A., 1989, *Chem. Rev.*, **89,** 1861.

4. Duann J., Yin H., Wei R. and Wang W., 2014, *Biosens. Bioelectron.*, **57,** 139.

5. Zhou Y., Zhao H., Yu H., Ding N. and Cao Q., 2011,*Colloid. Surf. A*, **391**,179.

6. Sung H.K., Oh S.Y., Park C. and Kim Y., 2013, *Langmuir*, **29**, 8978.

7. Wu X., Tang W., Hou C., Zhang C. and Zhu N., 2014, *Microchim. Acta*, **181**, 991.

8. Yang X.-H., Ling J., Peng J., Cao Q.-E., Ding Z.-T. and Bian L.-C., 2013, *Anal. Chim. Acta*, **798**, 74.

9. Jiang X.C. and Yu A.B., 2008, *Langmuir*, **24**, 4300.

10. Laliwala S.K., Mehta V.N., Rohit J.V. and Kailasa S.K., 2014, *Sens. Actuators B: Chem*, **197**, 254.

11. Song J., Wu F., Wan Y. and Ma L.-H., 2014, *Microchim. Acta*, **18**,1267.

12. Leesutthiphonchai W., Dungchai W., Siangproh W., Ngamrojnavanich N., and Chailapakul O., 2011, *Talanta*, **85**, 870.

13. Miao P., Liu T., Li X., Ning L., Yin J. and Han K., 2013, *Biosen. Bioelectron.*, **49**, 20.

14. Wiley B., Sun Y. and Xia Y., 2005, *Langmuir*, **21**, 8077.

15. Turkevich J., Stevenson P.C. and Hillier J., 1951, *Discuss. Faraday Soc.*, **11**, 55.

16. Frens G., 1973, *Nat. Phys. Sci.*, **241**, 20.

17. Lee P.C. and Meisel D., 1982, *J. Phys. Chem.*, **86**, 3391.

18. Shahverdi A.R., Minaeian S., Shahverdi H.R., Jamalifar H. and Nohi A., 2007, *Process Biochem.*, **42**, 919.

19. Kalishwaralal K., Deepak V., Ramkumarpandian S., Nellaiah H. and Sangiliyandi G., 2008, *Mater. Lett.*, **62**, 4411.

20. Basavaraja S., Balaji S.D., Lagashetty A., Rajasab A.H. and Venkataraman A., 2008, *Mater. Res. Bull*., **43,** 1164–1170.

21. Philip D., 2009, *Spectrochim. Acta- Part A*, **73**, 374.

22. Bar H., Bhui D.K., Sahoo G.P., Sarkar P., Pyne S. and Misra A., 2009, *Colloids Surf. A*, **348**, 212.

23. Dubey S.P., Lahtinen M. and M. Sillanpaa, 2010, *Colloids Surf. A*, **364**, 34.

24. Dwivedi A.D. and Gopal K., 2010, *Colloids Surf. A*, **369**, 27.

25. Prathna T.C., Chandrasekaran N., Raichur A.M. and Mukherjee A., 2011, *Colloids Surf. B*, **82**, 152.

26. Bankar A., Joshi B., Kumar A.R. and Zinjarde S., 2010, *Colloids Surf. A*, **368**, 58.

27. Linic, S., Aslam, U., Boerigter, C. and Morabito, M., 2015, *Nat. Mater.*, **14**, 567.

28. Thakkar, K.N., Mhatre, S.S. and Parikh, R.Y., 2010, *Nanomed. Nanotechnol. Biol. Med.*, **6**, 257.

29. Yoon, W.-J., Jung, K.-Y., Liu, J., Duraisamy, T., Revur, R., Teixeira, F.L., Sengupta, S. and Berger, P.R., 2010, *Sol. Energy Mater. Sol. Cells*, **94**, 128.

30. Yang, Y., Jin, P., Zhang, X., Ravichandran, N., Ying, H., Yu, C., Ying, H., Xu, Y., Yin, J. and Wang, K., 2017, *J. Biomed. Nanotechnol.*, **13**, 805.

31. Sathishkumar, M., Sneha, K., Won, S., Cho, C.-W., Kim, S. and Yun, Y.-S., 2009, *Colloids Surf. B*, **73**, 332.

32. Saha K., Agasti S.S., Kim C., Li X. and Rotello V.M., 2012, *Chem. Rev.*, **112**, 2739.

33. Gao, Y., Xie, X., Li, F., Lu, Y., Li, T., Lian, S., Zhang, Y., Zhang, H., Mei, H. and Jia, L., 2017, *Nanoscale*, **9**, 5624.

34. Chowdhuri, A.R., Bhattacharya, D. and Sahu, S.K., 2016, *Dalton Trans.*, **45**, 2963.

35. Pelaz, B., Alexiou, C., Alvarez-Puebla, R.A., Alves, F., Andrews, A.M., Ashraf, S., Balogh, L.P., Ballerini, L., Bestetti, A. and Brendel, C., et al., 2017, *ACS Nano*, **11**, 2313.

36. Jacob J.A., Biswas N., Mukherjee T. and Kapoor S., 2011, *Colloids Surf. B: Biointerfaces*, **87**, 49.

37. Hwang S. J., Jun S.H., Park Y., Cha S.-H., Yoon M., Cho S. and Lee H.-J., Park Y. 2015, *Nanomed. Nanotechnol. Biol. Med.*, **11**,1677-1688

38. Jacob J.A., Mahal H.S., Biswas N., Mukherjee T. and Kapoor S. 2008, *Langmuir*, **24**, 528.

39. Shankar, S.S., Rai, A., Ahmad, A. and Sastry, M., 2004, *J. Coll. Inter. Sci.*, **275**, 496.

40. Jain S. and Mehata M.S., 2017, *Scientific Reports*, **7**, Article number: 15867.

41. Chandran, S.P., Chaudhary, M., Pasricha, R., Ahmad, A. and Sastry, M., 2006, *Biotechnol. Prog.*, **22**, 577.

42. Noh H.J., Kim H.-S., Jun S.H., Kang Y.-H., Cho S. and Park Youmie, 2013, *J. Nanosci. and Nanotech.* **13**, 5787.

43. Zang L.Y., Cosma G., Gardner H., Castranova V. and Vallyathan V., 2003, *Mol. Cell. Biochem.*, **247,** 205.

44. Ong K.W., Hsu A. and Tan B.K., 2003, *Biochem. Pharmacol.*, **85**, 1341.

45. Belkaid, J. C., Currie, J., Desgagnes and B. Annabi, 2006, *Cancer. Cell. Int.*, **6**, 7.

46. Romero Romina, Salgado P. R., Soto C., Contreras D. and Melin V. July 2018, *Frontiers in Chemistry*, **6**, Article 208.

47. Zhang B., Xu P., Xie X., Wei H., Li Z., Mack N.H., Han X., Xu H. and Wang H.-L., 2011, *J. Mater. Chem.*, **21**, 2495.

48. Canamares M.V., Chenal C., Birke R.L. and Lombardi J.R. 2008, *J. Phys. Chem. C*, **112**, 20295.

RNI No. MAHENG/2017/74063
ISSN No. (Print) 2581-5911
ISI Impact Factor 0.883 (2018)

Degradation of Acid Orange 7 Dye using Fenton Process

Rohit R. Gurav*, Atish P. Limbare, Nitesh B. Pardeshi and Manoj B. Mandake
Department of Chemical Engineering, Bharati Vidyapeeth College of Engineering, Navi Mumbai – 400614.
Email: rohitgurav85@gmail.com; atishlimbare6@gmail.com
niteshpardeshi5@gmail.com; m.mandake@gmail.com

Abstract

Textile industries use a variety of synthetic dyes which generate a huge volume of textile effluent containing a mixture of pollutants. These pollutants are responsible for many diseases. The removal of color from textile wastewater is a major environmental concern. In this study, the removal of Acid Orange 7 dye from aqueous solution has been studied using Advanced Fenton Process. Fenton oxidation (H_2O_2 /Fe^{++}) is considered to be one of the most effective, simple and economical methods to remove pollutants from wastewater. Fenton's reagent is a result of the reaction between hydrogen peroxide (H_2O_2) and ferrous ions (Fe^{2+}) under acidic conditions. Batch experiments were performed at different initial concentrations of the dye, different pH of the solution, different ferrous sulfate and hydrogen peroxide loading and their effects on COD removal as well as optimum experimental conditions were determined. In this study, we obtained the maximum rate of COD removal upto 60% by the Fenton process. Then batch experiments were carried out for Ozonation process and the combined effect of Fenton and Ozonation process on COD and TOC reduction was studied. Fenton and Ozonation processes were used to produce $^{\cdot}OH$ (hydroxyl radical).

The results obtained from this study showed that the combination of Fenton and Ozonation Process is very effective to remove Acid Orange 7 dye.

Keywords: *Aqueous, effluent, Fenton process, hydroxyl radical, oxidation process, ozone, synthetic dye, textile industry.*

Introduction

The dyes used in the textile dyeing and printing industries not only can impart color to water sources but also can cause environmental damage to living organisms by stopping the re-oxygenation capacity of water and also blocking sunlight, thereby disturbing the natural growth activity of aquatic life[1]. Dyedtuffs are prepared from a variety of chemicals, and excess chemicals are discharged into water during the process. Sometimes products are also discharged into the wastewater during the process of salting-out. Wastewater containing dyestuffs has a COD of 3,000 – 20,000 mg/L. but it also has a dark color, which blocks sunlight.

Decolourization of coloured wastewater is very difficult using traditional physical and chemical methods. Dyestuff wastewater is composed of many organic com-

pounds that are difficult to treat by biological methods. Effective methods of decreasing COD and color are chosen depending on the type of dyestuff, and multiple processes are generally used to successfully treat twastewater [2]. The toxicity of numerous dyes renders them environmentally hazardous. Azo dyes are very common pollutants in dye effluents. Removing color from wastewater is more important than removing other colourless organic compounds, because already small amounts of dye are clearly visible and decrease the water quality [3]. Among various treatment methods, advanced oxidation processes (AOPs) are becoming important technologies for removing azo compounds. AOPs are based on the in situ generations of hydroxyl radical (•OH), which is a powerful oxidant and can attack organic compounds to produce mineral end-products. AOPs like Ozonation, Fenton process and Photocatalysis have been used for degradation of azo dyes [4].

Nowadays, chemical oxidation processes are used for water treatment in drinking water facilities and wastewater treatment plants dealing with toxic, bio refractory and highly stable compounds, viz. pharmaceuticals, pesticides, phenolic, herbicides, etc. Among the chemical oxidation processes, Ozonation is one of the methods that has proved to be very effective for the oxidation of organic pollutants such as textile dyes. Several studies with textile effluents have proved that common biologically based treatment options are ineffective in color removal. Therefore, the pollution resulting from the discharge of colored effluents is a great environmental concern since the color of textile wastewaters is quite noticeable and some dyes in textile wastewater may have carcinogenic effects [5].

Advanced Oxidation Process

AOPs is the technology used for the oxidation of a wide range of organic contaminants in polluted water. AOP methods involve the generation of powerful oxidants such as the hydroxyl radical (.OH). which are used to treat the water [6]. Advanced Oxidation Processes (AOPs) are efficient methods to remove organic contaminants AOPs processes produce very reactive oxygen species which are able to destroy a wide range of organic compounds. AOPs are more expensive than the conventional biological wastewater treatment since external energy sources (electric power, ultraviolet radiation (UV) or solar light electric power, ultraviolet radiation (UV) or solar light) are required to drive the AOP process. But AOP systems are not more expensive than well-established technologies for pollutant abatement [7].

Fenton Process

The Fenton process is used for the treatment of both organic and inorganic substances under laboratory conditions using synthetic effluents as well as real effluents from different sources like chemical, refinery and fuel terminals, engine and metal cleaning etc. Fenton Process is based on the production of highly reactive hydroxyl radicals (•OH). Fenton's reagent is a result of the reaction between hydrogen peroxide (H_2O_2) and ferrous ions (Fe^{2+}) under acidic conditions. Based on the oxidation system Fenton's reagent can be employed to treat a variety of industrial wastes containing a wide range of organic compounds like phenols, formaldehyde, pesticides, wood preservatives, plastic additives, and rubber chemicals. The wastewater treatment using Fenton process results in a reduction of toxicity, improvement in biodegradability, odor and color removal [8]. It has been demonstrated that Fenton's reagent is able to destroy toxic compounds in wastewaters such as dyes, phenols, and herbicides. Hydroxyl radical production by Fenton reagents occurs by adding H_2O_2 to Fe^{2+} salts. Special reactants and apparatus are not required for the reaction in which OH radicals are produced. The fact is that iron is available abundantly and hydrogen peroxide is environment-friendly and easy to handle.

The process is cost effective and environment friendly[9] since iron is available abundantly and Hydrogen peroxide is environmentally friendly.

Ozonation Process

Ozonation has excellent potential for decolorization due to the following reasons: (i) decolonization and degradation occur in one step, (ii) danger to humans is minimal; (iii) no sludge remains, (iv) all residual ozone can be decomposed easily into oxygen and water and iv)

ozonation is easily performed. Two possible degradation ways are available for oxidation of organics: (i) at basic pH, ozone decomposes rapidly to yield hydroxyl and other radical species in solution (Eqs.1-3) and (ii) at acidic pH, ozone is stable and can react directly with organic substrates. UV radiation can decompose ozone in water, generating highly reactive hydroxyl radicals. The hydroxyl radicals oxidize organics more rapidly than ozone. The effects of dye concentration, ozone dose, pH, the presence or absence of UV and UV intensity in ozone-based systems have been evaluated [3].

$$O_3 + OH^- \rightarrow O_3^{\bullet -} + {}^{\bullet}OH \quad (1)$$

$$O_3^{\bullet -} \rightarrow O^{\bullet -} + O_2 \quad (2)$$

$$O^{\bullet -} + H^+ \rightarrow {}^{\bullet}OH \quad (3)$$

Many studies have provided evidence that ozone can decolorize synthetic dyes which are soluble in water. There are two different primary reaction pathways for oxidation: 1) a direct attack of ozone molecule on the pollutants and generation of free radicals due to decomposition of ozone and 2) subsequent attack of these two radicals on the pollutants. The combination of ozone with UV light, H_2O_2, and MnO_2 increase the oxidizing efficiency. Ozone with UV light process is more efficient than the ozone process alone because UV radiation promotes ozone decomposition and as a result, yields additional hydroxyl radicals which increase decolourization rate[10].

In this paper we report the effects of initial concentration, pH ferrous ion and Hydrogen peroxide loading on advanced oxidation process.

Materials and Methods

Commercial grade Acid Orange 7 dy, Ferrous Sulfate ($Fe_2SO_4 .7H_2O$), 30% Hydrogen peroxide and 98% Sulphuruc acid were obtained from RLFCI, Navi Mumbai. All the chemicals were used as received.

Experimental Method

Fenton Process

An aqueous solution of the dye was taken in a glass reactor provided with a magnetic stirrer. Fenton reagent was then added and the pH was adjusted to 3-4.The reaction was carried out for 2 hours and at regular intervals of 15 minutes each, analytical samples of 10 mL each were withdrawn and stored in the dark. COD values was determined to find percentage rate of degradation of the dye at different concentrations.

Ozonation process

The experiments were carried out in a 3 neck glass reactor provided with a magnetic stirrer. 500 mL of the dye solution was in the glass reactor and pH was adjusted to 3-4 by adding Sulphuric acid. A predetermined amount of ozone gas was then passed through the dye solution. The experiment was carried out for 2 hours and at regular intervals of 15 minutes each, analytical samples of 10 mL each were withdrawn and stored in the dark. COD values were determined to find percentage rate of degradation of dye at different concentrations.

The experiments were carried out by Fenton, Ozonation and Combined Fenton-Ozonation processes and COD values were determined.

COD Measurement

The analysis was done by measuring COD of the solution. COD refers to the requirement of dissolved oxygen for both oxidation of organic and inorganic constituents. The following reagents were used for COD measurements: 0.05N $K_2Cr_20_7$, H_2SO_4, Standard 0.1NFerrous ammonium sulfate and $HgSO_4$.

The rate of COD was calculated using the formula

$$\text{COD}\,(\text{mg/L}) = \frac{(a-b) \times N \times 8000}{10}$$

where, a = 27.3 mL of $Fe(NH_4)(SO_4)_2$ for blank,
b = mL of $Fe(NH_4)2\ (SO_4)2\ 6H_2O$ for sample and

Normality (N) of FAS = 0.1N

Rate of COD reduction was calculated using the following formula

$$\text{Rate of COD reduction} = \frac{(A-B)}{A} \times 100$$

where, A is the initial COD and
B is the final COD

Kinetic Evaluation

The rate of reaction was determined using pseudo first order kinetic conditions with

with respect to the dye ,

$$-\ln \frac{Ca}{CaO} = kt$$

where, Ca and Ca0 are the dye concentration at time t and 0 respectively and k is the pseudo-first order rate constant ($time^{-1}$)

Results and Discussions

Fenton Process

1) Effect of Initial Dye Concentration

The effect of initial Acid Orange 7 on the COD reduction has been investigated at three different concentrations (100, 250 and 500 ppm). Figure. 1 shows the COD reduction with treatment time at varying initial concentration. It can be seen that the percentage of COD reduction decreases with an increase in the initial concentration of Acid Orange 7 dye. The observed decrease in COD reduction with an increase in dye concentration may be due to the fact that the presence of a higher concentration of pollutant reduces the efficiency of the formation of OH radicals in the solution. It is observed that at 500 ppm, % rate of COD reduction is 14.28%, at 250 ppm % reduction in COD is 49.44% and at 100 ppm % reduction in COD is 51.62%. Since the rate of COD reduction is maximum at 100 ppm dye concentration, all the remaining sets of experiments were performed at 100 ppm initial concentration of Acid Orange 7dye. As shown in Table 1 the kinetics data shows that rate constant decreases with increasing dye concentration -at 100 ppm rate constant were 6.11×10^3 min^{-1} but at 500 ppm it decreased to 1.28×10^3 min^{-1}. Graphs of ln(Ca0/Ca) versus time are shown in Figure 2. Its shows that R^2 values for all concentrations[11]

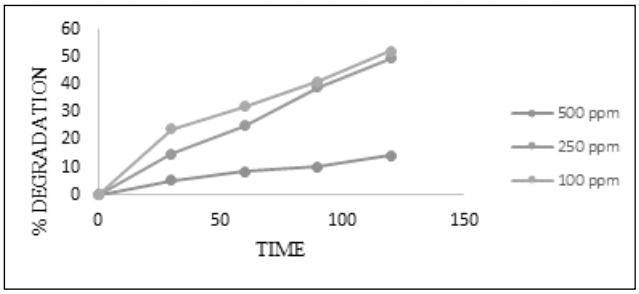

Fig. 1 Effect of initial dye concentration on percentage of COD degradation

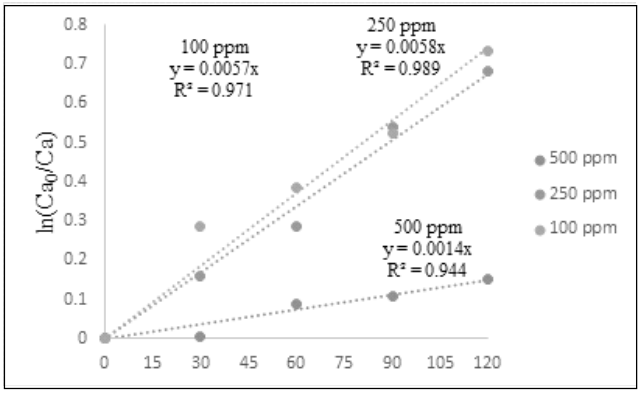

Fig. 2 Graph of ln(CaO/Ca) versus time

Table1 : Rate rate constants at different dye concentrations

ppm	% Degradation	Rate Constant k $x10^3 min^{-1}$	R^2
500	14.20	1.28	0.944
250	49.44	5.68	0.989
100	52.00	6.11	0.971

2) Effect of pH

The pH of the solution was adjusted by using NaOH and H_2SO_4. In this study, the effect of pH was observed at pH 4, 7 and 11. The extent of COD reduction is

generally observed more in the acidic condition than in the alkaline condition. At pH 4, the overall COD reduction rate is was 52% and decreased continuously with increasing pH. At pH 7 40% COD reduction was observed and at pH 11, the observed COD reduction was 29%. Maximum reduction occured in the first 30 minutes and as the time increased, reduction decreased. We observed a 26% reduction in the first 30 minutes at acidic pH 4 and total COD reduction was 52%. Similar results were obtained at other pH values (Fig.3). It can be seen that under acidic conditions, generation of hydroxyl radicals is more as compared to that in alkaline conditions.

Hence the rate constant increased with decrease in the pH value. As shown in Table 2 at pH 4 the rate constant were $6.11x10^3 min^{-1}$ and at pH 11 it was $2.85x10^3 min^{-1}$ [12].

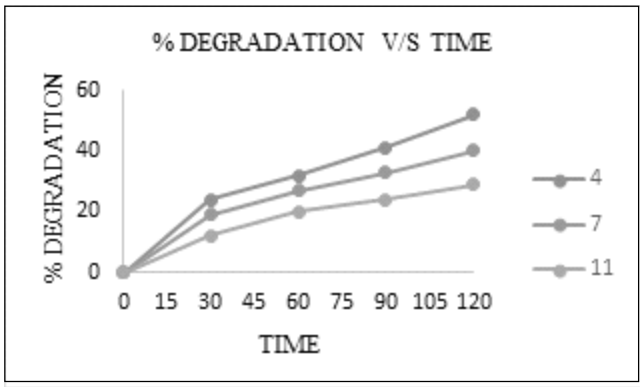

Fig. 3 Effect of pH on extent of COD reduction

Table 2: Rate rate constants at different pH

pH	% Degradation	Rate Constant k $x10^3 min^{-1}$	R^2
4.0	52	6.11	0.9613
7.0	40	4.26	0.9426
11.0	29	2.85	0.9518

3) Effect of Ferrous Sulfate Loading

In order to investigate the effect of ferrous sulfate dosage on COD removal, experiments were conducted at optimum pH value 4. Ferrous Sulfate dosage varied in the range of 0.05 to 0.2g in the H_2O_2: $Fe_2SO_4.7H_2O$ ratios of 1:1, 1:2 and 1:4. The effect of Ferrous sulfate loading on COD reduction is shown in Figure. 4. The maximum COD reduction is observed in the H_2O_2:F_eSO_4 ratio of 1:4 which is 59%. The rate constant also increases with increasing ferrous sulfate loading. The minimum reduction was observed at 1:1 ratio which is 52%. Maximum reduction were observed in first 30 minutes. As shown in Table 3 increase in ferrous sulfate loading from 1:1 to 1:4 results in increase in rate constant from $6.12x10^3$ to $7.63x10^3 min^{-1}$. It is observed that as the ratio of H_2O_2:$Fe_2SO_4.7H_2O$ increases; the COD reduction also increases [12].

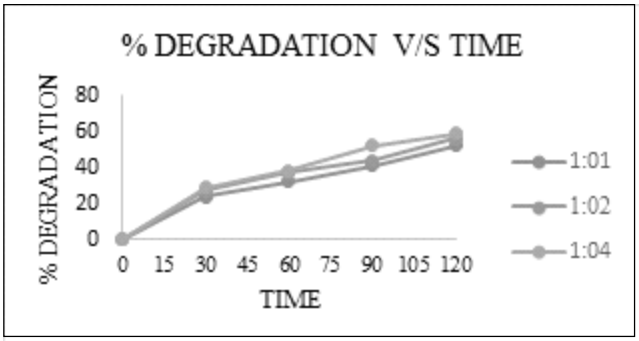

Fig. 4 Effect of Ferrous Sulfate loading on COD reduction

Table 3: Rate constants at different values of Ferrous Sulfate loading

Loading	% Degradation	Rate Constant k x 10^3 (min^{-1})	R^2
1:01	52	6.12	0.9716
1:02	56	7.04	0.9609
1:04	59	7.63	0.9613

4) Effect of Hydrogen Peroxide Loadings

To investigate the effect of hydrogen peroxide on COD removal, different ratios of $Fe_2SO_4.7\ H_2O$: H_2O_2 to 4:1, 4:2 and 4:4 were used at pH 4. The maximum COD reduction was observed in the first 30 minutes. The effect of Hydrogen Peroxide loading on COD reduction is shown in Figure. 5. At ratio 4:4, the maximum reduction (61%) was observed. Hydrogen peroxide was used as an additional source of hydroxyl radicals which is very helpful to intensify the process. It was observed that the rate of degradation increased with increase in the concentration of hydrogen peroxide. As shown in Table 4 the rate constant also increases with increasing hydrogen peroxide loading [12].

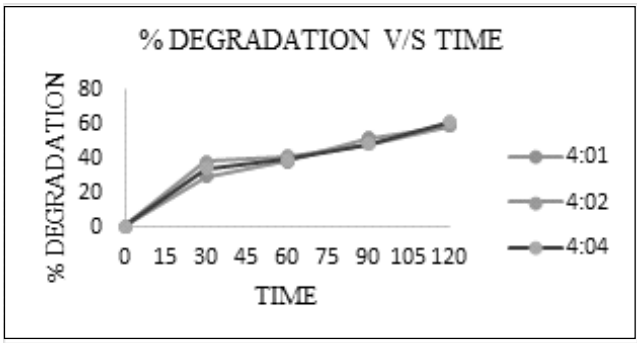

Fig. 5 Effect of hydrogen peroxide loading on COD reduction

Table 4 : Rate constants at different values of Hydrogen peroxide loading

Loading	% Degradation	Rate Constant k x 10^3 min^{-1}	R^2
4:01	59	7.42	0.844
4:02	59.12	7.42	0.928
4:04	61	7.84	0.97

Ozonation Process

1) Effect of Initial Dye Concentration

In order to study the feasibility of the ozonation process for different concentrations of dye, experiments were carried out by varying the initial concentration of dye from 100 to 500 ppm. It is observed that increase in dye concentration results in decrease in COD reduction rate (Figure 6).

The reason could be that under the given conditions, the ratio of ozone molecules to dye molecules in the solution decreases with increase in dye concentration. More ozone would be consumed at higher dye concentrations. The effect of initial dye concentration on COD reduction is shown in Figure. 6. The rate of COD reduction is 36% at 100 ppm initial AO7 concentration and 11 % at 500 ppm rate of COD reduction. As shown in Table 5, the rate constant at 100 ppm were $6.11x10^3$ min^{-1} and 0.878 min^{-1} 500 ppm. The rate constant decreased with increase in initial dye concentration. The time for COD reduction would be longer for higher initial dye concentration [13].

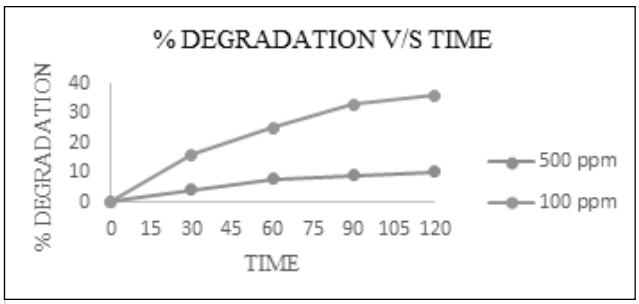

Fig. 6 Effect of initial dye concentration on COD reduction

Table 5: rate constants at different initial dye concentrations

Concentration	% Degradation	Rate Constant k min^{-1}	R^2
100 ppm	36	$6.11x10^3$	0.9598
500 ppm	11	0.878	0.9073

2) Effect of pH

The extent of COD reduction is generally observed more under alkaline conditions than under acidic conditions. The effect of pH on COD reduction is shown in Figure 7.

At pH 4 the overall COD reduction rate was 26% which decreased continuously at increasing pH. At pH 7 we get 38% COD reduction and at pH 11, the observed COD reduction was 49%. As shown in Table 6, the rate constant also increases with increasing pH values. COD reduction was more under alkaline conditions because free-radical oxidation is favored at higher pH while molecular ozone oxidation tends to dominate under acidic conditions, simply because the production of hydroxyl radicals is enhanced by alkaline conditions. The free radicals are more powerful oxidants than molecular ozone[14].

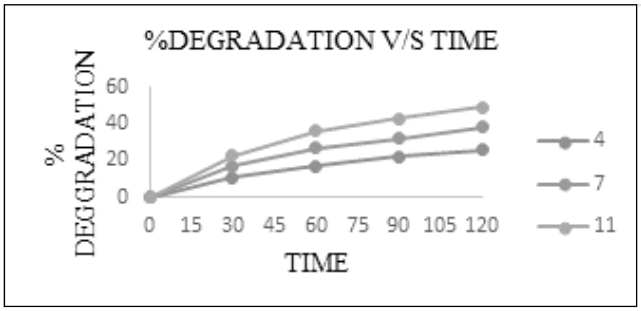

Fig. 7 Effect of pH on extent of COD reduction

Table 6 : Rate constants at different pH values

pH	% Degradation	Rate Constant $kx10^3min^{-1}$	R^2
4.0	26	2.5	0.95
7.0	40	3.98	0.94
11,0	49	5.61	0.94

Combination of Fenton and Ozonation Processes

The effect of the combination of Fenton and Ozonation processes on COD reduction was investigated. The concentrations considered for the experiment were on the basis of the ratio of H_20_2: $Fe_2SO_4.7H_2O$ as 4:4 and the pH range 4 to 11. At pH 4, the COD reduction was 66% and at pH 11 the COD reduction was 74% (Figure 8). The initial pH of wastewater plays an important role in the oxidation efficiency. It is known that OH- can accelerate the generation of •OH through the decomposition of O_3 molecule, thus high pH value is helpful for the indirect reaction of O_3 in some case. However, in strongly alkaline solution, •OH is rapidly converted to its conjugate base •O- that has a lower oxidation potential compared with •OH, causing mineralization. On the other hand, Fenton processes have high catalytic activity under acidic condition (pH = 4), which is attributed to the stability of Fe (II) in this pH range. The effect of initial pH on TOC removal efficiencies of O_3/Fenton system was investigated in the pH range 4-11. At pH 4 TOC reduction were 60% and at alkaline pH, TOC reduction was 80%. As shown in Table 7, the first order reaction rate constants at pH 4 and 11 were 0.0089 min^{-1} and 0.012 min^{-1} respectively.

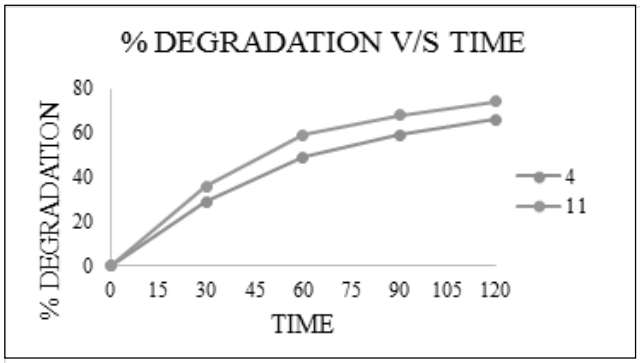

Fig. 8 Combined effect of Fenton and Ozonation processes on extent of COD degradation

Table 7 Kinetic rate constants for combine Fenton and Ozonation process at different pH

pH	% Degradation	Rate Constant k (min^{-1})	R^2
4.0	66	0.0089	0.97
11.0	74	0.012	0.99

Conclusions

The degradation of Acid Orange 7 dye using Fenton, Ozonation and combined Fenton and Ozonation processes has been investigated.

Fenton process can be effectively used for the degradation of Acid Orange 7 dye. At pH 4 and AO7:Fe2SO4: H2O2 ratio 1:4:4 we obtained maximum COD reduction which is 61%. Fenton process can be effective in acidic conditions.

Ozonation processes were less effective for COD reduction than the Fenton process but color removing efficiency of Ozonation process is good. The COD reduction obtained from Ozonation process for 100 ppm dye concentration at pH 11 was 49%. Ozonation process can be effective at high pH values.

The Combination of Fenton and Ozonation process were most effective for COD as well as TOC reduction. COD and TOC reduction values from the combined process were 74 % and 80% respectively at pH 11.

The combined Fenton and Ozonation process works effectively at high pH value rather than at low pH values.

Acknowledgments

Authors wish to thank the teaching and laboratory staff of Bharati Vidyapeeth College of Engineering, Navi Mumbai, India for help and support.

References

1. Konsowaa, A. H., Ossmanb, M. E., Yongsheng Chenc and John C. Crittendend., 2010, *Journal of Hazardous Materials*, **176**, 181-185

2. Jae-Wook Choi, Hyung Keun Song, Whun Lee, Kee-Kahb Koo, Choon Han and Byung-Ki Na., 2004, *Korean* J. *Chem. Eng*., **21(2),** 393-403

3. Chung-Hsin Wua, Chao-Yin Kuob and Chung-Liang Chang., 2007, **91(1)**, 161-168

4. Jianming Zheng, Zhanqi Gao, Huan He, Shaogui Yang and Cheng Sun., 2016, *Chemosphere*,**150**, 40-48.

5. Jyun-Hong Shen, Jao-Jia Horng, Yeoung-Sheng Wang and Yan-Ru Zeng., 2017, *Chemosphere*, **17**, 1-39

6. Sermin Gul, Ozlem Ozcan and Oktay Erbatur., 2007, *Dyes and Pigments*,**75(2)**, 426-431

7. Gholamreza Moussavi an Maryam Mahmoudi, 2009,*Chemical Engineering Journal*, 1-7

8. Arjunan Babuponnusami and Karuppan Muthukumar., 2013, *Journal of Environmental Chemical Engineering*, **2(1),** 1-16

9. Roberto Andreozzi and Vincenzo Caprio., 1999,*Catalysis Today*, **53**, 51-59

10. Arlindo C. Gomesa,, Luis R. Fernandesa and Rogerio M.S. Simoes. 2012, *Chemical Engineering Journal*, **189-190**, 175–181

11. Pankaj N. Patil, Sayali D. Bote and Parag R. Gogate., 2014, *Ultrasonic Sonochemistry*, **21**, 1770-1777

12. Xuanmo Liu, Muqing Qiu and Chengcai Huanga., 2011, *Procedia Engineering*, **15**, 4835–4840

13. Tehrani-Bagha, A.R., Mahmoodi, N.M. and Menger. F.M., 2010, *Desalination*, **260**, 34–38

14. Kintoo Yong, Jiangning Wu and Susan Andrews., 2015, *The Journal of the International Ozone Association*, 257-263

RNI No. MAHENG/2017/74063
ISSN No. (Print) 2581-5911
ISI Impact Factor 0.883 (2018)

Removal of Methylene Blue from Aqueous Solution using Rice Husk as Adsorbent

Advait Swamy, Ajay S. Nirmal*, Omkar V. Sakpal and Manoj B. Mandake
Department of Chemical Engineering , Bharati Vidyapeeth College of Engineering, Navi Mumbai – 400614
Email*: ajaynirmal85@gmail.com; advait.swamy01@gmail.com
sakpalomkar149@gmail.com; m.mandake@gmail.com

Abstract
Dyes are coloured organic compounds that can impart colour to other substances. Many industries like the textile industry use dyes to colour their products and thus produce wastewater containing organics having a strong colour. During the dyeing process, the percentage of dye lost in wastewater is 50% of the dye added because of the low levels of dye-fibre fixation. To find an effective but cheap method for treatment of wastewater containing dye, rice husk as agricultural by product has been used for adsorption of Methylene blue (MB) from aqueous solution. The effects of various parameters such as initial concentration of Methylene blue, rice husk dosage and pH were examined and their optimum experimental condition were determined. It was found that the adsorption of Methylene blue on rice husk followed Langmuir isotherm. The kinetics of adsorption was studied using pseudo first order and pseudo second order models and sorption data was found to follow pseudo second order model. The mechanism of the rate controlling step was determined by applying intraparticle diffusion model for the mass transfer. The sorption was found to be controlled by both intraparticle diffusion as well as adsorption. The results indicate that rice husk is a good adsorbent for removing Methylene blue from aqueous solution.

Keywords: *Methylene blue dye, Rice husk, Adsorption, Langmuir isotherm, Kinetics, Mechanism*

Introduction

Removal of colour from waste effluents becomes environmentally important because even a small quantity of dye in water can be toxic and highly visible. Since the removal of dyes from wastewater is considered an environmental challenge and government legislation requires textile wastewater to be treated, there is a constant need to have an effective process that can efficiently remove these dyes. Numerous techniques were used in the recent past for decolourisation of dyes. Among them adsorption technique has got maximum potential for the removal of dyes. Adsorption being a physical process, is less expensive and less time consuming and hence is widely accepted. [2]

The various methods of dye removal from dye-containing industrial effluents have been discussed under three categories[3] :-

1. Chemical
2. Physical
3. Biological

Currently the main methods of textile dye treatment are

by physical and chemical means such as: Fenton process, Photo/Ferri-Oxalate system, Combined Photocatalytic and Electrochemical treatment, Photocatalytic degradation using UV/TiO_2, Sonochemical degradation, Biodegradation, Photo-Fenton processes, Integrated chemical - Biological degradation, Electrochemical degradation, Adsorption process, ozonation, oxidation, Nano-Filtration, Chemical precipitation, Ion - Exchange and Reverse Osmosis. [4]

Among treatment technologies, adsorption is rapidly gaining prominence as a method of treating aqueous effluent. Some of the advantages of adsorption process are possible regeneration at low cost, availability of known process equipment, sludge-free operation and recovery of the sorbet. [5] Adsorption is a well-known equilibrium separation process and an effective method for water decontamination applications. Adsorption has been found to be superior to other techniques for water re-use in terms of initial cost, flexibility and simplicity of design, ease of operation and insensitivity to toxic pollutants. Adsorption also does not result in the formation of harmful substances. Activated carbon is the most widely used adsorbent for dye removal because of its extended surface area, micro-pore structures, high adsorption capacity and high degree of surface reactivity. However, adsorption by activated carbon has some limitations such as the cost of the activated carbon, the need for regeneration of the used carbon and the loss of adsorption efficiency after regeneration. This has led to the search for cheaper alternatives. [6]

There have been many attempts to find inexpensive and easily available adsorbents to remove the pollutants such as the agricultural solid wastes where according to their physic-chemical characteristics and low cost they may be good potential adsorbents. Agricultural waste materials have little or no economic value and often pose a disposal problem. The utilization of agricultural waste is of great significance. A number of agricultural waste materials are being studied for the removal of different dyes from aqueous solutions at different operating conditions. [5] Agricultural wastes are renewable, available in large amounts and less expensive as compared to other adsorbent materials. Agricultural wastes are better than other adsorbents because the agricultural wastes are usually used without or with a minimum of processing (washing, drying, grinding) and thus reduce production costs by using a cheap raw material and eliminating energy costs associated with thermal treatment.[1] Agricultural waste includes (but not limited to) banana peel, rice husk, peanuts hull, orange peel, date pit, broad bean peel, almond shells, etc. The use of these low-cost bio-sorbents is recommended since they are relatively cheap or of no cost, easily available, renewable and show high affinity to dyes. [7]

Material and Methods

Methylene blue was chosen for the adsorption study due to its strong adsorption onto solids. Methylene blue has a molecular weight of 373.9 g, which corresponds to Methylene blue hydrochloride with three molecules of water of crystallisation.

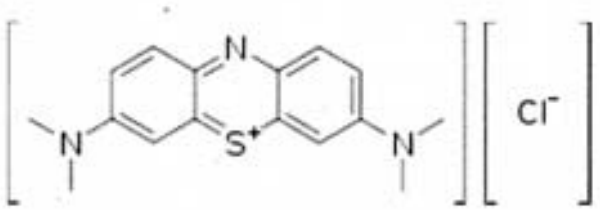

The structure of the Methylene blue is Methylene blue, a cationic dye, is not regarded as acutely toxic, but it has various harmful effects. On inhalation, it can give rise to short periods of rapid or difficult breathing, while ingestion through the mouth produces a burning sensation and may cause nausea, vomiting and gastric problems.[8]

Rice husk used in the present investigation was collected directly from local farms. The collected material was washed several times with distilled water to remove all the dirt particles. The washed material was then dried in an hot air oven at 80°C for 8 hr. The dried material was then ground using domestic mixer and sieved to obtain a mixture of constant particle size of 100 mesh. The mixture was stored in a glass bottle for further use.

Equilibrium studies

Equilibrium experiments were carried out by treating 1g of rice husk with 100 mL of dye solutions of dye concentrations 500, 250 and 100 mg/L each in 300mL stoppered bottles. The mixtures were agitated using shakers at a constant agitation speed. The agitation was carried for 4 h until equilibrium was reached. The amount of adsorption at equilibrium qe (mg/g) was calculated[9,10] by the equation,

$$Q_e = \frac{(C_o - C_e)V}{W} \quad (1)$$

where, Co and Ce (mg/L) are the liquid phase concentrations of dye at initial time and equilibrium time t, respectively. V (L) is the volume of the solution and W (g) is amount of adsorbent used.

The dye removal was calculated[10] as follows,

$$\text{Adsorption Percentage (\%)} = \frac{C_0 - C}{C_0} \times 100 \quad (2)$$

where C (mg/L) is liquid phase concentration at time t.

Effect of adsorbent dosages

The effect of rice husk mass on the amount of colour adsorbed was obtained by contacting 100 mL of dye solution of initial dye concentration 100 mg/L with different weighed amounts (0.5, 1 and 1.5 g) of rice husk using shakers at room temperature (32^0C) for 4 hr till equilibrium was reached. After equilibration, the samples were centrifuged and the concentration in the supernatant dye solution was determined using COD.

Effect of pH

The effect of pH on the amount of color removal was analyzed at different pH (i.e. 4, 7 and 10). The pH was adjusted using 1 N NaOH and 1 N HCl solutions. 100 mL of dye solution of 100 mg/L was agitated with 1 g of rice husk using shakers at room temperature (32^0C) for 4 hr till equilibrium was attained.The samples were then centrifuged and the concentration in the supernatant dye solution was determined using COD reduction.

Isotherm studies

The Langmuir model is valid for monolayer adsorption onto a surface with a finite number of identical sites which are homogeneously distributed over the adsorbent surface. The well-known expression of the Langmuir model[11,12,13,14] is given as

$$q_e = \frac{q_{max} K C_e}{1 + K C_e} \quad (3)$$

where qe is the amount of dye adsorbed on adsorbent at equilibrium, Ce is the equilibrium concentration in the solution, qmax the maximum adsorption capacity and K is the adsorption equilibrium constant. The linear form of this equation is written as

$$\frac{C_e}{q_e} = \frac{1}{k.q_{max}} + \frac{C_e}{q_{max}} \quad (4)$$

A plot of Ce/qe versus Ce is a straight line with slope 1/qmax and an intercept of 1/Kqmax. However, the Freundlich model is an empirical equation based on adsorption on a heterogeneous surface suggesting that binding sites are not equivalent and/or independent. Freundlich equation is expressed[11,12,13,14] as

$$qe = K_F C^{1/n} \quad (5)$$

where K_F is an indicator of the adsorption capacity and n that of the adsorption intensity, respectively. The logarithmic form of this equation is given by the following equation:

$$\ln(q_e) \ln K_F + \frac{1}{n} \ln Ce \quad (6)$$

From the linear plot of ln (q_e) versus ln Ce, K_F and 1/n values can be obtained.

Adsorption kinetics

Kinetic models have been proposed to determine the mechanism. The mechanism of adsorption depends on the physical and/or chemical characteristics of the adsorbent as well as on the mass transport process. In order to determine the mechanism of adsorption of

Methylene blue, pseudo-first and pseudo-second order kinetic models have been proposed as follows:

Lagergren model-
The integrated form of the model is

$$\ln (qe - q) = \ln(qe) - k_1 t \quad (7)$$

where q is the amount of dye adsorbed at time t (min), qe the amount of dye adsorbed at equilibrium and k1 is the rate constant for pseudo-first order adsorption.

Pseudo-second order model
The adsorption kinetics can also be studied using a pseudo-second order reaction. The integrated linear form of this model is

$$\frac{t}{q} = \frac{1}{k_2 q_e^{\ 2}} + \frac{t}{q_e} \quad (8)$$

where k_2 is the pseudo-second order rate constant of dye adsorption. The plot of t/q versus t of Eq. (8) should give a linear relationship, from which qe and k_2 can be determined from the slope and intercept of the plot respectively.

Since the models mentioned above cannot identify a diffusion mechanism, the intraparticle diffusion model is also tested to find the rate controlling step. In this model, the rate of intraparticular diffusion is a function of $t^{1/2}$ as given by the following equation and can be calculated by linearization of the resulting curve:

$$q = f\left(\frac{Dt}{rp}\right)^{1/2} = K_i t^{1/2} \quad (9)$$

where r_p is the particle radius, D the effective diffusivity of the dye within the particle and K_j is the intraparticular diffusion rate. [11,12,13,14]

Results and Discussion

Effect of initial dye concentration

Figure 1 shows the effect of initial dye concentration on its adsorption on rice husk. As shown in Fig.1 initially the % COD reduction is slightly greater for 500 mg/L solution. This indicates that adsorption i.e. dye uptake (mg/g) increases with increase in initial dye concentration. The concentration is an important driving force to overcome all mass transfer resistance of the dye between aqueous and solid phases. Hence initial dye concentration will enhance the adsorption process. But at equilibrium time, % COD reduction decreases with increase in dye concentration. This means that the percentage removal of dye decreases with increase in initial dye concentration because the adsorption capacity of 1g of rice husk is fixed and and goes on decreasing as the process progresses. After some time there is no free surface left for further adsorption of dye and hence percentage removal decreases. As initial dye concentration increases from 100 to 500 mg/l, the % COD reduction decreases from 48.07% to 38.03%.

Effect of adsorbent dosages

The effect of adsorbent dosage on the adsorption rate of Methylene blue was studied in the adsorbent range 0.5 to 1.5 g/L (Figure 2). The plot of % COD reduction verses contact time indicates that % COD reduction for 1.5 gram adsorbent is maximum (45.79%) and decreases as the adsorbent dose decreases. % COD for 0.5 gram dosage is 32.24%.

Hence the % dye removal increases with increase in adsorbent dosage. Also COD reduction for 1 gm

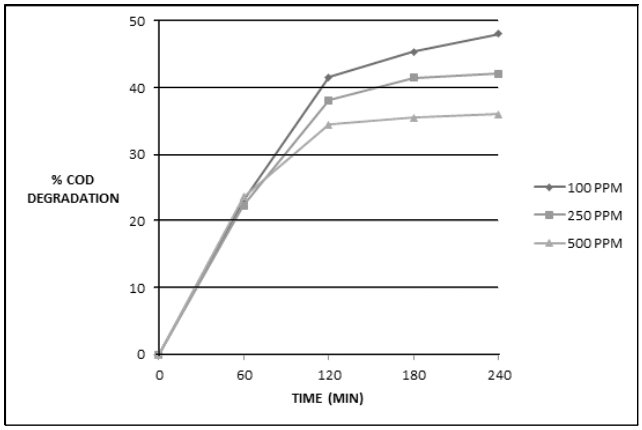

Fig.1 Effect of initial concentration on removal of Methylene blue by rice husk (w=1g/100 mL, at room temp.)

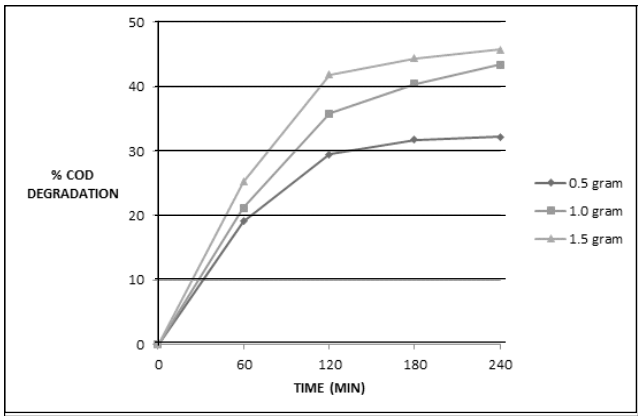

Fig.2 Effect of adsorbent mass on adsorption of Methylene blueon rice husk (C_o=100mg/L, V=100 mL, at room temp.)

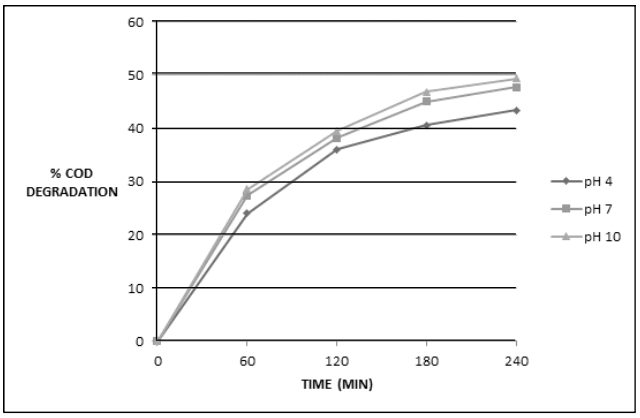

Fig.3 Effect of solution pH on Methylene blue adsorption on rice husk (C_o=100 mg/L, W=1g/100 mL, at room temp.)

(43.39 %) and 1.5 gm (45.79 %) dosage is approximately equal but equilibrium time for 1.5 g dosage is 3 hours while that for 1g dosage it is 4 hours. Hence using high adsorbent dosage, equilibrium time may be reduced. But as adsorbent mass increases and dye concentration remains constant, more adsorbent surface remain unoccupied and dye uptake decreases.

Effect of pH

Effect of pH on adsorption of dye solution was studied by varying pH keeping all other experimental conditions constant. Figure. 3 shows the plot of % COD reduction verses contact time. % COD reduction increase with increase in pH in the range 2-7, after which pH does not have influence on adsorption process. The % COD reduction values for 4, 7 and 10 pH solution are 43.45%, 47.81% and 49.44% respectively. This means that the adsorption and dye uptake increase as pH of solution increases upto 7 after which increase in pH does not show any significant effect. Several reasons may be attributed to dye sorption behaviour of the sorbent relative to solution pH. The surface of rice husk may contain a large number of active sites and the solute (dye ions) uptake can be related to the active sites and also to the chemistry of the solute in the solution.

At lower pH, the surface may get positively charged, thus making H+ ions compete effectively with dye cations causing a decrease in the amount of dye adsorbed. At higher pH the surface of rice husk particles may get negatively charged, which enhances the adsorption of positively charged dye cations through electrostatic forces of attraction. The surface of the adsorbent becomes saturated at a particular pH value resulting in a constant uptake of dye.

Adsorption isotherms

Langmuir and Freundlich isotherms were used to study the adsorption of Methylene blue on rice husk adsorbent.

The Langmuir adsorption model is based on the assumption that the maximum adsorption corresponds to the saturated monolayer of solute molecules on adsorbent surface. The linear form of the Langmuir isotherms is given by Eq. (4). As shown in Fig.4, the adsorption obeys the Langmuir isotherm and Langmuir constants qmax and b were determined from the slope and intercept respectively of the plot (Table 1).

Table 1 : Langmuir isotherm constants and correlations for Methylene blue adsorption on rice husk adsorbent

q_{max}(mg/g)	b(L/mg)	R^2
39.0625	$2.64*10^{-3}$	0.9933

The essential characteristics of Langmuir isotherms can be expressed in terms of the dimensionless constant separation factor R_L describe by Eq. (10),

$$R_L = \frac{1}{1+bC_0} \quad (10)$$

where C_0 (mg/L) is the highest initial concentration of adsorbent. The parameter R_L indicates the nature of shape of the isotherm accordingly:

$R_L > 1$	Unfavourable adsorption
$0 < R_L < 1$	Favourable adsorption
$R_L = 0$	Irreversible adsorption
$R_L = 1$	Linear adsorption

The value of R_L in the present investigation was found to be 0.7909 indicating that the adsorption of dye on rice husk i was favourable at operating conditions.

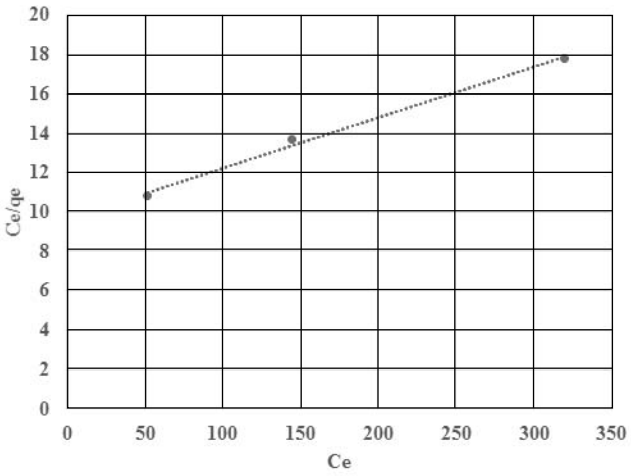

Fig.4 Langmuir isotherm for Methylene blue adsorption on rice husk

The Freundlich isotherm is used for non-ideal sorption that involves heterogeneous surface energy and is described by Eq. 5. The magnitude of the exponential, 1/n gives an indication of the favourability of absorption. The value $n > 1$ represents the favourable adsorption process. The linear plot of the Freundlich isotherm is shown in Eq. 6.

The values of K_F and n can be calculated from the intercept and slope respectively of the linear plot (Figure 5). Since the intercept of the linear plot is negative, Freundlich isotherms does not describe the adsorption

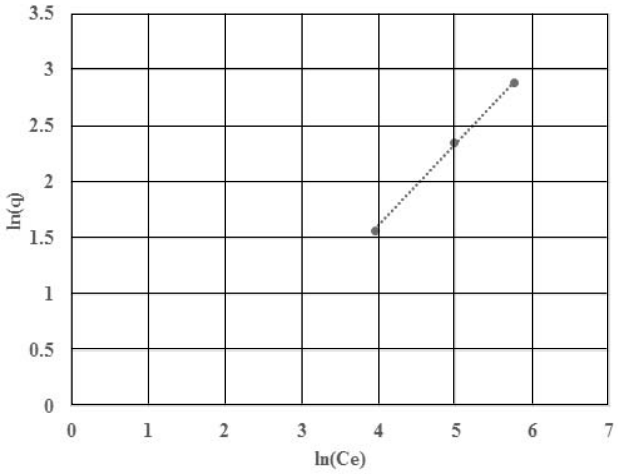

Fig.5 Freundlich isotherm for Methylene blue adsorption on rice husk

of dye on rice husk. It was observed that the equilibrium sorption data were very best represented by the Langmuir isotherm and confirms the monolayer coverage process of the dye on rice husk.

Adsorption kinetics

In order to investigate the adsorption process of Methylene blue on rice husk, pseudo-first order, pseudo-second order and intraparticle diffusion modesl were used. The plot of the linearized form of the pseudo-first order equation is shown in Fig. 6. The values of k_1, qe and correlation coefficients are compared in Table 2. The results show that the correlation coefficients obtained for the first order kinetic model is 0.9908. The theoretical qe values determined from this model did not give reasonable values, The pseudo first order model cannot satisfactorily describe the adsorption of Methylene blue on rice husk as the theoretical values of q_e determined from this model differed greatly from the experimental values.

The linearized form of the pseudo-second order model is presented in Fig. 7. The values of correlation coefficient of the model were very high and the theoretical qe values were much close to the experimental qe values. (Table 2).

The constant k_2 used to calculate the initial sorption rate, h (mg g^{-1} min^{-1}) at t'!0 was calculated as follows:

$$h = k_2 q_e^2 \quad (11)$$

The value of h in the present investigation was found to be 0.06073 mg g^{-1} min^{-1}.

Table 2: Comparison of the pseudo first order, pseudo second order adsorption rate constants and calculated and experimental qe value.

$q_{e,\ exp}$ (mg/g)	Pseudo first order model		Pseudo second order model	
	k_1(1/min)	q_e (mg/g)	k_2(g/mg.min)	q_e (mg/g)
4.81	2.21	22584.07	$1.06x10^{-3}$	7.59

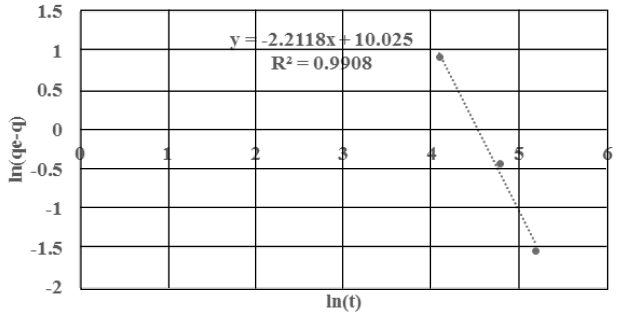

Fig.6 : Pseudo first order kinetic plot for Methylene blue on rice husk (C_0=100 mg/L;V-100 mL;w-=1g; at room temperature)

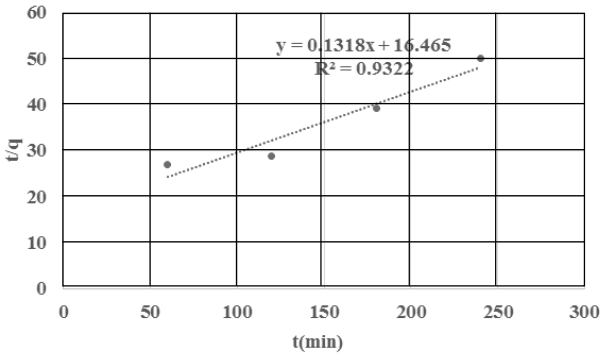

Fig. 7 :Pseudo second order kinetic plot for Methylene blue on rice husk (C_0=100 mg/L; V=100mL; w=1g; at room temperature.)

The results indicate that the pseudo-second order kinetic model provides a better correlation for the adsorption of Methylene blue on rice husk.

The adsorption of MB ont rice husk generally follows three consecutive steps - external diffusion, intraparticle diffusion and adsorption. One or more of these steps can control the adsorption kinetics . In the simplified model, it is assumed that the first linear stage represents a rapid external diffusion and surface adsorption which is neglected, the second linear stage represents a gradual adsorption stage where the intraparticle diffusion is rate limited, and the final stage is the equilibrium stage.[15]

The intraparticle diffusion parameter, K_i for this region was determined from the slope of the linear plot of q versus $t^{1/2}$.(Figure 8) Since the linear plot did not pass through the origin, the intraparticle diffusion was not the only rate controlling step.

In a well-agitated batch system, the external diffusion resistance is much reduced hence the intraparticular diffusion along with adsorption are more likely to be rate controlling steps.

Conclusions

The present study shows that rice husk, an agricultural waste biomaterial can be used as an effective adsorbent for the removal of Methylene blue from aqueous solution. The amount of dye adsorbed was found to vary with initial solution concentration, pH and adsorbent dose. The amount of dye uptake (mg/g) was found to

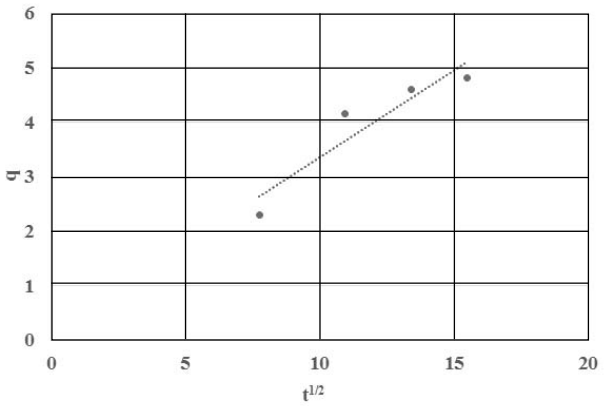

Fig. 8 Intraparticle diffusion (C_0=100 mg/L; V=100mL; w=1g; at room temperature.)

increase with increase in solution concentration and pH and found to decrease with increase in adsorbent dosage. The adsorption data agreed well with Langmuir isotherm model with monolayer adsorption capacity of 39.0625 mg/g at room temperature. The value of the separation factor, R_L, indicated the dye/rice husk system was a favourable adsorption system. The suitability of pseudo first order kinetic and pseudo second order kinetic models for the adsorption of Methylene blue on rice husk was also explored. The adsorption data were found to follow pseud-second order kinetics. The dye uptake process was found to be controlled by external mass transfer at earlier stages and by intraparticle diffusion at later stages.

References

1. Kayode Adesina Adegoke and Olugbenga Solomon Bello, 2015, *Water Resources and Industry,* **12**, 8-24.

2. Neetu Sharma, Tiwari, D.P. and Singh, S.K., 2012, *International Journal Of Scientific & Engineering Research,* **3(2)**, 1-10.

3. Tim Robinson, Geoff Mcmullan, Roger Marchant and Poonam Nigam, 2001, *Bioresource Technology*, **77(3**), 247-255.

4. Mohamad Amran, Mohd Salleh, Dalia Khalid Mahmoud, Wan Azlina Wan Abdul Karim and Azni Idris, 2011, *Desalination,* **280**(**1–3**), 1-13.

5. Amit Bhatnagar and Mika Sillanpaa, 2010, *Chemical Engineering Journal*, **157(2,3),** 277-296.

6. Mohd. Rafatullaha, Othman Sulaimana, Rokiah Hashima and AneesAhmad, 2010, *Journal Of Hazardous Materials,* **177(1–3**), 70-80.

7. Bharathi,K.S. and S. T. Ramesh,S.T.,2013, *Applied Water Science*, **3(4)**, 773–790.

8. Dursun Ozer, Gulbeyi Dursun and Ahmet Ozer, 2007, *Journal Of Hazardous Materials*, **144**, 171–179.

9. Gurusamy Annadurai, Ruey Shinjuang and Duu Jonglee, 2002, *Journal of Hazardous Materials* **92(3)**, 263-274.

10. Hameed, B.H., Krishni, R.R. and Sata, S.A., 2009, *Journal of Hazardous Materials*, **162(1),** 305-311.

11. Namasivayam, C., 1998, *Bioresource Technology*, **64**, 77-79.

12. Namasivayam, C. and N. Kanchana , N., 1992, *Chemosphere*, **25(11)**, 1691-1705.

13. Vadivelan,V. and Vasanth Kumar, K., 2005, *Journal of Colloid and Interface Science,* **286(1**), 90-100.

14. Renmin Gong, Mei Li, Chao Yang, Yingzhi Sun and Jian Chen, 2005, *Journal Of Hazardous Materials*, **B121**, 247- 250.

15. Dursun Özer Gülbeyi and Dursun Ahmet Özer, 2007, *Journal Of Hazardous Materials*, **144(1.2)**, 171-179.

RNI No. MAHENG/2017/74063
ISSN No. (Print) 2581-5911
ISI Impact Factor 0.883 (2018)

Scavenging of Reactive Oxygen Species by Ferulic Acid: A Pulse Radiolysis Study

H.S. Mahal [1], A.D. Belapurkar [1], G.B. Maru [2], S. Deshpande [2], S. Naumov [3] and T. Mukherjee [1]

[1] Formerly Chemistry Group, Bhabha Atomic Research Centre, Trombay, Mumbai 400 085, India

[2] Formerly The Advanced Centre for Treatment, Research and Education in Cancer (ACTREC), Tata Memorial Centre, Kharghar, Navi Mumbai, 410210, India

[3]Institute of Surface Modification, Permoserstrasse 15, D-04303 Leipzig, Germany

Email: tulsi.mukherjee@gmail.com

Abstract

Various one-electron oxidizing radicals generated pulse radiolytically viz., $^{\bullet}OH$, $Br_2^{\bullet-}$ $N_3^{\bullet}$, $NO_2^{\bullet}$, $NO^{\bullet}$ and $CCl_3OO^{\bullet}$ reacted with Ferulic acid at pH 7.5 mainly by decarboxylation and forming a transient having an absorption maximum at 350 nm. Rate constants for these reactions varied widely k *= 1.5 x 10^6 - 4 x 10^9 dm^3 mol^{-1} s^{-1}. $G(CO_2)$ = 2.2, was confirmed by gas chromatographic analysis of the irradiated solutions. In the case of reaction with $^{\bullet}OH$ radicals, at pH 7.5, we also observed a shoulder at ~ 420 nm which may be due to the formation of an $^{\bullet}OH$-adduct at the olefinic group. The rate constant for the addition of O_2 to this radical was measured to be* k *= 4.5 x 10^6 dm^3 mol^{-1} s^{-1}. At pH 10.5, one-electron oxidation of Ferulic acid by $^{\bullet}OH$, $Br_2^{\bullet-}$ and $N_3^{\bullet}$ resulted in the formation of a phenoxyl radical with l_{max} at ~ 530 nm and* k *= 3.7 - 5 x 10^9 dm^3 mol^{-1} s^{-1}. This 530 nm transient was able to oxidize 4-amino phenol,* k *= 4.5 x 10^8 dm^3 mol^{-1} s^{-1}. The $NO_2^{\bullet}$ and $NO^{\bullet}$ radicals seem to react differently. The oxidation potential of Ferulic acid at pH 7 and 10 as determined by cyclic voltammetry was 0.73 and 0.575 V* vs *NHE. Rate constant for the repair of tryptophanyl radical by Ferulic acid was 3.5 x 10^7 dm^3 mol^{-1} s^{-1}. The experimental observations and inferences are backed by appropriate theoretical calculations.*

Keywords: *Ferulic acid, Reactive Oxygen Species, Pulse Radiolysis*

Introduction

Phytochemicals derived from plants find wide application as food flavouring agents[1] while the polyphenols and phenolic derivatives of benzoic and cinnamic acids also occur naturally in plants and are widely used as dietary antioxidants.

Ferulic acid (**I,** scheme 1) (4-hydroxy-3-methoxycinnamic acid) is widely distributed in fruits and vegetables, where, as a result of bio-catalytic reaction it is converted to vanillic acid and proto-catecheuic acid[2, 3]. Graf [4] has reported that besides scavenging free radicals, it also finds use in cosmetic lotions for skin since it functions as a photo-protective agent. Numerous other studies[5-7] with hydroxy cinnamic acid and other antioxidants have revealed that they inhibit lipid oxidation. Meyer et al[5] have observed that the antioxidant action of ferulic acid in inhibiting oxidation of low density lipid (LDL) was greater than that offered by ascorbic acid.

Mainova and Yanishlieva[6] have observed that the antioxidant activity of cinnamic acid derivatives in inhibiting auto-oxidation of lard at 100°C was greater than that of benzoic acid derivatives.

Using time-resolved near IR phosphorescnce technique, the rate constants for the quenching of singlet oxygen for a range of hydroxycinnamic acids, determined in D_2O and acetonitrile solutions, showed that the quenching rate constant for caffeic acid was higher in D_2O than in acetonitrile solutions and was found to depend on the energy of the hydroxycinnamic acids / molecular oxygen charge transfer states[8].

The rate constants for the repair of the semi-oxidised 2¢-deoxy-adenosine monophosphate and 2¢-deoxy-guanosine monophosphate radicals[9] as well as for the ·OH-adducts of DNA[10] by hydroxy-cinnamic acids were determined by using pulse radiolysis technique. The *k* values for the electron transfer reactions ranged between $0.5 - 3 \times 10^9$ dm^3 mol^{-1} s^{-1}.

Literature is rife with references on the antioxidant action of various polyphenolic[11-15] and other synthetic or naturally occuring phenolic compounds[16-20] in scavenging reactive oxygen species or inhibiting lipid peroxidation. In contrast to this, little has been reported on the free radical scavenging action of cinnamic acid derivatives. In the light of this observation it was decided to investigate the redox and the kinetic characteristics of ferulic acid in scavenging various reactive oxygen species of interest from the biological point of view. We also extended our work to include the repair of tryptophanyl free radical by ferulic acid.

Materials and Methods

Ferulic acid, tert. butylhydroperoxide, methyl viologen and 4-amino phenol were all from (Sigma); tert. butanol (SISCO), potassium nitrite, Sodium hydroxide, Di-sodium hydrogen phosphate, Potassium di-hydrogen phosphate (Sarabhai Merck) and CCl_4 (E. Merck) were of GR or equivalent grade and were used as received. Immediately before experiments, solutions containing ferulic acid were made up in phosphate buffer using distilled water that was further purified by passing through a Thermolene's nanopure water purifying assembly. Solutions were purged with purified N_2O using syringe bubbling technique. Pulse radiolysis experiments were undertaken by utilising 50 ns single electron pulses of 7 MeV from the linear electron accelerator at BARC[21] along with the associated equipment for kinetic spectrophotometry and computer analysis of data. Dosimetry was carried out using 10^{-2} mol dm^{-3} air-saturated KSCN solution, taking $Ge[(SCN)_2^{\cdot-}]$[22] at 500nm to be = 21,520 dm^3 mol^{-1} cm^{-1}. The dose rate was ~ 10 Gy. / pulse.

Gas chromatographic analyses were performed with a Chemito-8510 unit equipped with a 200 x 0.3 cm^2 column containing porapak QS of 100-150 mesh maintained at room temperature, a sample injection port and a four filament thermal conductivity detector at ambient temperature. Helium was used as a carrier gas. To 5 ml of the irradiated aqueous solution containing 10^{-2} mol dm^{-3} ferulic acid and 1 x 10^{-3} mol dm^{-3} phosphate buffer, pH adjusted to 7.5, was added 0.25 ml of concentrated HCl. 0.1 ml of the gas present in 1 ml of void volume was drawn into a gas syringe and analysed by the gas chromatograph. Due to the partitioning of CO_2 gas between the aqueous and the gaseous phase, a pre-calibration was done by injecting different amounts of pure CO_2 gas to 5 ml of the aqueous buffered solution. The solution was acidified and the amount of CO_2 gas estimated in the void space above the aqueous solution. From the difference between the amount of CO_2 injected, and the estimated CO_2 in the void space after equilibration with the buffer solution, partitioning of CO_2 in the gas phase was estimated to be ~ 20 %. From this, the total CO_2 gas released following irradiation of ferulic acid solution was estimated.

Cyclic voltammetric data were recorded at a scan rate of 100 mV s^{-1} with a Princeton Applied Research universal potentiostat (model 273) electrochemical system. A three electrode cell comprising of a glassy carbon electrode (0.4cm^2 dia.) which was polished before each measurement in accordance with the procedure described earlier[23], a Ag / AgCl reference electrode and a Pt-wire

auxiliary electrode were used for all measurements. The experiments were performed in phosphate buffered solutions at 27° C, purged with purified N_2 for 5 mts. prior to scan runs. All measured potentials vs Ag / AgCl electrode were converted to those vs NHE by applying appropriate correction.

Computational Methods

To support our experimental results, quantum chemical calculations were done using Gaussian 98, Revision 9 [23] program by the Density Functional Theory (DFT) Hybrid B3LYP[24-26] methods. The equilibrium geometries of the structures investigated were optimized completely without any restriction. The standard basis set 6-31G(d) -was used and the atomic charges as well as the atomic spin densities were calculated using the Mulliken population analysis.

Results and Discussion

Generation of selective one-electron oxidants in N_2O-saturated aqueous solutions using pulse radiolysis technique have been shown by reactions 1 through 13 and have been dealt in detail elsewhere [23, 33]. The H• atoms were formed by reactions 1, and 14.

$$H_2O \xrightarrow{\sim\sim} {}^{\bullet}OH,\ H^{\bullet},\ e_{aq}^{-},\ H_2O_2,\ H_2,\ H_3O^{+} \quad (1)$$

$$e_{aq}^{-} + N_2 \xrightarrow{+H_2O} N_2 + {}^{\bullet}OH + OH^{-} \quad (2)$$

$${}^{\bullet}OH + Br^{-} \rightarrow Br^{\bullet} + OH^{-} \quad (3)$$

$$Br^{\bullet} + Br^{-} \rightarrow Br_2^{\bullet -} \quad (3a)$$

$${}^{\bullet}OH + N_3^{-} \rightarrow N_3^{\bullet} + OH^{-} \quad (4)$$

$${}^{\bullet}OH + NO_2^{-} \rightarrow NO_2^{\bullet} + OH^{-} \quad (5)$$

$$e_{aq}^{-} + NO_2^{-} \rightarrow NO_2^{\bullet 2-} \rightarrow NO^{\bullet} + OH^{-} \quad (6)$$

$${}^{\bullet}OH + (CH_3)_2\,CHOH \rightarrow (CH_3)_2{}^{\bullet}COH + H_2O \quad (7)$$

$$H^{\bullet} + (CH_3)_2\,CHOH \rightarrow (CH_3)_2{}^{\bullet}COH + H_2 \quad (8)$$

$$e_{aq}^{-} + CCl_4 \rightarrow {}^{\bullet}CCl_3 + Cl^{-} \quad (9)$$

$$CCl_4 + (CH_3)_2{}^{\bullet}COH \rightarrow {}^{\bullet}CCl_3 + (CH_3)_2CO \quad (10)$$

$${}^{\bullet}CCl_3 + O_2 \rightarrow CCl_3OO^{\bullet} \quad (11)$$

$$e_{aq}^{-} + (CH_3)_3COOH \rightarrow (CH_3)_3CO^{\bullet} + OH^{-} \quad (12)$$

$${}^{\bullet}OH + (CH_3)_3COH \rightarrow {}^{\bullet}CH_2(CH_3)_2COH + H_2O \quad (13)$$

$$e_{aq}^{-} + H^{+} \rightarrow H^{\bullet} \quad (14)$$

The transient UV-visible absorption observed with λ_{max} at 350 nm (Fig. 1) on pulse irradiating a N_2O-saturated solution containing 10^{-3} mol dm^{-3} ferulic acid and 10^{-3}

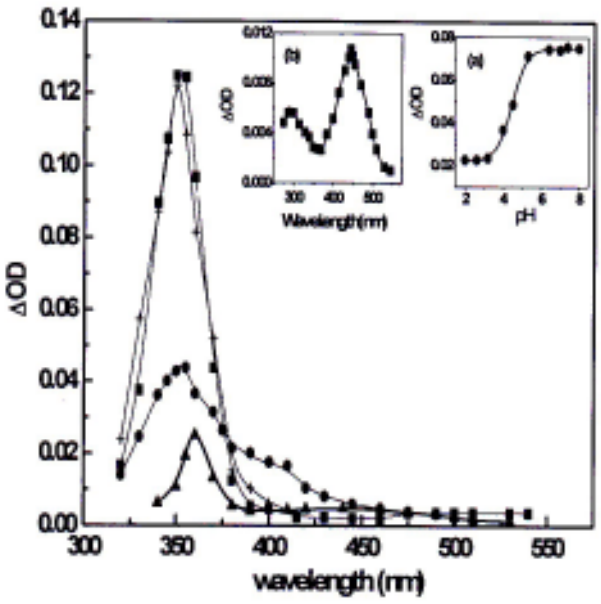

Fig. 1: Transient absorption spectra obtained on pulse radiolysis of N_2O-saturated aqueous solution pH 7.5 of ferulic acid (1 x 10^{-3} mol dm^{-3}), phosphate buffer (1 x 10^{-3} mol dm^3) at 30 ms after the pulse. Dose 10 Gy. (=) no scavenger, (<) 5 x 10^{-2} mol dm^{-3} NaN_3 pH 7.5, (+) 5 x 10^{-2} mol dm^{-3} KBr, (5) 5 x 10^{-2} mol dm^{-3} KCl pH 2.5, and air-saturated at 10 ms after the pulse. (inset) (a) $OD_{350\ nm}$ vs pH for the transient in a solution containing ferulic acid and KBr (air-saturated.) (b) Spectra obtained on pulse radiolysis of ferulic acid and 0.5 mol dm^{-3} tert. butanol, N_2-bubbled, pH 1.5.

mol dm^3 phosphate buffer (pH 7.5), may be attributed to the reaction of ·OH radicals (reactions 1, 2) with ferulic acid. The growth of the absorbance at 350 nm was attributed to the formation of a transient species and was exponential and first order in ferulic acid concentration. The bimolecular rate constant for the formation was calculated as, $k = 3.5 \times 10^9$ dm^3 mol^{-1} s^{-1}. This spectrum is comparable with the transient absorption spectrum obtained from the ·OH radical reaction with cinnamic acid and *p*-hydroxycinnamic acid having λ_{max} at 310 and 335 nm, respectively[34, 35]. A spectral shift to the longer wavelength (λ_{max} = 350 nm) in the case of ferulic acid is due to the presence of an additional electron donating $–OCH_3$ group in comparison to *p*-hydroxycinnamic acid.

From Fig 1 it can be seen that at pH £ 7.5 only a small absorption at 420 nm results on reaction of ·OH radicals with ferulic acid. This could be due to the ·OH radicals adding on to either the aromatic ring or to the olefinic part of Ferulic acid. If, ·OH radicals were to add on to the aromatic ring, one would expect the formation of a phenoxyl radical through loss of water molecule. In that case an absorbance around 530 nm should have been observed, as shall be seen later. Evidence for the formation of CO_2 was obtained in a separate experiment by carrying out gas chromatographic analysis following twenty repetitive electron pulses at a dose rate of 72 Gy / pulse to a Ferulic acid solution at pH 7.5. The elution time for CO_2 was » 4 min. after injection. It might be noted that the N_2O peak was observed at a latter time and the two peaks were well-resolved. These results matched perfectly with the calibration peaks obtained by injecting a mixture of pure N_2O and CO_2 gases. The total G (CO_2) released was 2.2. Decarboxylation reactions have been observed in the case of radiolysis of aqueous solutions of oxalic acid[36], phenylalanine[37], amino acids[38-40] and salicylic acid[41]. It can therefore be surmised that ·OH radicals bring about oxidative decarboxylation of Ferulic acid at pH 7.5 with the formation of the transient **II.**

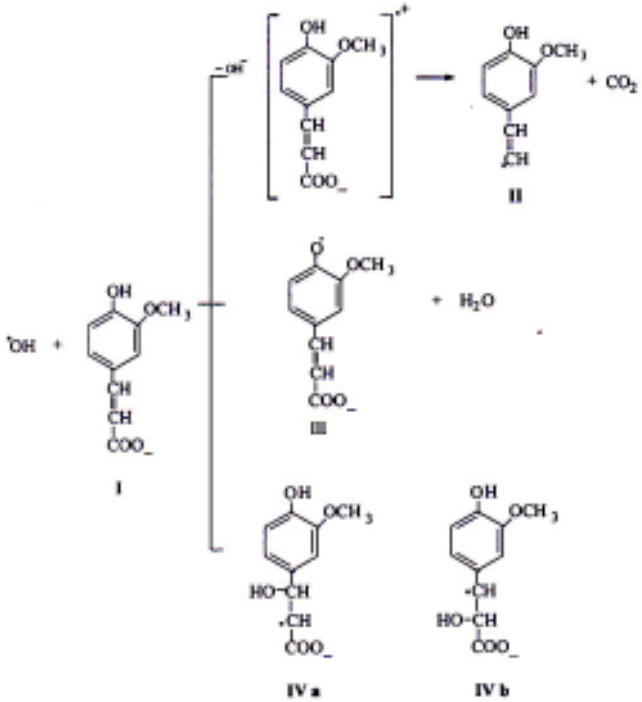

SCHEME I

The reducing nature of radical **II** was confirmed by its ability to transfer electron to the di-cation of methyl viologen[32] (MV^{2+}). We have followed the formation of ($MV^{·+}$) cation radical at 600 nm in solutions containing 2 x 10^{-3} mol dm^{-3} ferulic acid, 10^{-3} mol dm^{-3} phosphate buffer and 0.5 3 x 10^{-5} mol dm^{-3} methyl viologen at pH 7.5, on reduction by species II. The bi-molecular rate constant for the above reaction was found to be k = 1 x 10^9 dm^3 mol^{-1} s^{-1}. This channel accounts for only about 35% of the total (G (·OH) = 5.5).

In order to determine the possibility and the extent of formation of transient **III, (scheme I)** 0.5 – 5 x 10^{-5} mol dm^{-3} of 4-aminophenol ($E^1_{13.5}$ = 0.217 V and E^1_7 = 0.410 V vs NHE)[42] was added to N_2O-saturated solutions containing 2 x 10^{-3} mol dm^{-3} Ferulic acid, and 10^{-3} mol dm^{-3} phosphate buffer in the presence and absence of 0.5 mol dm^{-3} azide, pH 7.5 and tried to monitor the formation of the aminophenoxyl radical at 460 nm after pulse irradiating the solution. In the absence of any absorbance signals at this wavelength (pH 7.5), the existence of species III is somewhat doubtful.

In N_2O-saturated aqueous solutions at pH ~ 10.5, about 90% of the hydroxyl group of ferulic acid is expected to be in the de-protonated form and only ~ 5% of all the $^{\bullet}OH$ radicals exist as $O^{\bullet-}$. The transient absorption maximum formed on pulse-irradiating 1 x 10^{-3} mol dm^{-3} ferulic acid solution, shows a l_{max} at 530 nm and molar extinction coefficient e @ 750 dm^3 mol^{-1} cm^{-1}. This 530 nm absorption was attributed to the formation of Ferulic acid phenoxyl radical. A similar absorption at 530 nm was also observed for *p*-hydroxycinnamic acid[35]. However, we could not observe another absorption maximum around 600 nm, which could be of any significance. The value of the formation rate constant was found to be 5 x 10^9 dm^3 mol^{-1} s^{-1}.

The oxidizing ability of this transient was confirmed by adding incremental amounts of 4-aminophenol to a N_2O-saturated solution containing Ferulic acid and phosphate buffer (pH 10.5) in the presence and absence of azide ions and monitoring the absorption from 4-aminophenoxyl radical at 460 nm (Fig. 2).

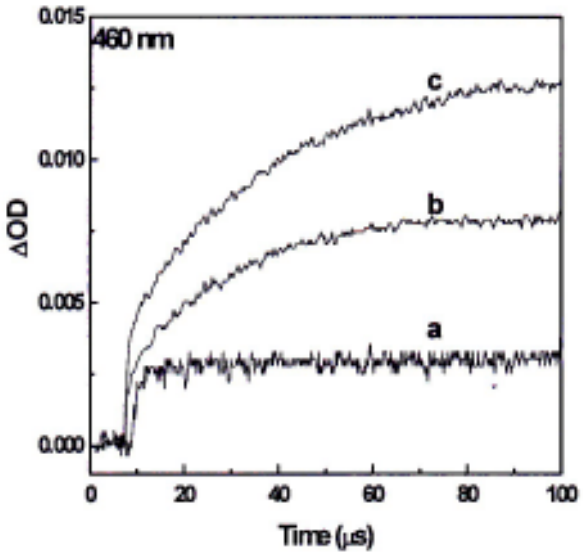

Fig. 2: Formation of the transient 4-amino phenoxyl radical at 460 nm on pulsing a solution containing, 0.5 mol dm^{-3} mol dm^{-3} azide, 2 x 10^{-3} mol dm^{-3} Ferulic acid, and 10^{-3} mol dm^{-3} phosphate buffer N_2O-saturated, pH 10.5 (a) in the absence of 4-aminophenol (b) in the presence of 1.2 x 10^{-5} mol dm^{-3} 4-aminophenol (c) in the presence of 2.5 x 10^{-5} mol dm^{-3} 4-aminophenol.

Rate constant for this radical was k = 4.5 x 10^8 dm^3 mol^{-1} s^{-1} and was in fair agreement with the 'k' value derived from the decay of the 530 nm transient k = 3 x 10^8 dm^3 mol^{-1} s^{-1}. This transient was also observed on pulse-irradiating a N_2O-saturated solution of 4-aminophenol at pH10.5. Figure 3 shows transient absorption spectrum with l_{max} at 530 nm, formed by the reaction of $Br_2^{\bullet-}$ / $N_3^{\bullet}$ radicals with 10^{-3} mol $dm^{-3}$of Ferulic acid (pH 10.5). Two additional very weak bands, having l_{max} at ~ 400 and 650 nm were seen for the reaction of the azide radical with the substrate. It may be noted that a similar spectrum was also observed in the case of $^{\bullet}OH$ radical reaction with the substrate at this pH. The rate constant values (Table 3) suggest that electron transfer occurs from the phenoxide anion to the oxidant ($^{\bullet}OH$, $Br_2^{\bullet-}$ and $N_3^{\bullet}$).

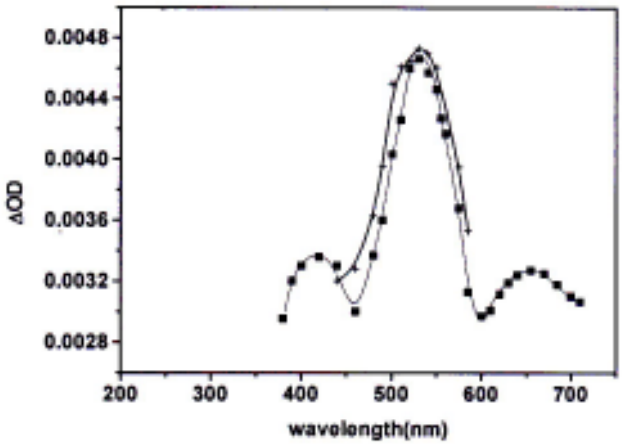

Fig. 3: Transient absorption spectra obtained at 30 ms after the pulse, during pulse radiolysis of N_2O-saturated aqueous solution containing 1 x 10^{-3} mol dm^{-3} Ferulic acid and 1 x 10^{-3} mol dm^{-3} phosphate buffer, pH 10.5. (Dose 10 Gy.) (<) 5 x 10^{-2} mol dm^{-3} NaN_3, at 30 ms after the pulse, (+)1 x 10^{-3} mol dm^{-3} Ferulic acid and 5 x 10^{-2} mol dm^{-3} KBr,

The transient with l_{max} at 350 mn was quite stable and did not show any significant decay even after 2 ms. The presence of varying concentrations of oxygen did not in any manner alter its decay rate. On the other hand, it was seen that the decay rate of the transient absorbing at 420 nm became faster on addition of O_2 (k = 4.5 x 10^6 dm^3 mol^{-1} s^{-1}) indicating that this could be either transient **III a,** or **III b** (scheme I).

Inset (**b)** in Fig 1 shows the transient absorption spectrum, formed due to the reaction of H atoms with 10^{-3} mol dm^{-3} ferulic acid in N_2-bubbled solutions at pH 1.5 after all the ·OH radicals were scavenged by tert. butanol, with a l_{max} centered at 450 nm, and, slightly red-shifted by ~ 25 nm in comparison to that observed for *p*-hydroxycinnamic acid[35]. This should be expected due to the reason mentioned above. Bobrowski and Raghavan[34] have mentioned that ~85% of H atoms react at the olefinic moiety of Cinnamic acid. We expect the same to be true in the case of Ferulic acid.

Theoretical Parameters

To test the influence of the polarized continuum on molecular structure the geometry optimization was also made in water (e=78) using the Self-Consistent Reaction Field (SCRF) Onsager (SCRF=Dipole) model[27]. The calculated Mulliken charges in water and spin density distributions were also compared with solvent effect taken into account with Tomasi's Polarized Continuum Model (SCRF=PCM)[28, 29]. This method uses more realistic shape of cavity made in solvent than SCRF=Dipole, but does not take into account possible changes in the molecular geometry. Testing of the influence of the solvent on geometrical parameters is important especially for the structures with large dipole moment and in the cases of different OH-adduct radicals, where molecular geometry is no more planar and geometry distortions are significant. By SCRF=Dipole method, molecular geometries were optimized in water and the SCRF=PCM method was used for vacuum geometries. The comparison of vacuum and water geometries show only a relatively small change of bond lengths and valence angles. The maximal changes of 0.012° A for interatomic distances and 1.4° for angles were observed for FA anion which has very large dipole moment (23 Debye in vacuum). Both methods viz., SCRF=Dipole and SCRF=PCM show qualitatively similar (within 10%) charge and spin density distributions for FA cation radical in water. So, only SCRF=PCM calculated results are shown in Table.1.

Quantum Chemical Parameters

To analyse quantum chemical transformations of Ferulic acid-anion we have investigated three possible reaction channels (scheme 1). The first channel is the formation of the vinyl radical (II). The electron transfer from highest occupied molecular orbital (HOMO) of Ferulic acid-anion to single occupied molecular orbital (SOMO) of ·OH can be effective because of favourable energy difference (about 3 eV) between MO's of the reaction partners. If the Ferulic acid radical is built, both the vinyl radical (II) and phenoxyl radical (III) are in question. Here it is interesting to compare the transformation of Ferulic acid-anion and substituted styrene. Whereas in substituted styrene the electron from HOMO is distributed through the whole molecule the electron from HOMO of Ferulic acid-anion is localized mainly on the carboxylate anion (*i.e.*, COO^-). The changes in atomic charges by electron transfer process show the distribution of positive charge in the molecule. It is also shown[30, 31] that stability of the cation radicals from various phenolic compounds correlate with changes of atomic charge on OH-group and absolute values of atomic spin on the phenolic oxygen. The larger is the change in the charge on OH- group and atomic spin on oxygen, the faster is the deprotonation from OH-group. As calculated, in the substituted styrene cation radical, positive atomic charge and spin density are distributed through the whole molecule with relatively large change of atomic charge on OH (+0.157e) and absolute values of atomic spin on oxygen (0.136). As calculated, the substituted styrene–phenoxyl radical is up to 35 kcal mol^{-1} more stable than substituted styrene –vinyl radical.

On the contrary, in Ferulic acid radical the spin density is strongly localised on COO^- group. Additionally, the difference of the Mulliken atomic charges between the anion ground state and radical shows that about 71% (85% at Onsager SCRF=Dipole method) of the positive charge is on the olefinic moiety and only 3% (1% at SCRF=Dipole) on OH group of ferulic acid. From frontier orbital theory, strong localisation of positive charge and atomic spin indicate that the olefinic moiety is the reactive part of the molecule and the existence of vinyl radical (II) is thus advocated. This result agrees also with the calculated reaction enthalpy (-6.8 kcal mol^{-1})

of formation from radical II. The calculated Mulliken charges of selected atoms for singlet anion and radical cation of Ferulic acid in water (Tomasi's SCRF=PCM model) in comparison with those of the vinyl type free radical and the substituted styrene can be seen in Table 2.

The results of calculations of reaction parameters by the formation of phenoxyl radical III and ·OH-adduct radicals IV are shown in Table 1. All these reactions are energetically allowed. If we compare different models of ·OH-adduct radicals, it can be seen that addition on double the bond is energetically more favourable than addition on the ring. As calculated, (radical IV b) is about 5 kcal mol^{-1} more stable than radical IV a.

Oxidation of Ferulic acid at pH 7.5 with more specfic one-electron oxidants, such as $Br_2^{\bullet-}$, $N_3^{\bullet}$ (formed through reactions 1-4) from a N_2O-saturated solution containing 1 x 10^{-3} mol dm^{-3} Ferulic acid and 5 x 10^{-2} mol dm^{-3} KBr or NaN_3, yielded a transient absorption spectrum with an absorption maximum at 350 nm (Fig 1) and a mean molar extinction coefficient **e** @ 21,300 dm^3 mol^{-1} cm^{-1}. Rate constant '*k*' for the above reactions ranged between 1.4 – 4 x 10^9 dm^3 mol^{-1} s^{-1} (table 3). In the case of azide radical reaction, '*k*' was obtained from the formation traces at 350 nm using different solute concentrations. On the other hand, rate constant for the $Br_2^{\bullet-}$ reaction with Ferulic acid was determined from the first order decay rates *k*¢ of $Br_2^{\bullet-}$ observed at 360 nm *vs* [Ferulic acid]. The presence of CO_2 gas in the post-irradiated samples confirms our statement made above that oxidation of Ferulic acid at neutral pH results in decarboxylation with the formation of the transient **II.** We believe that the difference in assigning the nature of transient species by Bobrowski and Raghavan[34] and Bobrowski[35] especially at lower pH is primarily due to the fact that they have arrived at their conclusions mainly from ·OH radical reaction.

The $HO_2^{\bullet}$ radicals formed on pulse radiolysis of O_2-saturated aqueous solutions (pH 2.5) containing 1 mol dm^{-3} tert. butanol as ·OH radical scavenger, do not seem to react with 10^{-3} mol dm^{-3} Ferulic acid in the 300-400 nm region. Hence, when O_2–saturated aqueous solutions of 10^{-3} mol dm^{-3} Ferulic acid and 0.5 mol dm^{-3} KCl (pH ~ 2.5) were pulse-irradiated, the $Cl_2^{\bullet-}$ radicals formed, in a manner similar to that of $Br_2^{\bullet-}$, react with Ferulic acid to give a very weak absorption maximum at ~ 360 nm (Fig. 1).

By proper selection of various solute concentrations the trichloromethyl peroxyl radicals (reactions 1, 7-11) formed in O_2-saturated solutions, and also the tert. butoxyl radicals (reactions 1 and 13) generated were seen to react with Ferulic acid at pH 7.5. Rate constant for the $CCl_3OO^{\bullet}$ radical reaction with Ferulic acid was 1.2 x 10^8 dm^3 mol^{-1} s^{-1}. This value is in fair agreement with the rate constant values reported for other aromatic compounds[43]. Rate constant for the reaction of the tert. butoxyl radical with the antioxidant was 1 x 10^9 dm^3 mol^{-1} s^{-1}.

When an aqueous solution containing 0.5 mol dm^{-3} $NaNO_2$ and 10^{-3} mol dm^{-3} Ferulic acid at pH 7.5 was saturated with N_2O and pulse-irradiated, reactions 1, 2 and 5 occur. We observed a transient absorption spectrum (Fig 4) with l_{max} at ~ 350 nm which is due to the reaction of the $NO_2^{\bullet}$ radicals with Ferulic acid. The build-up of this transient, though exponential with time, was rather slow and was observed only at longer time scale. On monitoring the k_{obs} values at this wavelength for different antioxidant concentrations, a linear plot with *k* = 1.5 x 10^6 dm^3 mol^{-1} s^{-1} was obtained.

Pulse-irradiation of an aqueous N_2-bubbled solution containing 0.5 mol dm^{-3} $NaNO_2$, and 0.5 mol dm^{-3} tert. butanol at pH 7.5 resulted in the formation of $NO^{\bullet}$ radicals vide reaction 6. In the additional presence of 10^{-3} mol dm^{-3} Ferulic acid, an absorption maximum was observed at 350 nm which is as a result of $NO^{\bullet}$ radicals reacting with the antioxidant (Fig. 4). The rate constant for this reaction was, k = 3.5 x 10^6 dm^3 mol^{-1} s^{-1}. The low rate constant values in the case of $NO_2^{\bullet}$ and $NO^{\bullet}$ radical reactions, reflect on incomplete reactions.

In earlier studies on Cinnamic acid[34] and *p*-hydroxycinnamic acid[35] it was observed that ~ 85 % of

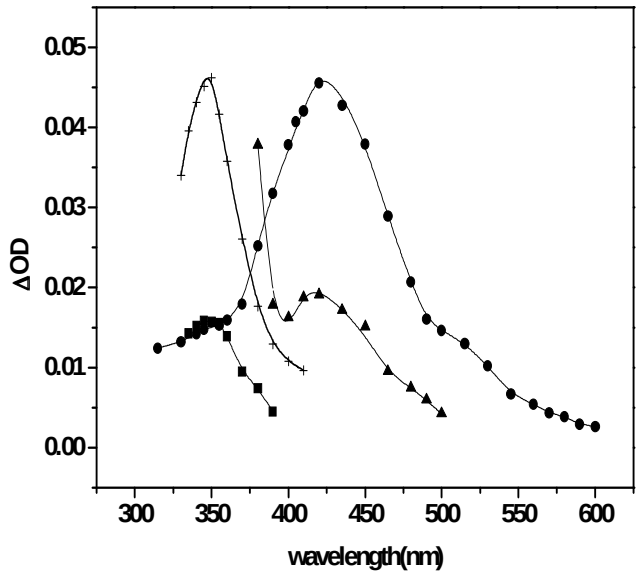

Fig. 4: Transient absorption spectra obtained during pulse radiolysis of a solution containing 1 x 10^{-3} mol dm^{-3} ferulic acid, 1 x 10^{-3} mol dm^{-3} phosphate buffer, and (+), 5 x 10^{-2} mol dm^{-3} $NaNO_2$, N_2O-saturated at pH 7.5, at 1400 μs after the pulse,. (■) 5 x 10^{-2} mol dm^{-3} $NaNO_2$, and 0.5 mol dm^{-3} tert. butanol, N_2-bubbled pH 7.5, at 1600 μs after the pulse,. (●) 5 x 10^{-2} mol dm^{-3} $NaNO_2$, N_2O-saturated, pH 10.5, at 1550 μs after the pulse, (▲) 5 x 10^{-2} mol dm^{-3} $NaNO_2$, 0.5 mol dm^{-3} tert. butanol, N_2-bubbled, pH 10.5, at 1650 μs after the pulse, (Dose 10 Gy.).

·OH radicals react at the olefinic part of the substrate resulting in benzyl type of radicals and the pK_a was as a consequence of the protonation /deprotonation of these benzyl-type of radicals formed on the addition of ·OH radicals to the olefinic groups. However, our studies with other one-electron oxidants at pH 7.5, where the phenolic group of the antioxidant is unionized, and also from the spectral and kinetic data obtained by the reaction of various one-electron oxidants with Ferulic acid at pH 7.5 (ground state pK_{a1} of Ferulic acid = 4.25 ± 0.1 and pK_{a2} = 9.4 ± 0.1, this study) shows that in all probability, electron transfer takes place from the carboxylate group of the substrate resulting in decarboxylation of the antioxidant and formation of the transient **II.** Rather very poor absorbance observed in the case of $Cl_2^{\cdot-}$ radical reaction with Ferulic acid at pH 2.5 and also the absence of any changes in the spectrum at pH = 2.5 probably points to the fact that at this pH the carboxylic group of the substrate is present mostly in the unionized state, thus electron transfer is not favoured. In order to check this we plotted the change in absorbance with pH over the range 2 – 8.5, after pulse irradiating O_2–saturated aqueous solutions of 10^{-3} mol dm^{-3} Ferulic acid and 0.5 mol dm^{-3} KBr. A sigmoidal curve was obtained (inset a, Fig 1) with pK_a = 4.4 ± 0.1 and is in fair agreement with the ground state pK_{a1} of Ferulic acid. We therefore have reason to believe that decarboxylation of the semi-oxidised Ferulic acid is the most favoured mechanism. In the case of ·OH radical reaction at pH 7.5 the small amount of absorption at ~420 nm may be due to a small amount of adduct formation at the olefinic part of the antioxidant.

At pH 10.5 the l_{max} of the transient formed by $NO_2^{\cdot}$ and NO· radical reaction with Ferulic acid shifted to 420 nm (Fig.4) indicating that the reaction was occuring at the olefinic part of the antioxidant rather than from the phenoxide anion, since, in that case one would have seen an absorbance at 530 nm at a longer time scale. The reason for this change seems to be unclear. The lower rate constant values for the reaction of $NO_2^{\cdot}$ and NO· radicals with Ferulic acid at pH 7.5 and 10.5 signify incomplete reaction.

Table 3 summarises the kinetic and spectroscopic data of interest for the reaction of various one-electron oxidants with Ferulic acid.

Repair of the tryptophanyl radicals

Jiang et al [9, 10] have studied the repair of the semi-oxidised 2′- deoxy-adenosine monophosphate and 2′-deoxy-guanosine monophosphate radicals [9] as well as for the ·OH-adducts of DNA[10] by sinapic, p-coumaric, and ferulic acids using pulse radiolysis technique. They have reported that the repair rate of various hydroxy cinnamic acids lie in the range of 5 – 30 x 10^8 dm^3 mol^{-1} s^{-1} and these values seem to be quite reasonable.

We have pulse radiolytically generated the tryptophanyl radical with l_{max} of 510 nm in aqueous solutions of pH 7, using N_2O-saturated 0.2 mol dm^{-3} KBr, and 10^{-2} mol dm^3 tryptophan In the additional presence of 0.7-3 x 10^{-4} mol dm^3 ferulic acid the decay of this transient be-

came faster. By plotting the first order decay rates against [ferulic acid], the rate constant for the repair of tryptophanyl radical was found to be 3.5 x 10^7 dm^3 mol^{-1} s^{-1}, which is twice that for the repair of the tryptophanyl radical by uric acid[44].

Reduction Potential

In order to get a correct reduction potential value, we have carried out determination of this potential using cyclic voltammetric method. About 25 ml of an aqueous solution containing 0.2 mol dm^{-3} KCl, 10^{-3} mol dm^{-3} phosphate buffer and 10^{-3} mol dm^{-3} Ferulic acid at pH 7 or 10 were de-aerated by passing N_2 gas for 5 minutes prior to measurement, in an electrochemical cell described earlier[23]. Only one anodic peak was observed during the forward scan at pH 7, as well as at pH 10 and the measured potential values at the two respective pHs being E^1_7 = 0.730 V and E^1_{10} = 0.575 V *vs* NHE. No peak was obtained during the reverse scan, indicating that the oxidation products undergo either fast electrode reaction or dimerise. The above reduction potential value at pH 7 was higher by about 40 mV than that reported by Lin *et.al*.[45] These authors have used pulse radiolysis technique employing 4-methoxy phenol as a reference redox standard to measure the reduction potential and the value will thus vary, depending on how accurately the potential of the reference is determined. The lower reduction potential value at pH 10 shows the ease of oxidation that the antioxidant can undergo.

Conclusions

Our pulse radiolysis studies show that the primary attack by one-electron oxidants such as $^{\bullet}OH$, $Br_2^{\bullet-}$, $N_3^{\bullet}$, $NO_2^{\bullet}$, $NO^{\bullet}$ and $CCl_3OO^{\bullet}$ radicals on Ferulic acid at pH 7.5 does not result in the formation of the phenoxyl radical of Ferulic acid as usually observed with other phenolic and substituted phenolic compounds. But, it tends to undergo decarboxylation along with the concomitant formation of a carbon-centered reducing radical. We have no evidence to account for the other possible species formed at pH 7.5. On the other hand, at pH 10.5 the electron transfer from Ferulic acid to $^{\bullet}OH$, $Br_2^{\bullet-}$ and $N_3^{\bullet}$ radicals takes place from the phenolate group and the phenoxyl radical formed in the process has oxidizing ability. The $NO_2^{\bullet}$ and $NO^{\bullet}$ radicals seem to add on to the olefinic part of Ferulic acid.

Acknowledgements

The authors wish to thank Dr. T.N. Das for useful discussions and Mr. V.N. Rao for maintenance of the LINAC facility.

Table 1. B3LYP/6-31G(d) calculated changes of Mulliken charges (DQ, electron) and spin densities (S) on selected atoms, DH (kcal mol^{-1}) - reaction enthalpies of formation of different radical structures formed from FA and considered in the reaction of $^{\bullet}OH$ radicals with ferulic acid anion *in aqueous phase* (Tomasi's SCRF=PCM model). DE-relative stability

Structure	Parameter	Ferulic Acid	Substituted Styrene
Ferulic Acid (cation radical)	$\Delta Q(OH)$ $\Delta Q(C_2O)$ $S(O)$ $S(C_2O)$	+0.032 +0.712 0.004 1.053	+0.157 - 0.136 -
II (vinyl radical)	ΔH	-6.8	ΔE=+35 kcal mol^{-1}
III (phenoxyl radical)	ΔH	-33.1	ΔE=0 kcal mol^{-1}
IV a) ($^{\bullet}OH$-adduct)	ΔH	-32.9	-
IV b) ($^{\bullet}OH$-adduct)	ΔH	-37.8	-
$^{\bullet}OH$-adduct on the aromatic ring	ΔH	-20.1	-

Table 2. B3LYP/6-31G(d) calculated Mulliken charges of selected atoms for singlet anion and radical cation of ferulic acid in water (Tomasi's SCRF=PCM model) in comparison with those of substituted styrene and vinyl type free radical.

Atom	Ferulic Acid Singlet Anion	Ferulic Acid Radical Cation	Substituted Styrene Vinyl type free radical	Substituted Styrene Singlet	Substituted Styrene Radical Cation
1 C	0.289	0.306	0.294	0.306	0.371
2 C	0.348	0.351	0.342	0.350	0.402
3 C	- 0.291	- 0.271	-0.283	-0.263	- 0.247
4 C	0.151	0.134	0.148	0.171	0.174
5 C	- 0.241	- 0.223	-0.238	-0.210	- 0.173
6 C	- 0.198	- 0.197	-0.196	-0.170	- 0.153
7 C	- 0.185	- 0.162	-0.200	-0.117	- 0.311
8 C	- 0.234	- 0.226	-0.241	-0.359	- 0.571
9 O	- 0.681	- 0.666	-0.677	-0.650	- 0.146
H(O)	0.453	0.470	0.458	0.425	0.503
10 C	0.514	0.559	-	-	-
11 O	- 0.690	- 0.356	-	-	-
12 O	-0.709	-0.376	-	-	-

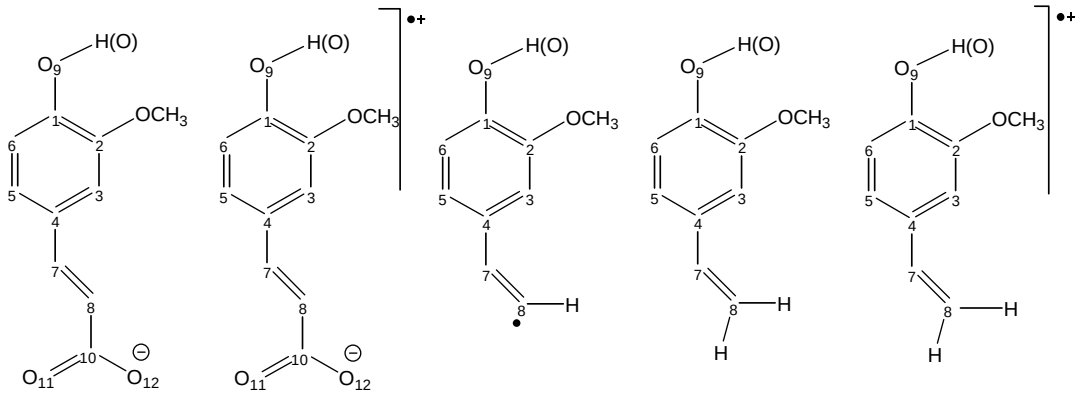

References

1. Coutis, E., Ho, C-T., Mmussinau, C.J. and Parliament, P.H. In*: Food flavours: Formation Analysis Packing Influences:* Developments in Food Science, Proc.9th Intl. Conf. 1-4 July, 1997.
2. Rosazza, J.P.N., Huang, Z.X., Dostal, L. and Rousseau, B., 1995, *J. Indl. Microbiol.*, **15,** 457.
3. Huang, Z.X., Dostal, L., Rosazza, J.P.N., 1993, *J. Biol. Chem.*, **268,** 23954.
4. Graf, E., 1992, *Free Rad. Biol. Med.*, **13,** 435.
5. Castelluccio, C. Bollwell, G.P., Gerrish, C. and Rice-Evans, C., 1996, *Biochem. J.* **316**, 691.
6. Yanishlieva, N.V. and Mainova, E.M., 1992, *Fett Wissenschaft Technologie*, **94,** 374 and 428.
7. Meyer, A.S., Donovan, J.L. and Pearson, D.A., 1998, *J. Agri.Fd. Chem.*, **46,** 1783.

Table 3: Kinetic and spectroscopic data for the reaction of one-electron oxidants and reductants with ferulic acid

Reactions	pH	λ_{max} (nm)	Molar Extinction Coefficient($\boldsymbol{\varepsilon}$) ± 100 ($dm^3\ mol^{-1}\ cm^{-1}$)	Rate constant ($\boldsymbol{k}$ x 10^{-8}) ($dm^3\ mol^{-1}\ s^{-1}$)
$^{\bullet}OH$ + FA	7.5	350	8,800	35.0
	7.5	420	8,700	
$^{\bullet}OH$ + FA	10.5	530	750	50.0
$Br_2^{\bullet-}$ + FA	7.5	350	21,000	1.4
$Br_2^{\bullet-}$ + FA	10.5	530	750	-
$N_3^{\bullet}$ + FA	7.5	350	21,500	40.0
$N_3^{\bullet}$ + FA	10.5	530	750	37.0
$CCl_3OO^{\bullet}$ + FA	7.5	350		1.2
$(CH_3)_3CO^{\bullet}$ + FA	7.5	350		10.0
$NO_2^{\bullet}$ + FA	7.5	350	7,950	0.015
$NO_2^{\bullet}$ + FA	10.5	430	7,950	0.025
$NO^{\bullet}$ + FA	7.5	350	5,100	0.035
$NO^{\bullet}$ + FA	10.5	430	6,350	0.045

8. Foley, S., Navaratnam, S., McGarvey, D.J., Land, E.J., Truscott, T.G. and Rice-Evans, C., 1999, *Free Rad. Biol. Med.*, **26,** 1202.

9. Jiang, Y., Lin, W.-Z., Yao, Si-de., Lin, N.-yun., Zhu and Da-Yuan., 1999, *Radiat. Phys. Chem.*, **54,** 349.

10. Jiang, Y., Lin, W.-Z., Yao, Si-de., Lin, N.-yun and Zhu, Da-Yuan, 1999, *Radiat. Phys. Chem.*, **54,** 355.

11. Jovanovic, S.V., Steenken, S., Hara, Y., Simic, M.G., 1996, *J. Chem. Soc. Perkin Trans.*, **2,** 2497.

12. Jovanovic, S.V., Steenken, S., Tosic, M., Marjanovic, B. and Simic, M.G., 1994, *J. Am. Chem. Soc.*, **116,** 4846.

13. Salah, N., Miller, N.J., Paganga, G., Tijburg, L., Bolwell, G.P. and Rice-Evans, C., 1995, *Arch. Biochem. Biophys.*, **322,** 339.

14. Rice-Evans, C., Miller, N.J. and Paganga, G., 1996, *Free Rad. Biol. Med.*, **20,** 933.

15. Bors, W., Heller, W., Michel, C. and Stettmaier, 1996, K. In Handbook of Antioxidants, Cadenas, E., Packer, L. Eds., Marcel Dekker: New York, p409.

16. Aeschbach, R., Löliger, J., Scott, B.C., Murcia, A., Butler, J., Halliwell B. and Aruoma, O.I., 1994, *Food. Chem. Toxic.*, **32,** 31.

17. Cuvelier, M-E., Richard, H. and Berset. C., 1992, *Biosci. Biotech. Biochem.*, **56,** 324.

18. Chimi, H., Cilard, J., Cillard, P. and Rahmani, M., 1991, *J. Am. Oil Chem. Soc.* **68,** 307.

19. Giese, J., 1996, *Food. Tech.* **65,** 73.

20. Packer, L. and Fuchs, J., 1997, Handbook of Synthetic Antioxidants. Marcel Dekker: New York, pp441.

21. Mukherjee, T., 1997, In: Atomic, Molecular and Cluster Phys., Ahmad, S.A. Ed. Narosa, New Delhi, p299.

22. Fielden, E.M., 1982, In: The study of fast processes and Transient Species by Electron Pulse Radiolysis, Reidel, Dordrecht, Holland, p49.

23. Mahal, H.S., Sharma, H.S. and Mukherjee, T. 1999, *Free Radical Biol. Med.*, **26,** 557.

24. Gaussian 98, Revision A9, Frisch, M.J., Trucks, G.W., Schlegel H.B., Scuseria G.E., Robb M.A., Cheeseman J.R., Zakrzewski V.G., Montgomery J.A. Jr., Stratmann R.E., Burant J.C., Dapprich S., Millam J.M., Daniels A.D., Kudin K.N., Strain M.C., Farkas O., Tomasi J., Barone V., Cossi M., Cammi R., Mennucci B., Pomelli C., Adamo C., Clifford S., Ochterski J., Petersson G.A., Ayala P.Y., Cui Q., Morokuma K., Malick D.K., Rabuck A.D., Raghavachari K., Foresman J.B., Cioslowski J., Ortiz J.V., Baboul A.G., Stefanov B.B., Liu G., Liashenko A., Piskorz P., Komaromi I., Gomperts R., Martin R.L., Fox D.J., Keith T., Al-Laham M.A., Peng C.Y., Nanayakkara A., Gonzalez C., Challacombe M., Gill P.M.W., Johnson B., Chen W., Wong M.W., Andres J.L., Gonzalez C., Head Gordon M., Replogle E.S. and Pople J.A., 1998, Gaussian, Inc., Pittsburgh PA.

25. Axel D. Becke., 1993, *J. Chem. Phys*., **98,** 5648.

26. Axel D. Becke., 1996, *J. Chem. Phys.*, **104,** 1040.

27. Chegteh Lee, Weitao Yang, Robert G. Parr., 1987, *Physical Review* B, **37,** 785.

28. Wong M.W., Frisch M.J. and Wiberg K.B., 1991, *J. Am. Chem. Soc.*, **113,** 4776.

29. Miertuš S., Scrocco E. and Tomasi J., 1981, *Chem. Phys*., **55,** 117.

30. Miertuš S. and Tomasi J., 1982, *Chem. Phys*., **65,** 239.

31. Hermann R., Naumov S. and O. Brede, 2000, *J. of Molec. Structure (Teochem),* **532,** 69.

32. Mahalaxmi G.R., Hermann R., Naumov S. and Brede O., 2000, *Phys. Chem. Chem. Phys.*, **2,** 4947-495.

33. Mahal, H.S. and Mukherjee, T., 1999, *Radiat. Phys. Chem.,* **54,** 29.

34. Bobrowski, K. and Raghavan, N.V., 1982, *J. Phys. Chem.,* **86,** 4432.

35. Bobrowski, K., 1984, *J. Chem. Soc. Farad. Trans., I,* 1377.

36. Draganic, I. G. and Gal, O., 1971, *Radiat. Res. Rev.*, **3,** 167.

37. Wang, D.G., Schuchmann, H.P. and von Sonntag, C., 1993, *Zeitschrift fur Naturforschung B,* **48,** 761.

38. Monig, J., Chapman, R. and Asmus, K-D., 1985, *J. Phys. Chem.,* **89,** 3139.

39. Bonifacic, M., Stefanic, I., Hug, G.L., Armstrong, D.A. and Asmus, K-D., 1998, *J. Am. Chem. Soc.*, **120,** 9930.

40. Bobrowski, K., Hug, G.L., Marciniak, B. and Kozubek, H., 1994, *J. Phys. Chem.*, **98,** 537.

41. Amphlett, C.B., Adams, G.E. and Michael, B.D., 1968, In: Radiation Chemistry-1, Advances in Chemistry, Series-81 (ed.), Gould, R.F., 231.

42. Steenken, S. and Neta, P., 1982, *J. Phys. Chem.*, **86,** 3361.

43. Neta, P., Huie, R.E. and Ross, A.B., 1990, *J. Phys. Chem., Ref. Data.*, **19,** 413.

44. Butler, J. and Hoey, B.M., 1984, *Biochem.Biophys. Acta*, **791,** 212.

45. Lin, W., Navaratanam, S., Yao, S. and Lin, N., 1998, *Radiat. Phys. Chem.,* **53,** 425.

Conference Alerts

1) 21st International Conference on Materials, Methods and Technologies,
Organized by Bulgarian Academy of Sciences
July 1-5, 2019, Burgas, Bulgaria
Website: www.sciencebulgaria.org
Enquiries: office@sciencebg.net

2) 2nd International Conference on Green and Sustainable Chemistry
Theme; Research at the interface of Chemistry and Sustainability
July 15-16, 2019, Zurich, Switzerland
Website: https://meetingsint.com/conferences/green-chemistry
Enquiries: greenchem@insightsummits.com

3) 5th International Congress on Water, Waste and Energy (WWEM-19)
July 22-24, 2019, Paris, France
Website; http://waterwaste-19.com/

4) 13th Budapest International Conference on Chemical, Agricultural, Environmental and Biological Sciences (BCAEBS-19)
July 22-24, 2019, Budapest, Hungary
Website: http://caebs.eacbee.org/

5) International Conference on Green Energy and Environmental Technology (GEET-19)
July 24-26, 2019, Prais, France
Website: https://geet-19.com/

6) 2nd World Congress on Drug Discovery and Development 2019
July 25-26, 2019, Bangkok, Thailand
Website: http://drugdiscoverycongress.com/

7) 8th Congress on Analytical Chemistry and Mass Spectrometry
Theme: Utilizing the latest developments in Mass spectrometry and Proteomics
July 29-30, 2019, Bangkok, Thailand
Enquiries: massspectrometry@annualmeetings.net

8) 15th International Conference on Environmental Chemistry and Engineering
August 15-16, 2019, Rome, Italy
Enquiries: environmentalchemistry3@gmail.com
Environmentalchemistry2019@protonmail.com

9) 14th Istanbul International Conference on Chemical, Agricultural and Biological Sciences (ICABS-2019)
September 17-19, 2019, Istanbul, Turkey
Website: http://cabs.eacbee.org/

10) 7th Asian Conference of Coordination Chemistry (ACCC-7)
October 15-18, 2019, Kuala Lumpur, Malaysia
Website: https://accc7.org.my/
Enquiries: accc7@ikm.org.my

11) 6th Industry Green Chemistry World (IGCN 2019)-Convention and Ecosystem
October 16-17, 2019, IIT-Bombay, Mumbai, India
Website: www.industrialgreenchem.com

12) 2nd International Conference on Advanced Nanomaterials and Nanodevices
October 23-25, 2019, Shanghai, China
Website: http.//www.icannd.org/

13) 8th International Conference on Chemical Science and Engineering (ICCSE2019)
November 18-20, 2019, Taipei, Taiwan
Website: http://www.iccse.org/

14) International Conference on Phosphorus, Boron and Silicon(PBSI-2019)
December 2-4, 2019, Rome, Italy
Website:http://premc.org/conferences/pbsi-phosphorus-boron-silicon/

RNI - No. MAHENG / 2017 / 74063
VOLUME 3 (Issue 1) July - Dec 2019

ISSN No. 2561-5911
BI-ANNUAL SUBSCRIPTION : Rs. 2000/-

G P GLOBALIZE RESEARCH JOURNAL OF CHEMISTRY

VOLUME 3 (Issue 1) July - December 2019
BI-ANNUAL 2019

GAURANG PUBLISHING

GAURANG PUBLISHING GLOBALIZE PRIVATE LIMITED

OFFICE : 1, Plo-72, P.M.M.M. Marg, Tardeo, Mumbai-400034. MAHARASHTRA. INDIA
TEL. : 022 23522068. (M) : +91 9969392245.
Website : www.gpglobalize.com | Email : gpglobalize@gmail.com / publish@gpglobalize.com
CIN U22130MH2016PTC287238 | UAN - MH19D0008178